FE-2465-12
Distribution Category UC-90f

EROSION STUDY IN TURBOMACHINERY AFFECTED BY COAL AND ASH PARTICLES

Annual Progress Report for the

Period of

November 1, 1978 to December 31, 1979

W. Tabakoff,
A. Hamed,
J. Ramachandran,
R. Kotwal,
and B. Beacher

University of Cincinnati
Department of Aerospace Engineering and Applied Mechanics
Cincinnati, Ohio 45221

Date Published - February 1980

PREPARED FOR THE UNITED STATES
ENERGY RESEARCH AND DEVELOPMENT ADMINISTRATION

Under Contract No. E(49-18)-2465

RB

Blank Page

TABLE OF CONTENTS

	Page
ABSTRACT	1
OBJECTIVE AND SCOPE OF THE WORK	1
HIGH TEMPERATURE EROSION STUDY	2
EROSION PREDICTION DUE TO FLY ASH	10
ANALYTICAL INVESTIGATION OF THE GAS-PARTICLE FLOW IN EROSION TUNNEL TEST SECTION	19
REFERENCES	22
NOMENCLATURE	24

LIST OF ILLUSTRATIONS

FIGURE	TITLE	PAGE
1	Schematic of Test Apparatus	25
2	Schematic of Air Supply and Control System	26
3	Fly Ash Particle Size Distribution	27
4	Effect of Velocity on 304 Steel at Room Temperature	29
5	Effect of Velocity on Rene 41 at Room Temperature	30
6	Effect of Velocity on A286 at Room Temperature	31
7	Effect of Velocity on 304 Steel at 300°F	34
8	Effect of Velocity on Rene 41 at 300°F	35
9	Effect of Velocity on A286 at 300°F	36
10	Effect of Velocity on 304 Steel at 600°F	39
11	Effect of Velocity on Rene 41 at 600°F	40
12	Effect of Velocity on A286 at 600°F	41
13	Effect of Velocity on 304 Steel at 900°F	44
14	Effect of Velocity on Rene 41 at 900°F	45
15	Effect of Velocity on A286 at 900°F	46
16	Effect of Velocity on 304 Steel at 1200°F	49
17	Effect of Velocity on Rene 41 at 1200°F	50
18	Effect of Velocity on A286 at 1200°F	51
19	Effect of Angle of Attack on 304 Steel at Room Temperature	54
20	Effect of Angle of Attack on 304 Steel at 300°F	55
21	Effect of Angle of Attack on 304 Steel at 600°F	56
22	Effect of Angle of Attack on 304 Steel at 900°F	57
23	Effect of Angle of Attack on 304 Steel at 1200°F	58

FIGURE	TITLE	PAGE
24	Effect of Angle of Attack on Rene 41 at Room Temperature	60
25	Effect of Angle of Attack on Rene 41 at 300°F	61
26	Effect of Angle of Attack on Rene 41 at 600°F	62
27	Effect of Angle of Attack on Rene 41 at 900°F	63
28	Effect of Angle of Attack on Rene 41 at 1200°F.	64
29	Effect of Angle of Attack on A286 at Room Temperature	66
30	Effect of Angle of Attack on A286 at 300°F	67
31	Effect of Angle of Attack on A286 at 600°F	68
32	Effect of Angle of Attack on A286 at 900°F	69
33	Effect of Angle of Attack on A286 at 1200°F	70
34	Effect of Temperature on 304 Steel	72
35	Effect of Temperature on Rne 41	73
36	Effect of Temperature on A286	74
37	Comparative Erosion Damage at Particle Velocities of 600 ft/sec	76
38	Comparative Erosion Damage at Particle Velocities of 800 ft/sec	77
39	Comparative Erosion Damage at Particle Velocities of 1000 ft/sec	78
40	Fly Ash Particle Size Distributions	80
41	Erosion Caused by Various Types of Fly Ash Particles (Experimental Results)	81
42	Ranges in Analysis of Fly Ash (Ref. 14)	82
43	Erosion Vs. Angle of Attack for Different Commercial Abrasives (Experimental Results)	83
44	Erosion Vs. Particle Size at Room Temperature (Experimental Results)	84
45	Erosion Vs. Particle Size at 900°F (Experimental Results)	85

FIGURE	TITLE	PAGE
46	Erosion Vs. Angle of Attack (Experimental and Predicted Results)	87
47	Erosion Vs. Particle Velocity (Experimental and Predicted Results)	88
48	Assumed Particle Size Distributions	90
49	Relative Erosion Loss Caused by Different Types of Fly Ash on 304 St. Steel Specimens (Predicted Results)	91
50	Relative Erosion Loss Caused by Different Types of Fly Ash Particles on INCO-718 Specimens (Predicted Results)	92
51	Relative Erosion Loss Caused by Different Types of Fly Ash Particles on 304 St. Steel Specimens (Predicted Results)	93
52	Relative Erosion Caused by Different Types of Fly Ash Particles on Rene 41 Specimens, (Predicted Results)	94
53	Schematic of Wind Tunnel Test Section Geometry	95
54	Trajectories of Particles which Impact the Specimen Leading and Trailing Edges	96
55	Trajectories of Particles which Impact the Specimen Leading and Trailing Edges	97
56	Trajectories of Particles which Impact the Specimen Leading and Trailing Edges	98
57	Trajectories of Particles which Impact the Specimen Leading and Trailing Edges	99
58	Trajectories of Particles which Impact the Specimen Leading and Trailing Edges	100
59	Trajectories of Particles which Impact the Specimen Leading and Trailing Edges	101
60	Trajectories of Particles which Impact the Specimen Leading and Trailing Edges	102
61	Trajectories of Particles which Impact the Specimen Leading and Trailing Edges	103
62	Percent of Particle that Impacts Vs. Particle Diameter	104

FIGURE	TITLE	PAGE
63a	Plots of Particle Angles and Velocities at Three Upstream Locations	105
63b	Plots of Particle Angles and Velocities at Three Upstream Locations	106
64	Plots of Particle Angles and Velocities	107
65	Trajectories for Different Particle Sizes (α = 40°)	108
66	Trajectories for Different Particle Sizes (α = 10°)	109

LIST OF TABLES

TABLE	TITLE	PAGE
1	Analysis of Fly Ash	17
2	Heat Treatment Cycles for Rene 41 and A286	18
3	Series I - Room Temperature	32
4	Series II - 300°F	37
5	Series III - 600°F	42
6	Series IV - 900°F	47
7	Series VII - 1200°F	52
8	Chemical Analysis of Fly-Ash	79
9	Value of Erosion Constant in Equation (4)	86
10	Assumed Fly Ash Compositions	89

ABSTRACT

In order to provide a basis for alloy selection in future turbines using coal as a fuel, an investigation is undertaken to obtain a basic understanding of the mechanisms of erosion at high temperatures due to particulate fly ash. Three alloys were tested in the test facility which has been designed to simulate the aerodynamic and thermodynamic conditions in the turbine. The effects on erosion due to the high temperature coal ash gas stream was determined at several gas temperatures, particle velocities and angles of attack. The test results for 304 stainless steel, Rene 41 and A286, and the corresponding conclusions are presented. In addition, a series of experiments were conducted to determine the effects of fly ash constitutents, particle size, particle velocity, angle of attack and target temperature on the erosion of iron and nickel bas alloys. Based on the experimental results, a semi-empirical equation has been obtained for the prediction of the erosion losses. This equation provides a new technique for predicting the metal erosion due to the fly ash produced by the conventional burning of coal.

OBJECTIVE AND SCOPE OF THE WORK

The objective of this research is to perform an experimental and theoretical study of the erosion of potential turbine materials caused by coal and ash particles. Attempts will be made to determine the factors which are significant in such erosion, and a computer model will be developed which will facilitate the prediction of potential for erosion in future turbomachinery design.

HIGH TEMPERATURE EROSION STUDY

Introduction

The use of pulverized coal as fuel in many power plants and industrial establishments is inevitable both in the present and in the future. The products of combustion will contain solid particles, whose presence cause erosion of the engine components and in a very short time possible deterioration of the power output. Air filtration cannot accomplish a 100 percent removal of the particles, but also results in performance reduction. In coal gasification both the coal and the catalyst contribute to the resulting particulate flow. While larger particles can be removed by cyclones, a quantity of particles ranging in size between 5 and 25 microns diameter still pass through the cyclones and enter the turbine resulting in a very limited life of this component.

The design and development of high performance turbomachinery operating in an ambient with coal particles or coal ash therefore requires a thorough knowledge of the fundamental erosion phenomena. The future of advanced turbomachinery for use in the coal industry, gasification, mining, pipelines' gas transport, powder coal burning, coal-oil gas refinery, and many others in dependent upon this understanding. If erosion could be incorporated as an engine design parameter, perhaps an erosion tolerant engine could be produced.

Two problems are involved in erosion prediction. First the velocity, direction, and number of particles striking the surface must be determined. These are naturally affected by the general and local flow conditions. The second part involves the calculation of the surface material removed using the information obtained from the first part. The problem of predicting erosion in rotating machinery is particularly complexed by tracing trajectories through the flow field after multiple impacts [1].

Present State of the Art

The theoretical studies concerning erosion are predominantly empirical. They involve basic assumptions as to the process governing material removal. Finnie [2] and Smeltzer, et al. [3] have conducted theoretical analyses of the erosion of ductile materials. In more recent investigations [1], [4] and [5], further insight into the actual mechanism of erosion has been obtained by examining the target surface at high magnification using metallographic techniques and electron microscopy. The work reported in references [2] through [5] has been conducted using the sand-blasting erosion test facility described in reference [5] or modifications of it. This facility utilizes a small jet of particle-laden air impacting on a stationary specimen, and does

not simulate the aerodynamic effect of the flow field over the erosion specimen. This effect can be a very important factor in turbomachine erosion, where the flow is constantly turned by rotating and stationary cascades. Two cold gas particle erosion test facilities have been built at the University of Cincinnati's Propulsion Laboratory. The first was designed to obtain basic erosion data, particle impact, and rebound characteristics for particulate flow over a stationary specimen. Another test facility was then designed to simulate and measure the erosion of stationary and rotating turbomachine blades. A detailed description of these test facilities can be found in references [1] and [6].

In many turbomachinery applications, however, erosion takes place at elevated temperatures near the strength limiting temperatures of the materials used. For example, even in the case of turbojet engine compressors, titanium used in the early stages and the INCO 718 used in the aft stages are operated at metal temperatures in excess of 316°C and 593°C (600°F and 1100°F) respectively. In both cases, these temperatures are very close to the maximum operating temperatures used for these materials. The erosion characteristics can significantly change under elevated temperatures as evidenced in the data presented by Tabakoff and Hamed [7]. This data was obtained in the same facility of reference [1], with the sample heated to temperatures up to 204°C (400°F). Although this temperature falls far short of those experienced in turbine engines, it still indicates the significant effect of temperature on erosion and probably on the rebound characteristics.

High Temperature Erosion Rig

An erosion test facility was designed to provide erosion and rebound data in the range of operating temperatures experienced in compressors and turbines. For that purpose, this facility has been designated to operate at a test section temperature in the range of ambient to 1093°C (2000°F). In addition to high temperatures, the facility properly simulates all erosion parameters which were found to be important from previous testing at ambient temperatures. These parameters include particle velocity, angle of impact, particle size, particle concentration and sample size.

As with the cold flow erosion test facility, close attention was given to aerodynamic effects to insure that important parameters such as angle of attack are not masked or altered. To insure the correlation of data from the high and low temperature erosion tunnels, flowpath and acceleration tunnel length were kept almost identical with those of the facility described in reference [1]. The cross section was increased, however, from 76.2 mm x 25.5 mm to 88.9 mm x 25.4 mm (3" x 1" to 3½" x 1") in order to reduce the tunnel blockage by the test sample [6].

A schematic of the test apparatus [6] is shown in Fig. 1. The main components of the set-up are the following:

A) Main air supply.
B) Combustor.
C) Particle feeder.
D) Particle preheater and injector.
E) Acceleration tunnel.
F) Test section.
G) Settling chamber.
H) Control systems and instrumentation.

A measured quantity of ash is fed into the particle feeder (C), which is driven up into the particle preheater (D) by a constant flow of secondary air. It is injected into the main flow, downstream of the combustor, where it thoroughly mixes with it. The air flow which has been heated by the combustor (B) and the ash particles, are accelerated in the acceleration tunnel (E) and impinge upon the specimen in the test section (F). Further, the particles mix with the water from test section cooling jacket and flow into the settling tank (G).

Control Systems and Instrumentation

Figure 2 shows a schematic of the air supply and control system. The air flow rate was controlled by means of the control valve downstream of the orifice plate. Mass flow rates were calculated based on the orifice pressure and pressure difference. Orifice plates of diameter 1.836 in. and 2.021 in. were used during the course of this experimentation in order to obtain a range of velocities. For efficient operation of the regulator-and-valve, a static pressure of 60 psi was set using the manual pressure loader. The control valve was always kept slightly open before the test facility shut off valve was opened. Otherwise, a rapid buildup of the pressure could damage the regulator-and-valve.

Static and total pressure tappings were provided just downstream of the combustor. Static pressure tappings were also provided upstream and downstream of the specimen at the test section. Combustion temperatures were measured by means of a thermocouple sensor. Also, thermocouple sensors along the walls of the tunnel provided a measure of the liner temperature.

Since there was a loss in temperature between the gases at the exit of the combustor and that at the test section, calibration charts were drawn up by using rakes at the test section to measure the temperatures and pressure. An instrumented sample with thermocouples fixed on it was used to verify the test sample temperatures.

Calculations of air properties at the test section were based on Rayleigh and Fanno line assumptions. Using the conditions of the gas at the entrance to the tunnel and the mass flow rate,

the test section conditions were obtained utilizing a computer program. A friction coefficient of 0.003 in the tunnel was assumed. The calculated air velocities along the length of the tunnel were used to obtain the particles' drag and velocities. The validity of the velocity calculations are verified by utilizing high speed photographic techniques, and Laser Doppler Velocimeter systems (L.D.V).

The ash whose erosive properties were to be studied was obtained from the Cincinnati Gas and Electric Company. Properties of the ash are shown in Table I. A particle size distribution utilizing a Coulter counter was obtained for particles less then 53 microns in diameter. For particles greater than 53 microns, the size distribution was obtained using a sieve analysis. The fly ash distribution is shown in Fig. 3. A weighted averaged rendered a mean diameter of 38.4 microns which was the value used in the computer program to obtain the particles' drag and velocities.

The materials whose erosion resistances were to be studied were chosen as 304 stainless steel, Rene 41 and A286. The choice of these three alloys was based on the following justifications:

A) An experimental study of the erosion characteristics of 304 stainless steel at room temperature had been carried out by other researchers [8], and provided data for room temperature erosion correlation.

B) Rene 41 and A286 were alloys used in the primary turbine stages of successful aircraft jet engines, due to their superior thermal properties in resisting thermal shock. However, if they were to be used in coal fueled gas turbines, it was necessary to study their erosion resistive behavior.

Specimens of these alloys were cut from sheets in the condition 'as received' to sizes of 1.0" x 0.75" and were polished to a uniform surface finish on silicon carbide abrasive discs of 600 grit. They were subsequently cleaned with acetone and weighed to an accuracy of 0.1 mg.

Specimens of Rene 41 and A286 were also heat treated prior to testing, and the heat treatment cycles are shown in Table II.

Results and Discussion

Five series of tests were conducted on the 3 alloys, viz. 304 st. steel, Rene 41 and A286 (Figs. 4-18). Each series consisted of about twenty-four tests carried out at six different angles of attack, fifteen degrees apart at a particular temperature. The temperatures were chosen three hundred degrees apart, between 300°F and a maximum at 1200°F. These constituted four series of tests at high temperatures. A series of tests was conducted at

room temperature to provide data for the correlation of tests conducted in this facility with that of tests conducted in the cold flow test tunnel, as shown in Figs. 4, 5 and 6, Series I. The test data for the same three alloys, but at different gas temperatures, are shown in Figs. 7 through 9 for tests at 300°F, Figs. 10 through 12 for 600°F, Figs. 13 through 15 for 900°F and Figs. 16 through 18 for 1200°F.

The effects on erosion due to the particle velocities, the angles of attack, and the temperatures were obtained. The erosion was expressed in terms of the erosion volume parameter which is defined as the volume of material removed per unit weight of impacting ash particles. This was preferred over the erosion mass parameter as it provides a better estimate of blade damage with respect to change of shape or blade profile. The effect of ash concentration was not studied, the concentration varied between 0.1 to 0.3 g/ft^3 of air.

Effect of Velocity on Erosion

Since erosion is known to vary with velocity raised to some exponent 'n', logarithmic plots of experimental erosion data versus particle velocity yielded straight lines at the different angles of attack. Since $\varepsilon \propto V^n$,

$$\frac{\varepsilon_1}{\varepsilon_2} = \left(\frac{V_1}{V_2}\right)^n$$

$$\text{i.e.,} \quad \log\left(\frac{\varepsilon_1}{\varepsilon_2}\right) = n \log \left(\frac{V_1}{V_2}\right)$$

Thus, slopes of the straight lines obtained from logarithmic plots provided the velocity index 'n'. From these plots the erosion at three specific velocities, viz. 600 ft/sec, 800 ft/sec, and 1000 ft/sec, were obtained, and the values of 'n' computed (Tables III through VII). In certain cases, it was necessary to extrapolate to these values but since the trends were linear in the logarithmic scale, the error is minimal. In all cases, the erosion rate was found to increase with increasing incidence angles and materials, thus providing only positive values for the index 'n', contrary to the findings of Smeltzer et al. [9]. However, it was found that 'n' varied with angle of attack, temperature and material. Values of 'n' as high as 2.78 for Rene 41 at a temperature of 300°F and an angle of attack of 30°, and as low as 0.68 for 304 stainless steel at a temperature of 1200°F and an angle of attack of 90° were observed. Comparison of the index 'n' revealed that the dependence of the erosion rate on incidence velocity is greater at the impingement angle associated

with the next larger erosion rate in 78% of the cases. This can also be casually evidenced by a visual examination of the plots of erosion volume parameter versus particle velocities. In general, the average slope for corresponding high temperatures was higher for A286 compared to Rene 41 and higher for Rene 41 as compared to 304 stainless steel. This implies that changes in velocity would have a greater effect on A286 compared to Rene 41 and Rene 41 over 304 st. steel. No obvious trend has been noticed in the change of 'n' with temperature.

Effect of Angle of Attack

The effect of the angle of attack on the erosion rate showed a persistent trend of ductile behavior in the case of all three alloys, independent of the magnitude of the particle velocity or the temperature (Figs. 19 through 33). Starting from 15° angle of attack, the erosion rate increased until a maximum at about 30° (25° for 304 st. steel) and then decreased to a residual value at normal impact. The definition of the point of maximum erosion becomes much more explicit with increasing velocity and increasing temperature. It has been observed that the general erosion (ε) trend is $\varepsilon_{30°}$ ($\varepsilon_{25°}$ for steel) > $\varepsilon_{45°}$ > $\varepsilon_{60°}$ > $\varepsilon_{75°}$ > $\varepsilon_{90°}$ for the three alloys at corresponding temperatures and particle velocities. Two exceptions to this rule were observed with A286 at room temperature and at 600°F. At room temperature, the erosion rate at 15° angle of attack was higher than at 45° for corresponding velocities by about 20% (Fig. 29), and at 600°F by about 12% (Fig. 31).

Effect of Temperature

In order to study the effects of temperature on erosion, plots of temperature versus the erosion rate at the maximum angle of erosion were obtained (Figs. 34, 35 and 36). These were at 30° for A286 and Rene 41 and 25° for 304 st. steel. The base scale also provides a comparison of the target temperature to the melting temperature, i.e. the homologous temperature ratio [°R/°R]. However, the three alloys had melting temperatures in the same range and therefore did not provide any information toward a trend with the melting temperature. All three alloys exhibited an increasing trend of erosion with increased temperature. Rene 41 and A286 showed rather similar trends at higher temperatures but differed significantly with those of 304 st. steel. The rate of increase of erosion with temperature decreases between 900°F and 1200°F for both Rene 41 and A286 as compared with that between 600°F and 900°F (Figs. 35 and 36). This is quite in contrast to the characteristics of 304 st. steel which shows higher slopes between 900°F and 1200°F as compared with that between 600°F and 900°F (Fig. 34). This was observed in the case of all three velocities considered. By examining the three alloys independently, the following remaks may be made:

(a) 304 St. Steel: This metal exhibits a linear trend of increasing erosion up to 900°F at particle velocities of 600 ft/sec and 800 ft/sec (Fig. 34). At temperatures beyond this, a much sharper trend is observed. This is also observed to be the case at the higher particle velocity of 1000 ft/sec.

(b) Rene 41: At a particle velocity of 600 ft/sec, Rene 41 shows a linear trend of increasing erosion up to 600°F (Fig. 35). Between 600°F and 900°F a sharper trend is observed but falls off between 900°F and 1200°F resulting in a very marginal increase between these temperatures. This is also observed to be the case at a particle velocity of 800 ft/sec. At a higher particle velocity of 1000 ft/sec, the increase in erosion is quite significant between 900°F and 1200°F, but a decreasing trend in the slope is observed.

(c) A286: Except for a near constant erosion at a particle velocity of 600 ft/sec between room temperature and 600°F, the trends of this alloy are similar to those of Rene 41, which has already been discussed (Fig. 36).

Comparative trends of the three alloys at the three particle velocities considered can be seen in Figs. 37 through 39. It can be observed from Figs. 38 and 39 that for particle velocity ranges in the region of 800 ft/sec to 1000 ft/sec, 304 st. steel has a higher erosive resistance compared to Rene 41 and A286 up to a temperature of about 1050°F. At this temperature (1050°F), the resistance of all three alloys is about the same, the erosive damage being in the region of 1.8×10^{-4} cm^3/gm at a velocity of 800 ft/sec and in the region of 3.1×10^{-4} cm^3/gm at a velocity of 1000 ft/sec. But beyond this temperature the erosion damage of 304 st. steel increases very sharply. This increase is very explicit at higher particle velocities (Fig. 39).

Effect of Heat Treatment

Heat treated specimens of Rene 41 tested showed an approximate 23% decrease in erosion for corresponding velocities at the angle of maximum erosion, at temperatures of 600°F, 900°F and 1200°F. At other angles of attack also, the heat treated specimens showed a higher erosion resistance but since the points fell within the normal scatter region, no definite conclusions could be made. No sudden change from ductile to brittle behavior was observed due to hardening.

Specimens of heat treated A286 were tested only at 1200°F. Here, too, the points fell within the normal scatter region. Also, the erosion at an angle of attack of 30° was higher than that at 60° suggesting that no change in ductile to brittle behavior occurred due to hardening.

Other Experimental Observations

All test specimens were polished to the same surface finish, a few specimens tested in the 'as received' condition at the higher temperatures feel within the normal scatter region. This suggests that the surface finish is not critical for erosion resistance at high temperatures.

Conclusions from the High Temperature Erosion Study

(1) The velocity exponent 'n' was not found to be constant, but varied widely with angle of attack, gas temperature and target material.

(2) The dependence of the erosion rate on particle incidence velocities was greater at the impingement angles associated with larger erosion rates.

(3) At low angles of attack, the mechanism of erosion was primarily due to chipping action of the impinging particles. As the angle of attack was increased, the brittle mode of erosion was observed to become more predominant.

(4) The general trend in the erosion rate with respect to impingement angle was:

$$\varepsilon_{30^\circ} \ (\varepsilon_{25^\circ} \text{ for 304 Steel}) > \varepsilon_{45^\circ} > \varepsilon_{60} > \varepsilon_{75^\circ} > \varepsilon_{90^\circ}.$$

(5) All three alloys exhibited an increasing trend of erosion with increasing temperatures. However, individual characteristics for particular particle velocities varied.

(6) The effect of heat treatment was significant at the angle corresponding to maximum erosion for Rene 41 and A286.

(7) No change from ductile to brittle behavior was observed in the heat treated specimens of Rene 41 and A286, due to hardening.

(8) Surface finish was not observed to contribute toward the erosion resistance at higher temperatures.

EROSION PREDICTION DUE TO FLY ASH

Introduction

The major problem confronting earlier developers of coal-burning turbines is the serious erosion of turbine blades and other components caused by the fly ash contained in the combustion gases. It is possible to remove approximately 85 percent by weight of the ash in these gases using cyclones. However, small particles ranging in size between 1 and 20 microns still pass through the cyclones and enter the turbine. The severity of this problem can be judged from the fact that a gas turbine operating on pulverized coal combustion is considered to have a short life. Typical ash concentrations for such a turbine are about 7.8 mgm/ft^3 [10]. The damage is caused principally be erosion of the blade trailing and leading edges. Several changes in the blade design to reduce the erosion problem have been made. These include changing the blade configurations to direct the ash towards the turbine casing instead to the rotor hub, and providing large annular space between the first stage stator and rotor blades through which the ash can centrifuge to the casing. Some designs have introduced wear strips at the base of the rotor and stator blades to minimize the erosion at these points. The authors of reference [10] estimated that the maximum life of the stator blades would be 5000 hours and that of the rotor blades 10,000 hours. This is far below the minimum life expectancy of a commercial power plant. A thorough knowledge of the various parameters which influence the extent of erosion damage is required to improve the life and the aerodynamic performance of turbomachinery operating in an ambient with fly ash particles. The future of advanced turbomachinery for use in the coal industry, gasification, mining, pipelines' gas transport, powder coal burning, coal-oil gas refinery and many others is dependent upon this understanding.

Previous mathematical models [11, 12, 13] used to predict erosion rates consider only the influence of parameters such as particle velocity and angle of attack. The effects of composition and particle size should also be considered in order to predict the erosion rates of heterogeneous abrasives such as fly ash. This paper takes into consideration these additonal parameters in the development of a semi-empirical equation which can be used to predict metal erosion due to fly ash produced during the conventional burning of coal.

Preliminary studies were carried out with the following purposes: first, to find out the variation in the amount of erosion caused by fly ash particles acquired from different sources, and second, to understand the nature of the constituents in the fly ash.

Experimental Erosion Study of 304 Stainless Steel

Experiments were conducted on erosion test rigs developed by Grant et al. [1] and Tabakoff et al. [6]. Four types of fly ash acquired from different sources with different compositions and particle sizes were used. The four types of fly ash were: (a) Cincinnati Gas and Electric Company (C.G.&E.), (b) Kingston I, (c) Kingston II, and (d) Exxon. Kingston II fly ash was obtained by the removal of large coarse particles, by using sieves, from Kingston I ash. A series of erosion tests were carried out using these fly ashes. The chemical analyses of three types of fly ash are given in Table 8, and the particle size distributions are shown in Fig. 40. The mean particle sizes of C.G.&E., Kingston I, Kingston II and Exxon fly ash were 38.4μ, 28μ, 15μ and 3.9μ respectively.

Figure 41 shows the measured erosion on 304 stainless steel subject to various angles of attack by the fly ash particles. The tests were carried out at room temperature and for a particle velocity of 450 fps. It can be seen in this figure that the erosion loss reduces significantly when the coarse particles from the Kingston I fly ash were removed. The erosiveness of C.G.&E. fly ash is observed to be greater than that of Kingston I fly ash. The results presented in this figure also show that Exxon fly ash is least erosive among the four samples of fly ash tested.

Kingston and C.G.&E. fly ash were produced during the conventional combustion of coal. Table 8 shows the chemical analysis of the three types of fly ashes. From this table, it can be seen that the compounds of aluminum, silicon and iron are the major constituents of these samples of fly ash. The composition of Exxon fly ash is quite different and contains $CaSO_4$ as one of the major constituents. This is because Exxon fly ash was generated during the fluidized-bed combustion of coal using dolomite as the sorbent for capturing sulfur-dioxide.

Fly Ash Composition

The constituents of fly ash from a given furnace are related to many factors, such as coal composition and size, initial state of raw coal, fuel burning rate, combustion efficiency and methods of fly ash collection. The principal ash-forming minerals in coal are as follows: aluminosilicates (Kaolinite $Al_4Si_4O_{10}(OH)_8$, illite $KAL_2(AlSi_3O_{10})(OH)_2$, and mixed layer clay minerals); sulfides (primarily pyrite FeS_2); carbonates (calcite $CaCO_3$), siderite $FeCO_3$ and ankerite $CaCO_3 \cdot FeCO_3 \cdot MgCO_3$); and quartz ($SiO_2$)

The character of the fly ash is related to the thermal changes which the mineral matter undergoes during the combustion

of coal. Ash composition is generally reported in terms of percent weight of metal oxides in their highest oxidation state. Chemical analyses of a large number of U.S. fly ash [14] produced during the conventional combustion of coal show ranges in composition given in Fig. 42. This representative data shows that there is a large variation in the amounts of various substances that are present in fly ash. For example, the percent by weight of aluminum compound in a fly ash may be as low as 10 and as high as 60. The fly ash contains compounds of silicon, aluminum and iron and smaller amounts of compounds containing titanium, calcium, magnesium, sodium, potassium and sulfur. These compounds occur in fly ash primarily as silicates, oxides and sulfates, along with lesser amounts of phosphates and carbonates.

Erosion Prediction Equation

It is evident that the prediction of erosion caused by fly ash particles is complicated because of the varying properties of fly ash. It is desirable to determine which constituents in fly ash affect metal erosion. The usual method of doing this is to control all other constituents and change only the constituent being considered. This approach cannot be taken in the case of fly ash because its constituents are inseparable. Hence, it was decided to develop a semi-empirical equation which relates the erosive characteristics of a fly ash to that of the commercial abrasives. The effects of chemical composition and particle size distribution in the fly ash will be included in this equation. It will be shown that the equation is general in nature and can be extended to erosion wear situations involving different materials, particle velocities, impingement angles and target temperatures. The amount of material removed by a unit mass of fly ash particles ε, can be expressed as follows:

$$\varepsilon = \psi \sum_{i=1}^{m} \sum_{j=1}^{n} W_i \{\varepsilon_{ij}\ \omega_j\} \qquad (1)$$

where ψ = erosion constant, the value of this constant depends on the properties of the fractional components of the fly ash and the properties of the abrasives available commercially.

W_i = percent by weight of commercial abrasive particles corresponding to i^{th} substance in the fly ash, e.g., the commercial abrasives silica (SiO_2), alumina (Al_2O_3) and iron oxide (Fe_2O_3) correspond to silicon, aluminum and iron compounds respectively in the fly ash.

ε_{ij} = erosion due to unit mass of commercial abrasive particles having diameter D_j and corresponding to i^{th} substance in the fly ash.

ω_j = percent by weight of commercial abrasive particles having diameter D_j, and corresponding to particle size distribution in the fly ash.

m = total number of different substances in the fly ash.

n = a number which can be selected depending on the erosion versus particle size relationship (for higher values of n, the accuracy of the present analysis improves).

Equation (1) can be simplified by the following considerations. From the results presented in Fig. 42, the percent by weights of all the substances (constituents) in the fly ash except those of aluminum, silicon and iron compounds are negligible, i.e.,

$$W_i << W_1, W_2, W_3 \quad \text{for} \quad i > 3 \quad . \tag{2}$$

The above equation (2) suggests a value of 3 for the variable m in equation (1). Therefore equation (1) can be written in the following form:

$$\varepsilon = \psi\Big[\underbrace{\sum_{j=1}^{n} W_1\, \varepsilon_{1j}\omega_j}_{\text{erosion due to alumina}} + \underbrace{\sum_{j=1}^{n} W_2\, \varepsilon_{2j}\omega_j}_{\text{erosion due to silica}} + \underbrace{\sum_{j=1}^{n} W_3\, \varepsilon_{3j}\omega_j}_{\text{erosion due to iron oxide}}\Big] \tag{3}$$

(erosion due to fly ash)

The above equation can be further simplified by examining the experimental results presented in Fig. 43. This figure shows the results of the tests in which 304 stainless steel alloy was eroded by 35 microns alumina, silica and iron oxide particles. The tests were conducted at room temperature with particle velocities of 450 ft/sec. It can be seen that the magnitude of erosion due to alumina and silica particles are comparable but the mangitudes of erosion due to alumina and iron oxide differ markedly. For example, at an impingement angle of 30 degrees (keeping in mind that the average particle size is the same), the erosiveness of the silica and iron oxide are respectively about 65% and 1% based on 100% for alumina. Tests at elevated temperature (900°F) also revealed similar results. Therefore it can be assumed that the erosion due to iron oxide may be neglected and equation (3) can be rewritten as follows:

$$\varepsilon = \psi\Big[\sum_{j=1}^{n} W_1\, \varepsilon_{1j}\omega_j + \sum_{j=1}^{n} W_2\, \varepsilon_{2j}\omega_j\Big] \tag{4}$$

The values of W_1 and W_2 can be obtained from the chemical analysis of the fly ash. The particle size analysis of the fly ash provides the values for ω_j. For a given target material, the values of ε_{1j} and ε_{2j} can be obtained from erosion versus particle size characteristics of alumina and silica particles respectively (as weill be shown later). The appropriate value of ψ is not easily estimated, because the shape, hardness and strength of the particles in the fly ash are so different from those in conventional form. In view of the present uncertain nature of the particles in fly ash, it is preferable to establish this quantity by erosion experiments involving the abrasives and target material of interest. The effects of angle of attack, particle velocity and target temperature can be included by substituting the appropriate values for the variables ε_{1j} and ε_{2j} on the right hand side of equation (4).

Application of Erosion Prediction Equation

In the following discussion, equation (4) will be used to predict the erosion caused by different types of fly ash particles on three target materials, namely 304 stainless steel, Rene 41 and INCO 718. These alloys are widely used in turbomachinery applications. Data on fly ash erosion for such materials is not available in the literature. Therefore before using this equation, it is necessary to obtain data on the amount of erosion caused by alumina and silica particles of various sizes and the value of the erosion constant ψ.

Figure 44 shows the test data for the variation in erosion wear of 304 stainless steel as a function of particle size. The tests were carried out at room temperature. The results are presented for two angles of attack (30 and 60 deg) and two particle velocities (280 and 450 ft/sec). Figure 45 shows the erosion versus particle size plots for three target materials; namely, 304 stainless steel, Rene 41 and INCO 718. The test results are shown for a target temperature of 900°F and a particle velocity of 1000 ft/sec. Only one impingement angle was employed (30°) which was close to the angle of maximum erosion for all three target materials.

For a given target temperature, one erosion test was conducted for each target material using CG&E fly ash particles. The results of these tests and the results presented in Figs. 44 and 45 were used in equation (4) to evaluate the value of the erosion constant ψ. Table 9 lists the values of the erosion constant ψ for the three target materials. The value of ψ was found to be between 0.425 and 0.65. The variation in the value of this constant tends to confirm the complexity of the material property parameters and abrasive property parameters which are controlling the erosion.

Using the appropriate values for ψ and other quantities in equation (4), the erosion mass parameter values for other fly ash particles were obtained. Figure 46 shows the experimental and predicted erosion mass parameter values for 304 stainless steel and three different fly ash particle types. The predicted and experimental erosion values of 304 stainless steel, Rene 41 and INCO 718 by using CG&E fly ash for specimen temperature of 900°F and angle of attack of 30 deg, are shown in Fig. 47. There is good agreement between the predicted and experimental erosion results, thus verifying the usefulness of equation (4) to predict the erosion resistance of a material under attack by fly ash particles. Additional experimental data using fly ash may be found in reference [8].

To facilitate the use of equation (4), a simple computer program was developed. This program was used to study the effects of fly ash composition and particle size distribution on the erosion of a material. For a given target material of interest, the appropriate value of the erosion constant ψ and the erosion values for different sizes of alumina and silica particles (such as shown in Figs. 44 and 45), were provided as input to this program.

The procedure outlined above was used to estimate the erosion on the three target materials (304 stainless steel, Rene 41 and INCO 718) caused by various types of fly ash having assumed compositions and particle size distributions. Table 10 shows 12 different fly ash compositions which were investigated in this study. These compositions were chosen on the basis of ranges in fly ash composition that occurs in practice. Figure 48 shows the 15 different particle size distribution numbers, N, considered (from N=1 to N=15) plotted versus the particle diameters (1 to 200 microns). The fly ash compositions are identified by capital letters (A, B, C, ... L) as shown in Table 10. A particular fly ash is therefore identified by a combination of a letter and a number. Among the fly ash compositions studied, composition A (with 30% Al compound and 60% Si compound) and composition L (with 30% Al compound and 40% Si compound) gave maximum and minimum erosion values respectively and composition G (with 30% Al compound and 50% Si compound) gave an intermediate erosion value, for a given particle size distribution. Therefore, computed erosion results will be presented for these three fly ash compositions only.

Figure 49 shows the estimated relative erosion caused by different types of fly ash particles on 304 stainless steel specimens at room temperature. The results are presented for two angles of attack (30 and 60 deg) and two particle velocities (280 and 450 ft/sec). The spread in the erosion data shown by the three symbols for a given particle size distribution indicates the effect of fly ash composition. The effect of fly ash content is significant when the larger particles (> 30μ) are present in the fly ash. For a given fly ash composition,

particle size distribution N=5 (with particles 1-10μ) and particle size distribution N=6 (with particles 80-200μ) were found to be the least and most erosive respectively.

The predicted dependence of the erosion mass parameter on the fly ash compositions and particle size distributions are shown in Figs. 50, 51 and 52. The results are presented for the three target materials (304 stainless steel, Rene 41 and INCO 718). These results were obtained from the computer program for a target temperature of 900°F, a particle velocity of 1000 ft/sec and an angle of attack of 30 deg. At these conditions the computed results show that 304 stainless steel has a higher erosion resistance compared to Rene 41 and INCO 718. It is seen that the earlier observations (Fig. 49) regarding the effects of composition and particle distribution in the fly ash on the room temperature erosion are true for the elevated temperature erosion also. The computed results also show that the effect of fly ash composition on erosion is more significant in the case of high velocitie particles impinging a target material at elevated temperatures.

Summary and Conclusions

The most important findings of the present study were concerned with the amount and the nature of the erosion caused by different types of fly ash on three different materials (304 stainless steel, Rene 41 and INCO 718). A model to predict erosion (in the form of a semi-empirical equation), was developed which takes into account the effects of composition, particle size and complicated structure of the fly ash particles. It was shown that the technique is general in nature and can be extended to erosion wear situations involving different materials, particle velocities, impingement angles and target temperatures. This equation relates the erosive characteristics of a fly ash to that of the commercial abrasives. The equation was simplified by assuming that, for the fly ash, the percent by weight of all the substances (constituents) excluding that of aluminum, silicon and iron compounds are negligible. This assumption is true only for fly ash produced during the conventional combustion of coal. There was good agreement between the predicted erosion values and the test results, as shown in Figs. 46 and 47.

The study of a variety of fly ashes shows that their erosiveness is directly proportional to the percentage of the aluminum and the silicon compounds. The effect of fly ash content on erosion is significant when larger particles (> 30μ) are present. The computed results also show that the effect of fly ash composition on erosion is more significant in the case of high velocity particles impinging a target material at elevated temperatures. The predicted and test results show that the erosion mass parameter increases at a rapid rate with increasing particles diameter up to about 40 microns and at a slower rate with further increase in particles diameter.

TABLE I

ANALYSIS OF FLY ASH

CHEMICAL ANALYSIS

Chemical	Percentage
Silicon Dioxide (SiO_2)	48.08
Iron Oxide (Fe_2O_3)	20.05
Aluminum Oxide (Al_2O_3)	21.16
Magnesium Oxide (MgO)	0.93
Sulphur Trioxide (SO_3)	1.20
Moisture Content	0.13
Loss on Ignition	0.73
Available Alkalies as Na_2O	0.64
Undetermined	7.08

PHYSICAL ANALYSIS

Surface Area		6615.78 $\frac{cm^2}{cm^3}$
Increase of Drying Shrinkage (28 Days)	0.01	
Water Requirement, % of control	87.00	
Autoclave Expansion	0.01	
Specific Gravity		2.58

TABLE II

HEAT TREATMENT CYCLES FOR RENE 41 AND A286

RENE 41:

The heat treatment simulated that used in the manufacturing process of the first three stages of the turbine nozzle vanes of the G.E. J79.

Description	Temperature	Time	Cooling
Braze Simulation	2150°F ± 25°F	10 min	Helium quench
Stress Relieve Simulation	1975°F ± 25°F	30 min	Air cooled
Ageing	1650°F ± 25°F	60 min	Air cooled

A286:

Description	Temperature	Time	Cooling
Solutioning	1800°F	60 min	Air cooled
Ageing	1325°F	16 hr	Air cooled

ANALYTICAL INVESTIGATION OF THE GAS-PARTICLE FLOW IN EROSION TUNNEL TEST SECTION

The unique erosion tester in the University of Cincinnati Department of Aerospace Engineering and Applied Mechanics laboratory is designed to impact a high velocity, particle-laden gas stream upon a two-dimensional test specimen. The impact velocity and impingement angle of the particles with respect to the specimen must be accurately known since the erosion data is correlated in terms of those parameters. When relatively small particles of the order of 10 microns in diameter are used, their trajectories can be influenced by gas stream deflections in the tunnel test section. Since it is difficult to experimentally observe particles of this size, analytical tools are used to determine the extent of trajectory deviations from the assumed "straight-line" paths.

The analysis is focused upon the erosion tunnel test section, from nearly 6 inches upstream of the test specimen to nearly 4 inches downstream. The objectives are two-fold: (1) to describe the gas flow field by solving the equations of motion for a compressible, inviscid fluid in two dimensions, and (2) to describe the particle trajectories approaching the test specimen in this flow field up to the point of impact with the specimen surface. Both analyses are performed by existing computer programs which assume that all motion is two-dimensional, and define the flow field between tunnel walls and around the specimen on a rectangular grid. The fineness of the numerical grid, especially around the test section, gives good definition to the flow field where gas deflection is significant. Although the gas flow field is determined over the entire grid, the particle trajectories are considered only from a short distance ahead of the specimen (where the flow begins to turn) to the specimen itself. A schematic of the wind tunnel cross section is shown in Fig. 53.

The analyses model certain test conditions from which experimental results are available. Specimens of one inch in length are studied at angles of 10 and 40 degrees to the incoming flow. An inlet gas Mach number of 0.4 is used with total properties of 16.2 psia and 522°R. Particle sizes of 2, 5, 10 and 28 microns are considered, assuming an average particle density (representative of coal ash) of 206 lb_m/ft^3.

Analytical Results

It has been hypothesized that the geometry of the erosion tunnel test section and specimen produces a significant flow perturbation that influences the incoming trajectories of the small (less than 10 micron diameter) coal ash particles. The degree to which the particles deviate from their "straight-line" paths is presented herein as a function of particle size for two

representative specimen positions. Variations in particle velocity and angle are shown at several locations (see Fig. 53) upstream of the specimen. Verification of these calculations await the measurements to be obtained with the Laser Doppler Velocimeter.

Figures 54 through 61 illustrate the two-dimensional, inviscid flow streamlines around a 2.54 cm (1 inch) specimen inclined at α = 10 degrees and at 40 degrees from the vertical centerline of the accelerating tunnel. Superimposed on these flow fields are the trajectories of the two particles which impact the specimen edge extremes. Of great significance is the ratio of the upstream cross-sectional area that contains the impacting particles, A_a, to the projected area of the specimen, A_p, as shown in Fig. 54. This ratio is a measure of the percentage of particles in the upstream "shadow" of the specimen that eventually impact the specimen. The ratio approaches 1.0 for the large particles as shown in Fig. 57, which are relatively unaffected by the distorted aerodynamics near the specimen. However, the smaller particles as shown in Figs. 54, 55 and 56, whose trajectories are strongly invluenced by the flow field, exhibit ratios much less than unity. A ratio of zero for the 2 and 5 micron diameter particles approaching the 10 degree specimen, as shown in Figs. 58 and 59, indicates that no impacts on the specimen are predicted. Figure 62 shows how this ratio varies not only with particle diameter but also with specimen angle of attack, α. When the specimen is more nearly aligned with the incoming flow, more of the smaller particles tend to "slip by" without colliding.

As the smaller particles approach the specimen, both the magnitude and direction of their velocities experience significant changes. Figures 63a, 63b and 64 show the angle measured between the particle path and the vertical axis at three locations upstream of the specimen for the cross sections A-A, B-B and C-C as shown in Fig. 53. As expected, the smaller (2 and 5 micron diameter) particles deviate more than the longer (10 and 28 micron diameter) particles from the desired zero-degree direction at all three locations. The particles nearer to the specimen leading edge of the specimen at 40°, ash shown in Fig. 63, show the largest deviations, up to 25 degrees for the smallest particles at the closest location (C-C) to the specimen. The particles nearer to the specimen trailing edge show the smallest deviations, only 5 degrees in the most extreme case. For the specimen at 10 degrees, as shown in Fig. 64, a different trend is observed. The particle angle deviations are nearly constant for all particles of a given size at a given location, and their direction is opposite to that of the 40 degree specimen. It can be seen that the specimen orientation is of primary influence upon the small particle trajectories.

Figures 63a, 63b and 64 also show the variation in particle velocity for both small and large particles at the same three upstream locations (A-A, B-B and C-C). Only slight variations in velocity magnitude are observed among the impacting particles

at any given location, as was seen in the angle profiles. However, the level of the velocity changes significantly for the smaller particles from location (A-A) to location (C-C); specifically they are observed to decelerate as they move closer to the specimen at 40 degrees and to accelerate as they move closer to the specimen at 10 degrees. These characteristics are dependent not only upon specimen orientation and particle size, but also upon the initial velocity difference, or relative velocity, between the particles and the gas stream. At locations closer than 0.5 inches upstream of the specimen center, the accuracy of the trajectory calculations are questionable due to the exaggerated flow gradients of the compressible but inviscid flow field. However, the trajectories can be reasonably extrapolated to the specimen surface in an attempt to estimate the particle velocity and angle at impact. This was done for some of the 2 micron particles that impact the specimen inclined at 40 degrees, and is shown in Fig. 65, along with a few representative trajectories of other particle sizes. Similar trajectories for different size particles are shown in Fig. 66.

When the accuracy of these analytical investigations have been established from test measurements, further studies could be performed to systematically investigate the effects of varying inlet velocity, specimen size, angle of attack, and particle diameter. Such data will be very useful for predicting erosion. Additional information in regard to this research may be found in references [15] and [16].

REFERENCES

1. Grant, G. and Tabakoff, W., "Erosion Prediction in Turbomachinery Resulting from Environmental Solid Particles," Journal of Aircraft, Vol. 12, No. 5, May 1975, pp. 471-478.

2. Finnie, I., Wolak, J. and Kabil, Y., "Erosion of Metals by Solid Particles," Journal of Materials, Vol. 2, No. 3, September 1967, pp. 682-700.

3. Smeltzer, C.E. et al., "Mechanisms of Sand and Dust Erosion in Gas Turbine Engines," USAAVLABS Technical Report, August 1970.

4. Fraas, A.P., "Survey of Turbine Bucket Erosion, Deposits, and Corrosion," ASME Paper No. 75-GT-123, presented at the Gas Turbine conference, Houston, Texas, March 2-6, 1975.

5. Finnie, I., "An Experimental Study on Erosion," Proceedings of the Society for Experimental Stress Analysis, Vol. 17, No. 2, pp. 65-70.

6. Tabakoff, W. and Wakeman, T., "Test Facility for Material Erosion at High Temperatures," ASTM Publication, Erosion: Prevention and Useful Applications STP 664, 1979.

7. Tabakoff, W. and Hamed, A., "Aerodynamic Effects on Erosion in Turbomachinery," JSME and ASME Paper No. 70, 1977 Joint Gas Turbine Congress, Tokyo, Japan, May 22-27, 1977.

8. Tabakoff, W., Kotwal, R. and Hamed, A., "Erosion Study of Different Materials Affected by Coal Ash Particles," Wear, 52, (1979), pp. 161-173.

9. Smeltzer, C.E., Gulden, M.E., McElmury, S.S. and Compton, W.A., "Mechanisms of Sand and Dust Erosion in Gas Turbine Engines," USAAVLABS Technical Report 70-36, U.S. Army Air Mobility Research and Development Lab., Ft. Eustis, Va., August 1970.

10. Nabors, W.M., Strimbeck, D.C., Cargill, R.W. and Smith, J., "Bureau of Mines Progress in Developing the Coal Burning Gas Turbine Power Plant," Journal of Engineering for Power, April 1965, pp. 215-222.

11. Finnie, I., "The Mechanism of Erosion of Ductile Metals," Proceedings of 3rd National Congress of Applied Mechanics, ASME Trans., 1958, pp. 527-532.

12. Bitter, J.G.A., "A Study of Erosion Phenomena, Part I and Part II," Wear, 6 (1963), pp. 5-21 and pp. 169-190.

13. Neilson, J.H. and Gilchrist, A., "Erosion by a Stream of Solid Particles," Wear, 2 (1968), pp. 111-122.

14. White, H.J., "Effect of Fly Ash Characteristics on Collector Performance," JAPCA, Vol. 15, May 1955, pp. 37-50, 62.

15. Tabakoff, W., "Erosion Study in Turbomachinery Affected by Coal and Ash Particles. Phase 1," U.S. Department of Energy Annual Progress Report, FE-2465-5, January 1978.

16. Tabakoff, W. and Hamed, A., "Erosion Study in Turbomachinery Affected by Coal and Ash Particles," U.S. Department of Energy Annual Progress Report, FE-2465-9, November 1978.

NOMENCLATURE

D	particle diameter.
m	total number of different substances in the fly ash.
n	a number to account for the particle size effect in the erosion prediction equation.
V	particle velocity.
W_i	percent by weight of commercial abrasive particles corresponding to i^{th} substance in the fly ash.
ω_g	percent by weight of commercial abrasive particles having diameter D_j.
ε	erosion mass parameter, expressed as milligrams of material eroded per gram of abrasive impacted on the specimen surface.
ψ	erosion constant.
μ	microns.
α	impingement angle.

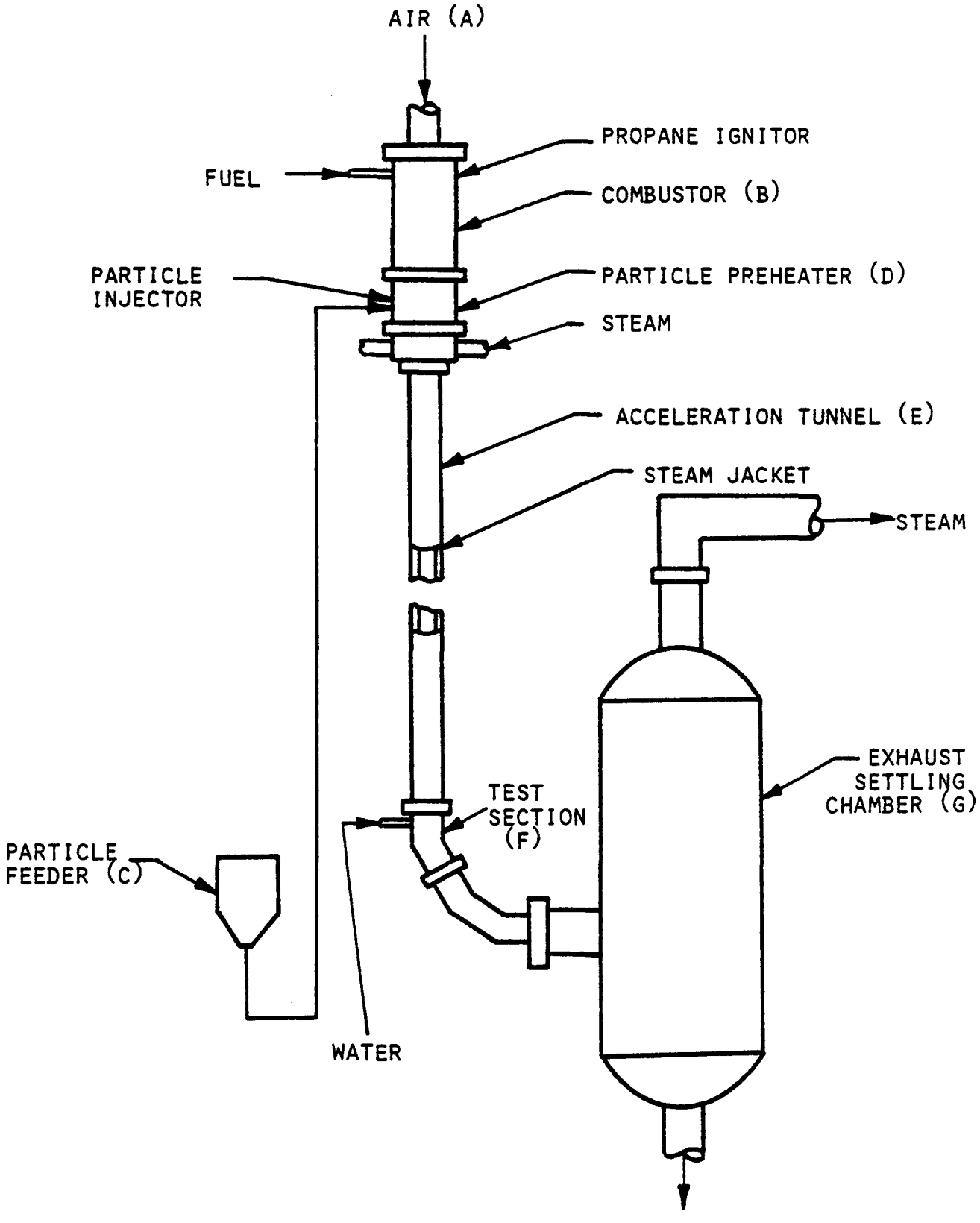

FIG. 1. SCHEMATIC OF TEST APPARATUS.

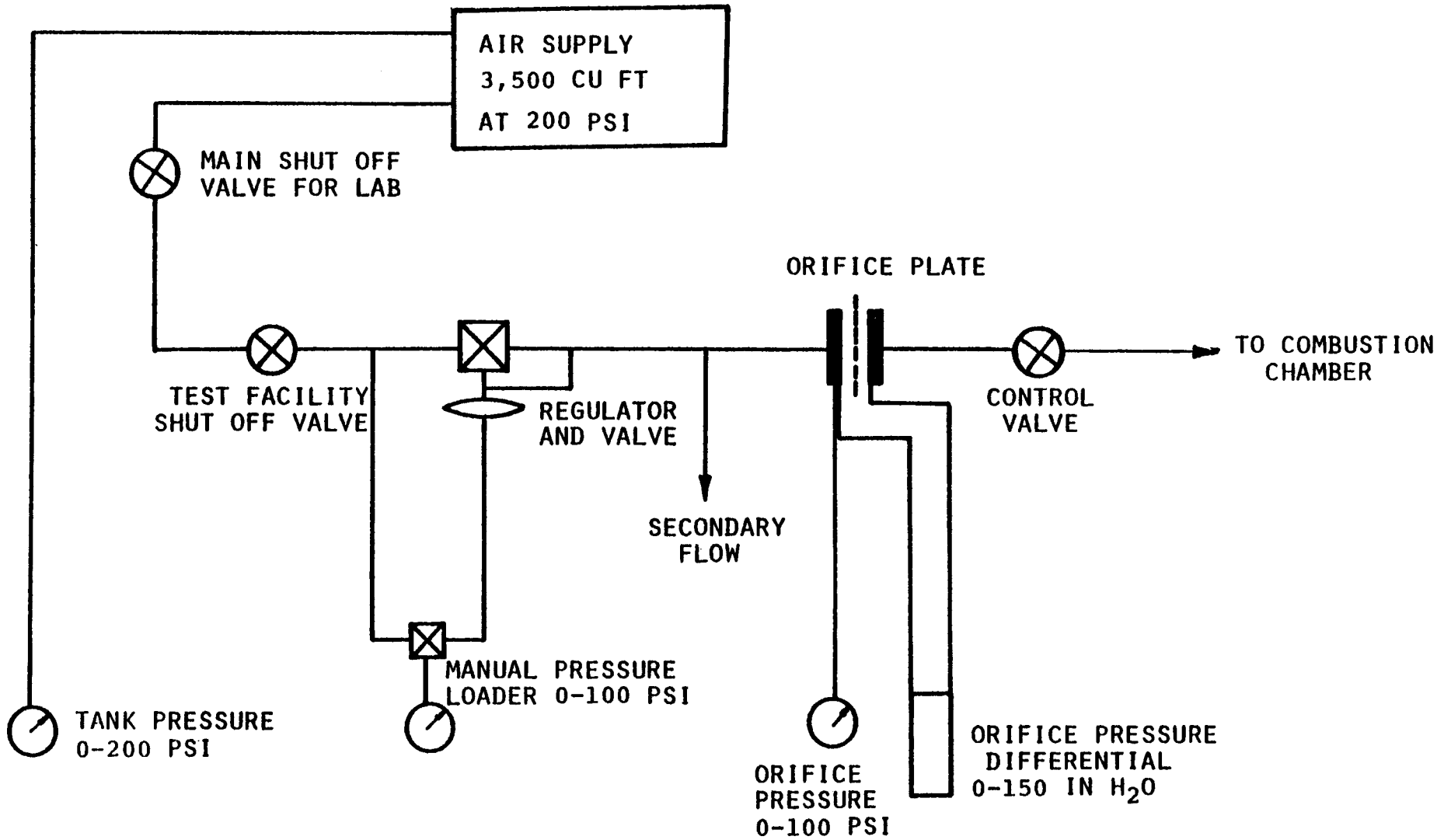

FIG. 2. SCHEMATIC OF AIR SUPPLY AND CONTROL SYSTEM.

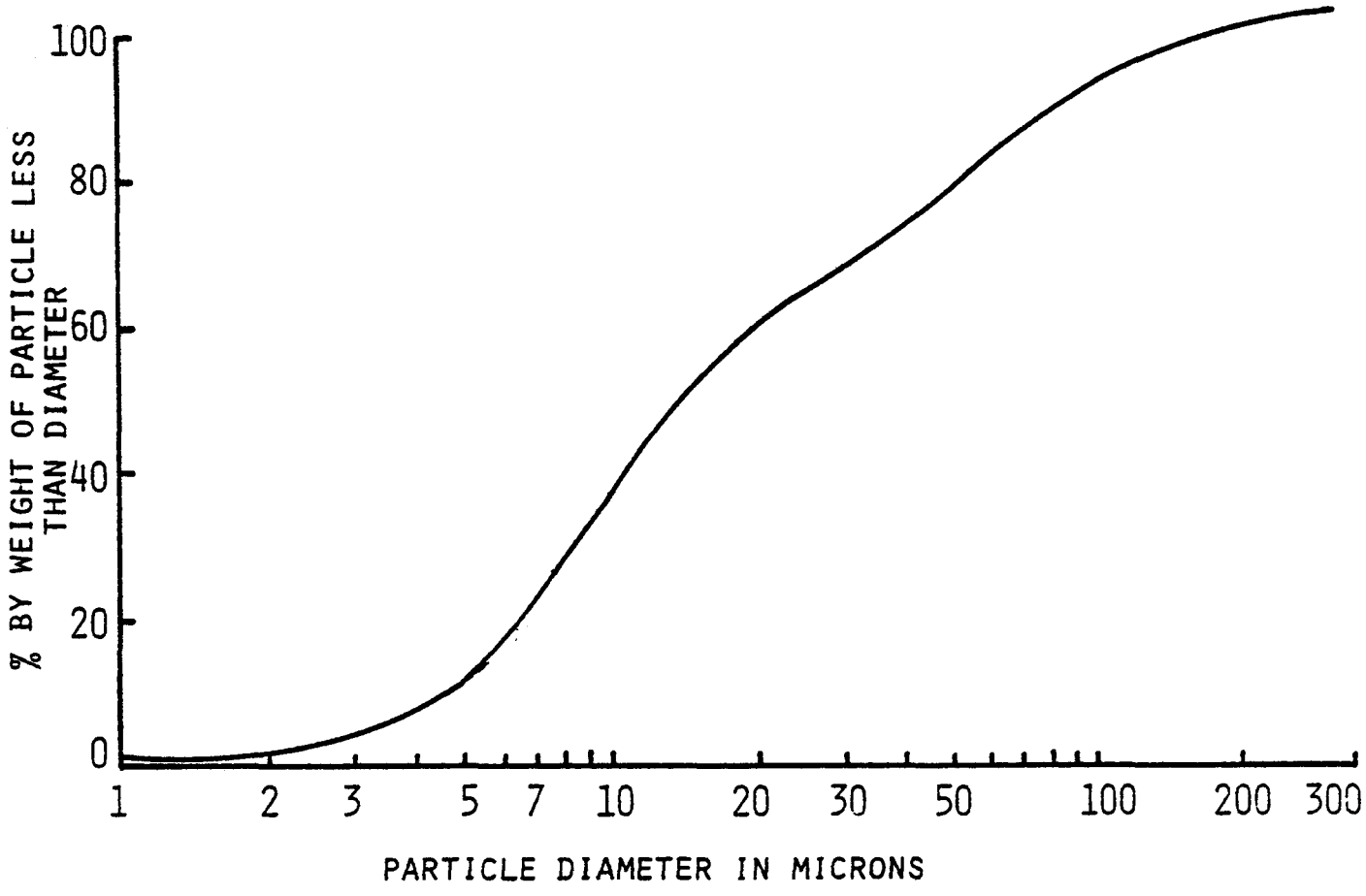

FIG. 3. FLY ASH PARTICLE SIZE DISTRIBUTION.

SERIES I - TESTS AT ROOM TEMPERATURE

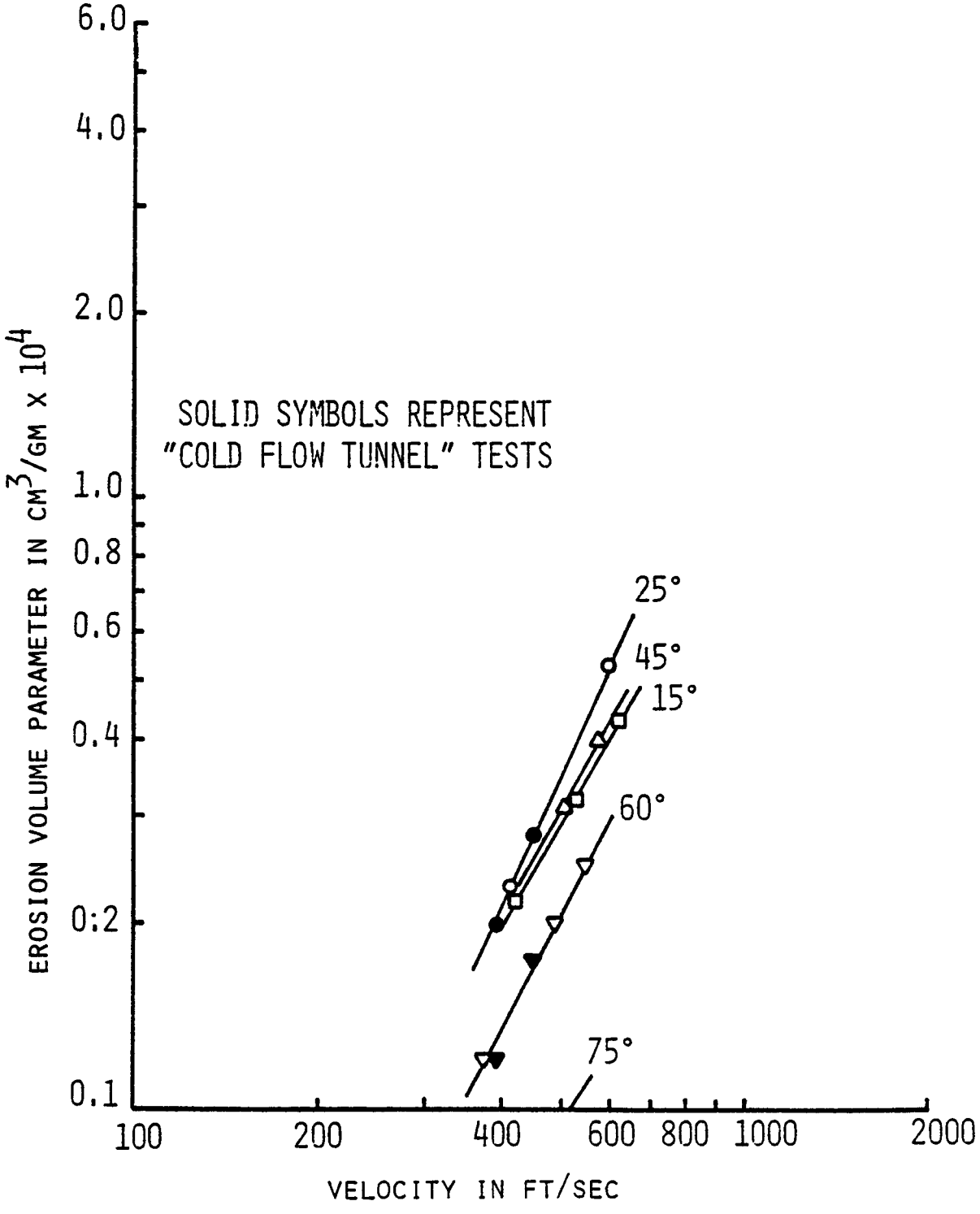

FIG. 4. EFFECT OF VELOCITY ON 304 STEEL AT ROOM TEMPERATURE.

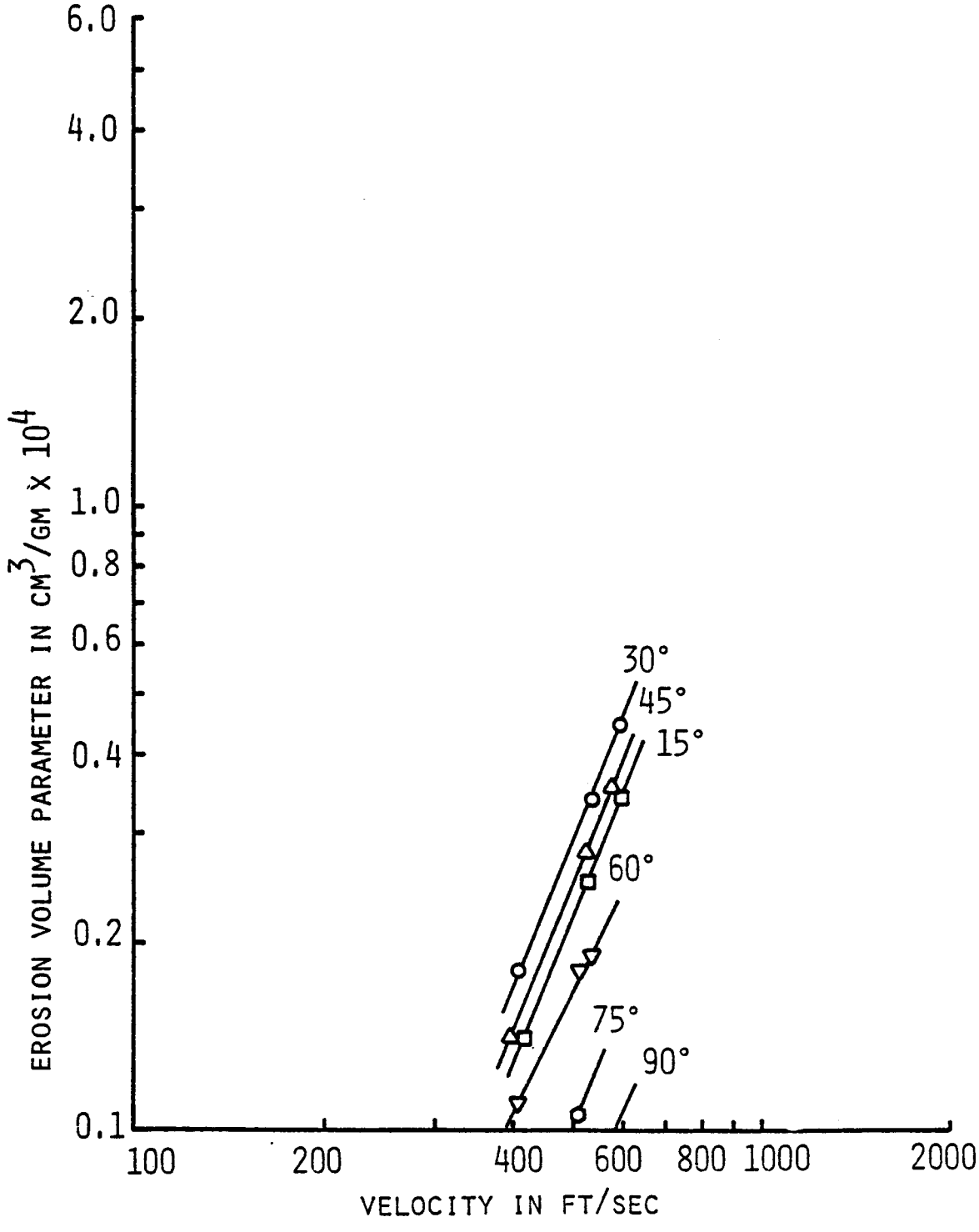

FIG. 5. EFFECT OF VELOCITY ON RENE 41 AT ROOM TEMPERATURE.

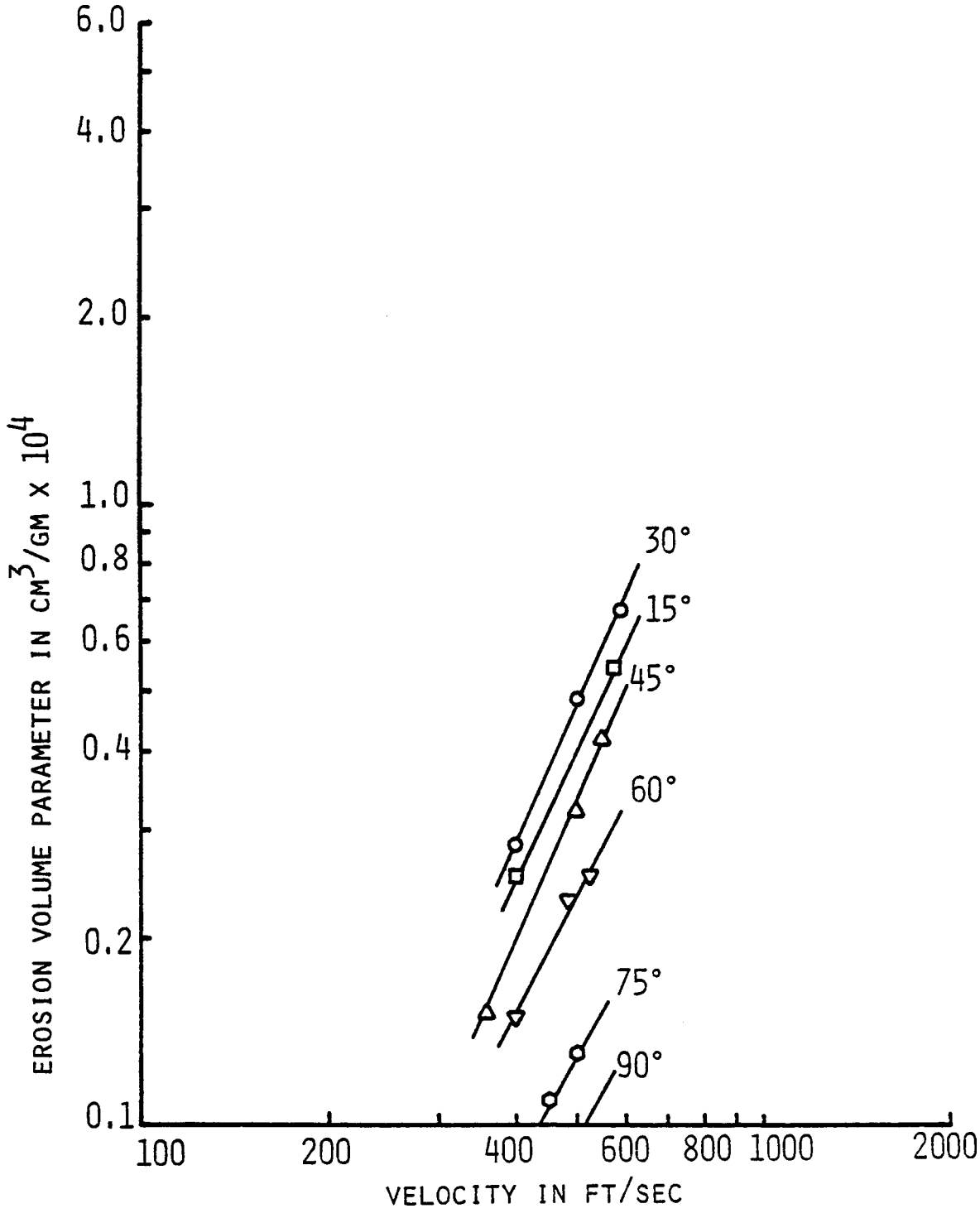

FIG. 6. EFFECT OF VELOCITY ON A286 AT ROOM TEMPERATURE.

TABLE III

SERIES I - ROOM TEMPERATURE

Target Material	Angle of Attack	Erosion Vol. Parameter (in $CM^3/GM \times 10^4$) Particle Velocity = 450 ft/sec	Particle Velocity = 600 ft/sec	Velocity Index 'n'
304 Steel	15	0.245	0.4	1.7
	25	0.28	0.53	2.22
	45	0.255	0.43	1.82
	60	0.17	0.3	1.97
	75	0.08	0.12	1.41
	90	0.06	0.105	1.95
Rene 41	15	0.165	0.34	2.51
	30	0.22	0.45	2.49
	45	0.19	0.38	2.41
	60	0.135	0.24	2.00
	75	0.078	0.155	2.39
	90	0.055	0.105	2.25
A286	15	0.32	0.59	2.13
	30	0.37	0.7	2.22
	45	0.26	0.5	2.27
	60	0.19	0.33	1.92
	75	0.11	0.18	1.71
	90	0.08	0.13	1.69

SERIES II - TESTS AT 300°F

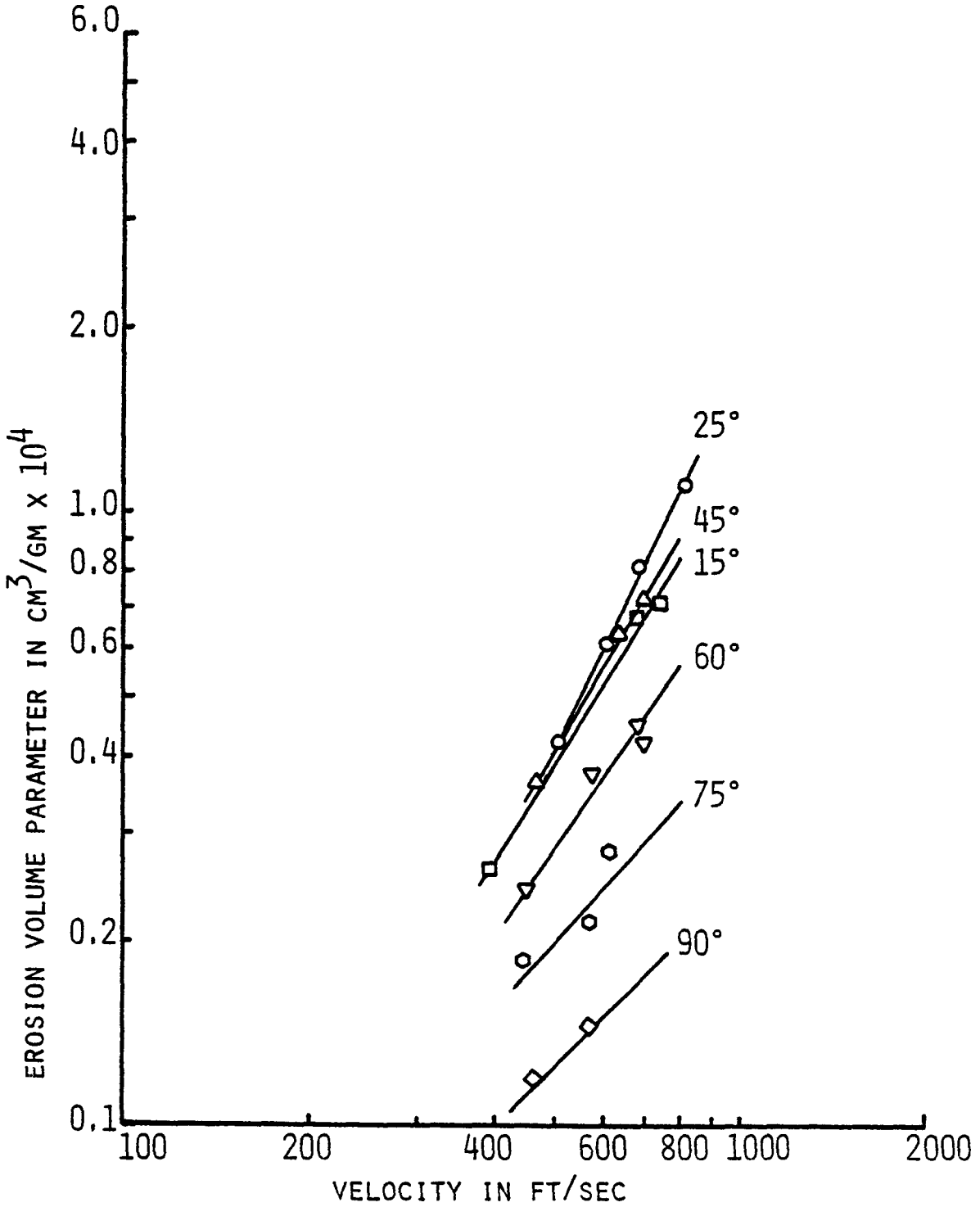

FIG. 7. EFFECT OF VELOCITY ON 304 STEEL AT 300°F.

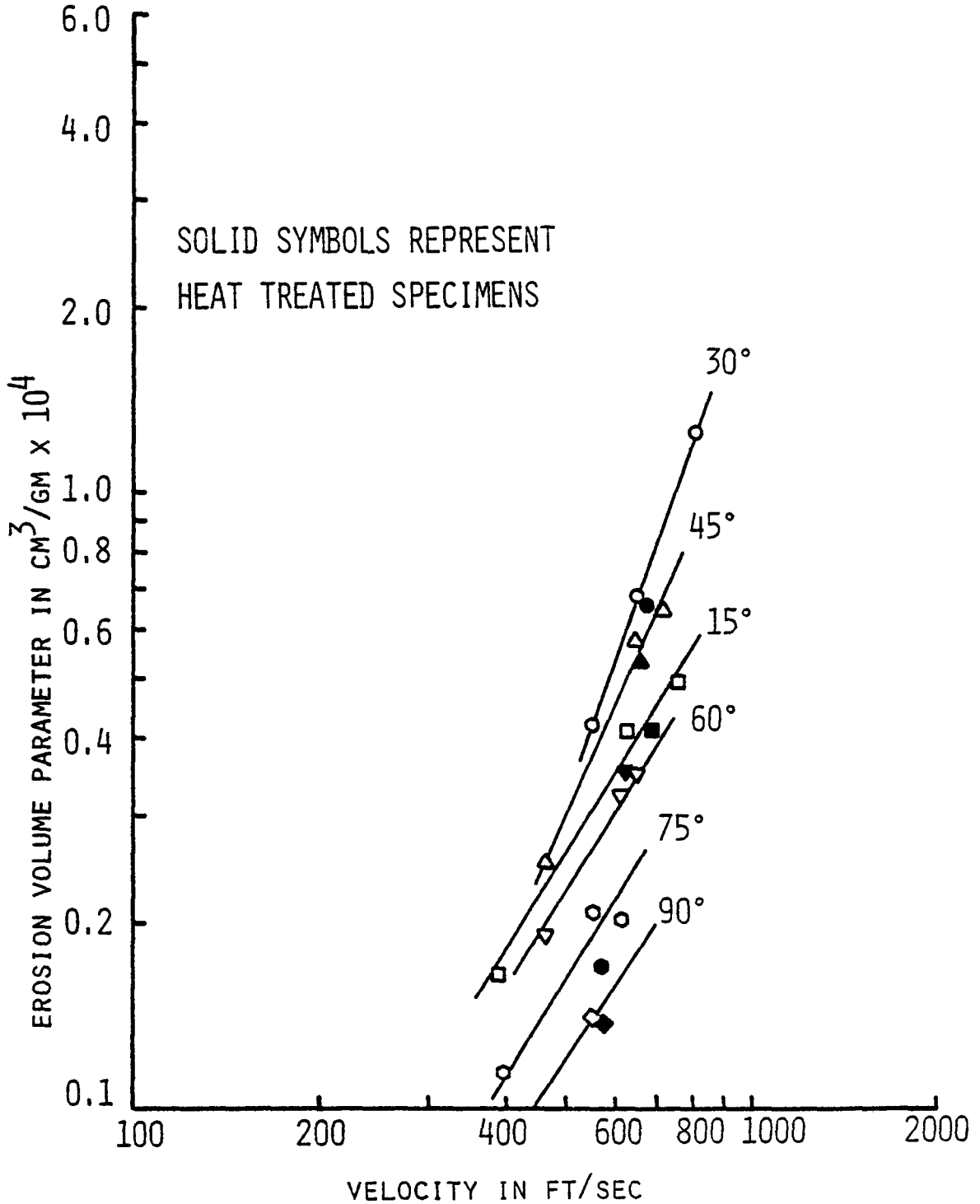

FIG. 8. EFFECT OF VELOCITY ON RENE 41 AT 300°F.

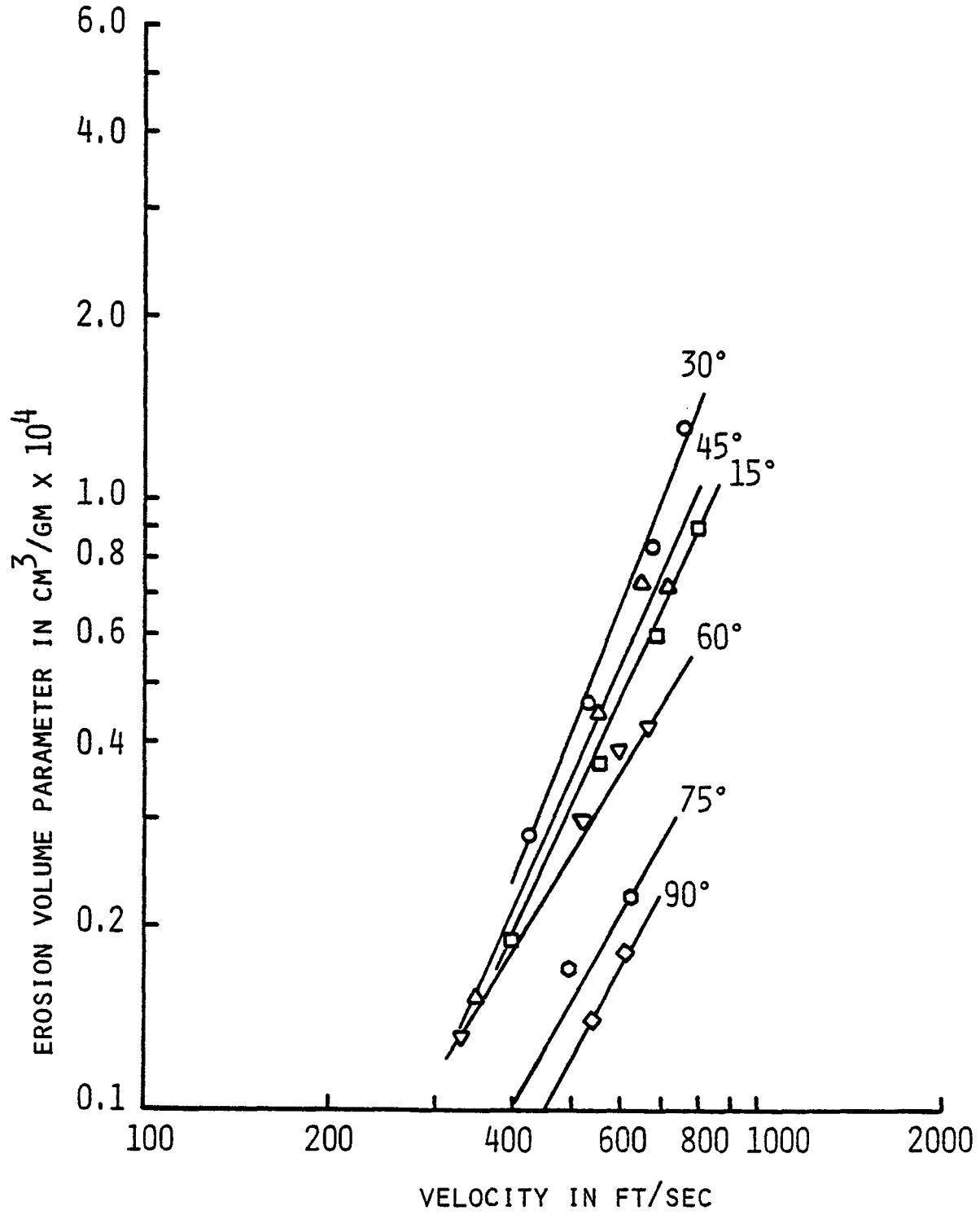

FIG. 9. EFFECT OF VELOCITY ON A286 AT 300°F.

TABLE IV

SERIES II - 300°F

Target Material	Angle of Attack	Erosion Vol. Parameter (in $CM^3/GM \times 10^4$) Particle Velocity = 600 ft/sec	Particle Velocity = 800 ft/sec	Velocity Index 'n'
304 Steel	15	0.52	0.84	1.67
	25	0.6	1.05	1.95
	45	0.54	0.9	1.78
	60	0.37	0.56	1.44
	75	0.24	0.33	1.11
	90	0.15	0.2	1.00
Rene 41	15	0.35	0.56	1.63
	30	0.54	1.2	2.78
	45	0.45	0.88	2.33
	60	0.3	0.47	1.56
	75	0.22	0.34	1.51
	90	0.16	0.24	1.41
A286	15	0.46	0.9	2.33
	30	0.64	1.35	2.59
	45	0.56	1.0	2.02
	60	0.35	0.58	1.76
	75	0.21	0.35	1.78
	90	0.165	0.29	1.96

SERIES III - TESTS AT 600°F

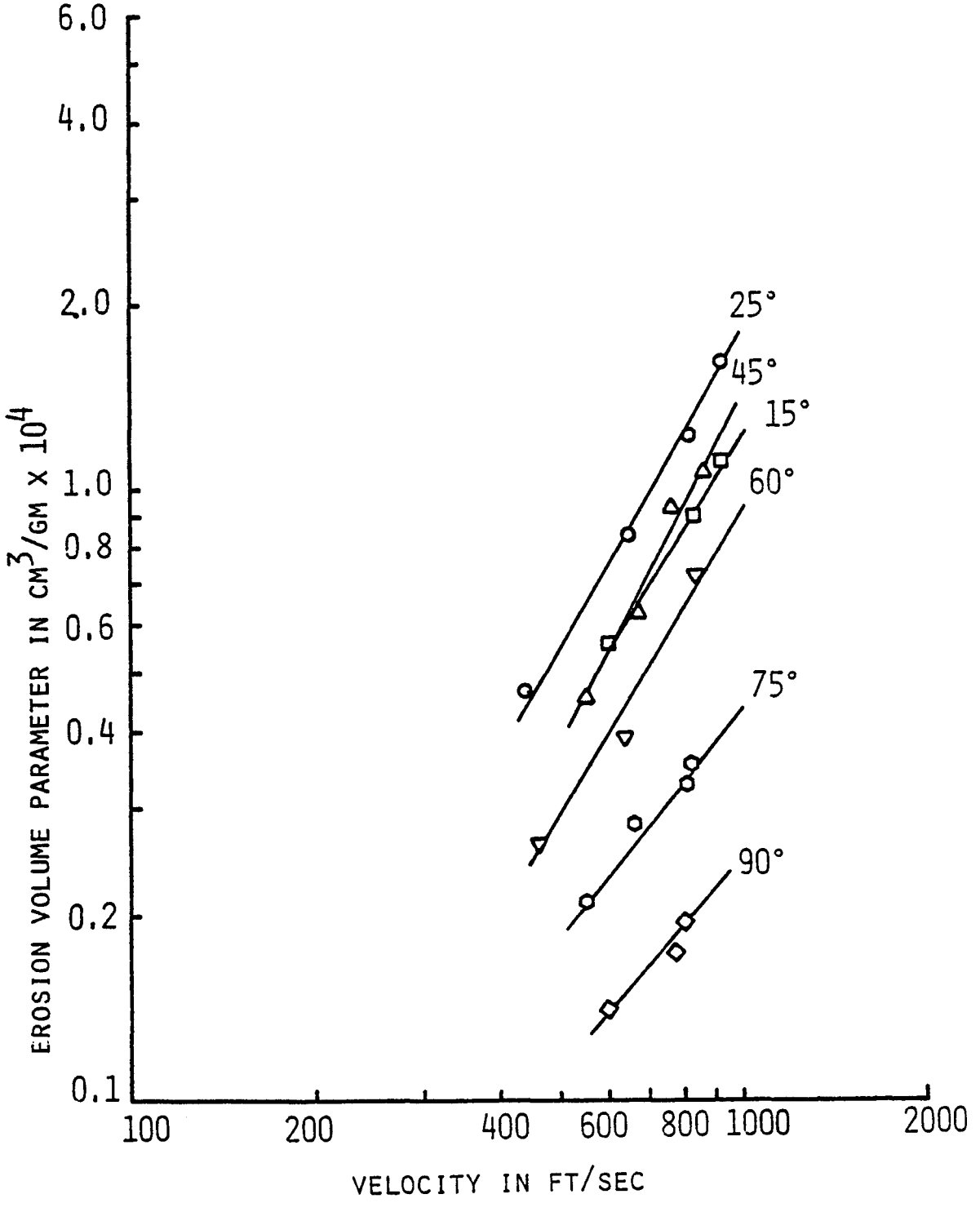

FIG. 10. EFFECT OF VELOCITY ON 304 STEEL AT 600°F.

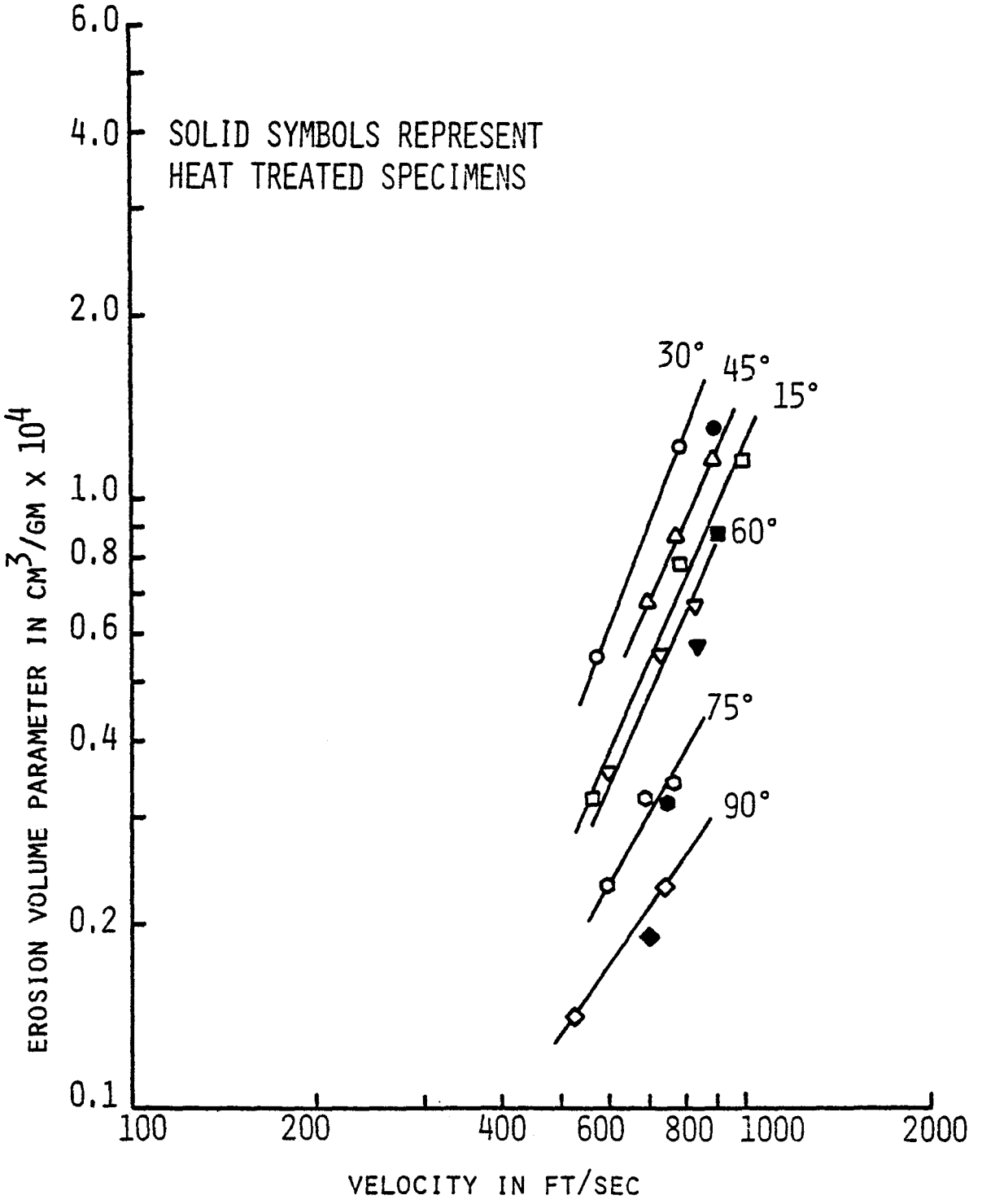

FIG. 11. EFFECT OF VELOCITY ON RENE 41 AT 600°F.

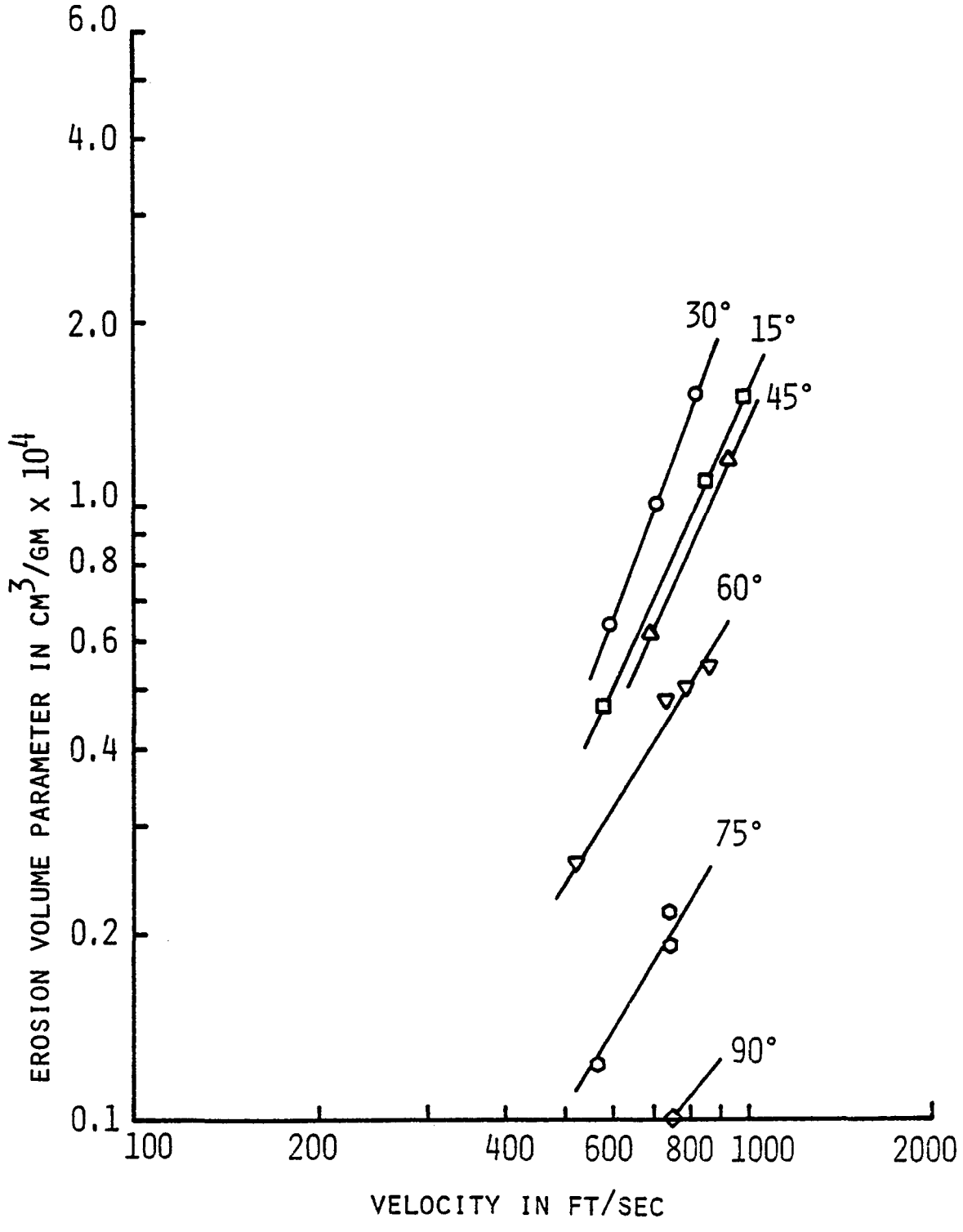

FIG. 12. EFFECT OF VELOCITY ON A286 AT 600°F.

TABLE V

SERIES III - 600°F

Target Material	Angle of Attack	Erosion Vol. Parameter ($in\ CM^3/GM \times 10^4$) Particle Velocity (in ft/sec) 600	800	1000	Velocity Index 'n'
304 Steel	15	0.54	0.86	1.2	1.56
	25	0.74	1.25	1.8	1.74
	45	0.54	0.92	1.4	1.86
	60	0.39	0.64	0.9	1.64
	75	0.24	0.33	0.44	1.19
	90	0.14	0.2	0.25	1.14
Rene 41	15	0.37	0.72	1.2	2.3
	30	0.6	1.3	2.3	2.63
	45	0.48	0.92	1.5	2.23
	60	0.33	0.64	1.05	2.27
	75	0.23	0.38	0.56	1.74
	90	0.17	0.26	0.35	1.41
A286	15	0.5	0.92	1.5	2.15
	30	0.64	1.4	2.45	2.63
	45	0.44	0.82	1.35	2.19
	60	0.34	0.5	0.7	1.41
	75	0.14	0.225	0.32	1.62
	90	0.072	0.11	0.145	1.37

SERIES IV - TESTS AT 900°F

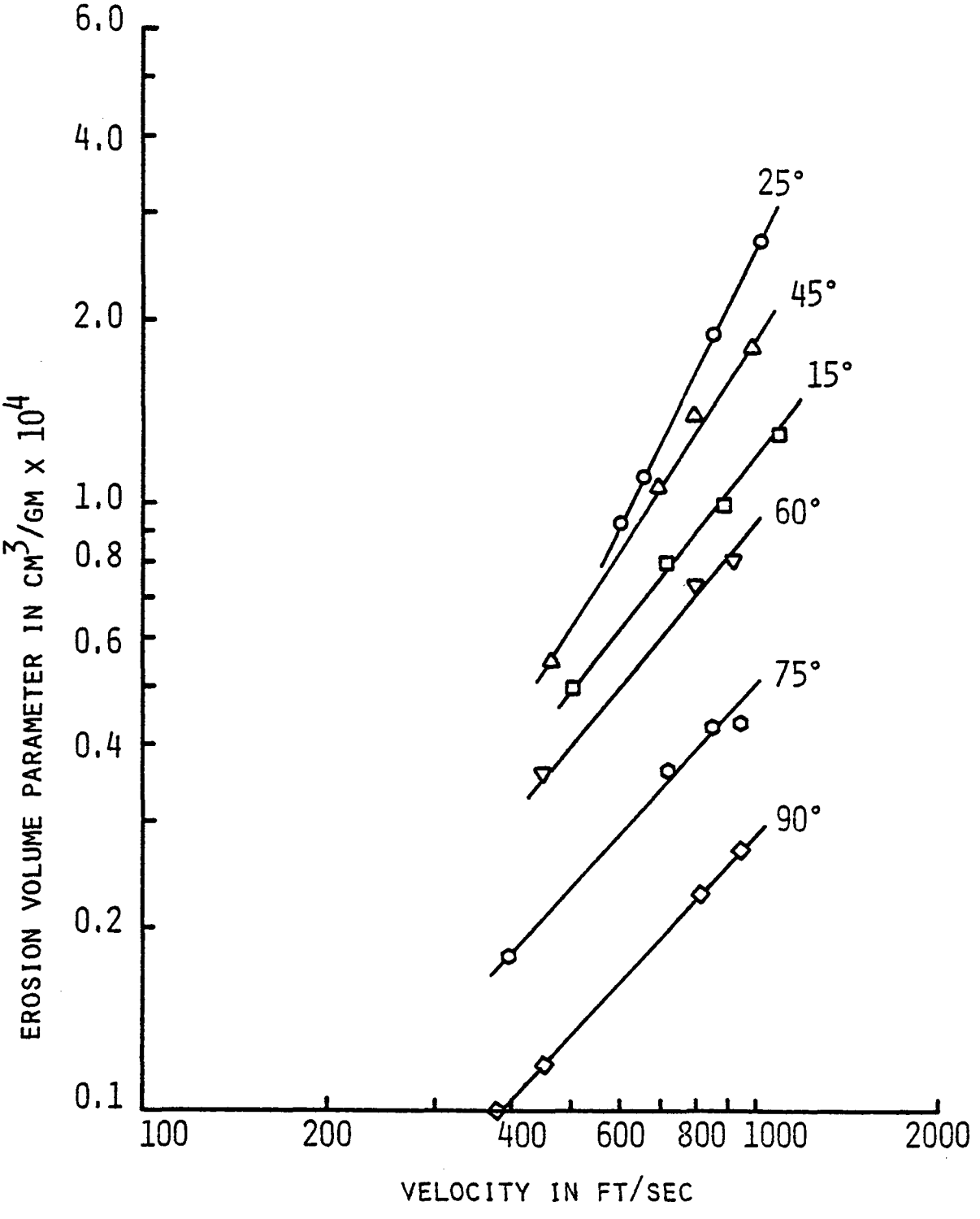

FIG. 13. EFFECT OF VELOCITY ON 304 STEEL AT 900°F.

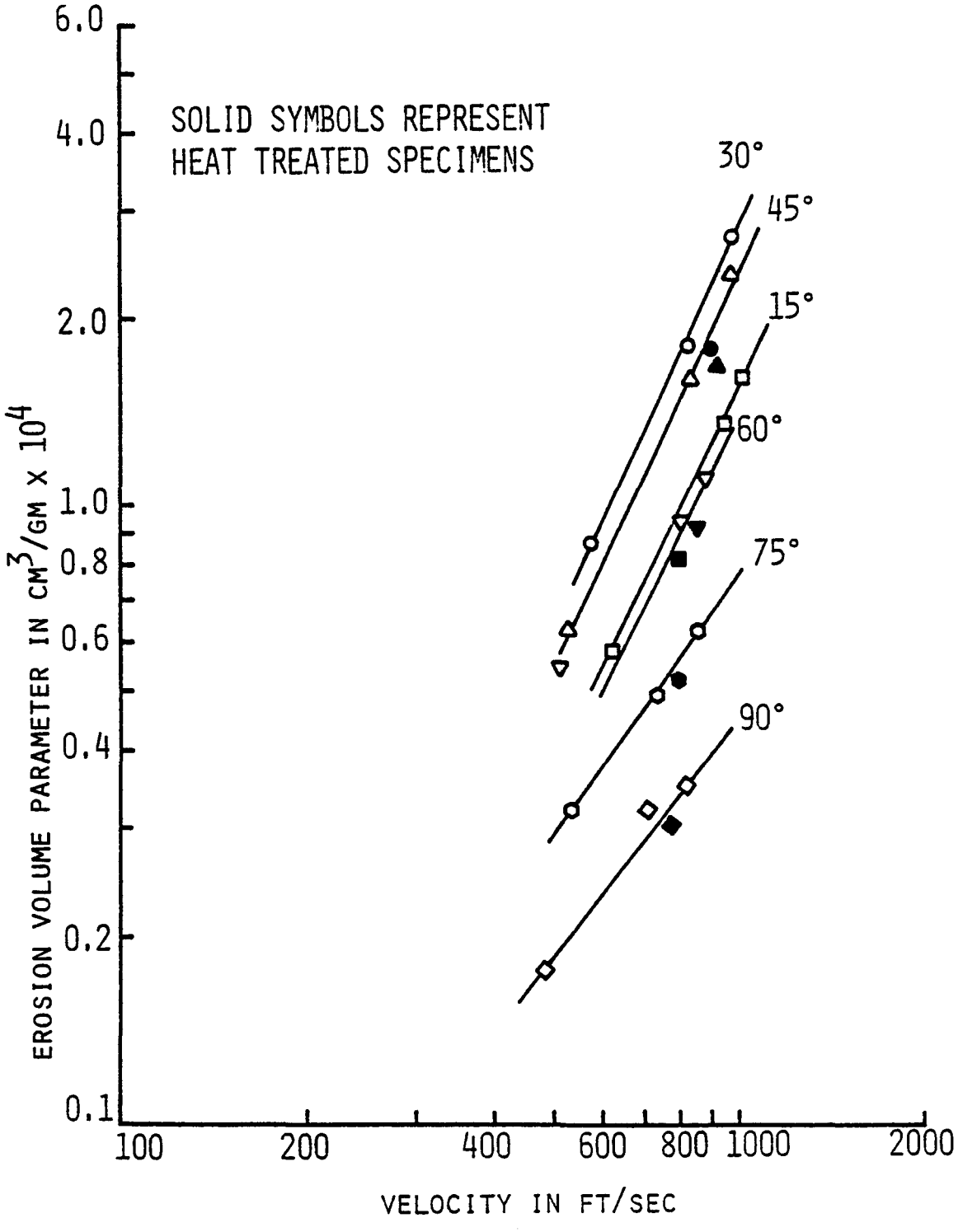

FIG. 14. EFFECT OF VELOCITY ON RENE 41 AT 900°F.

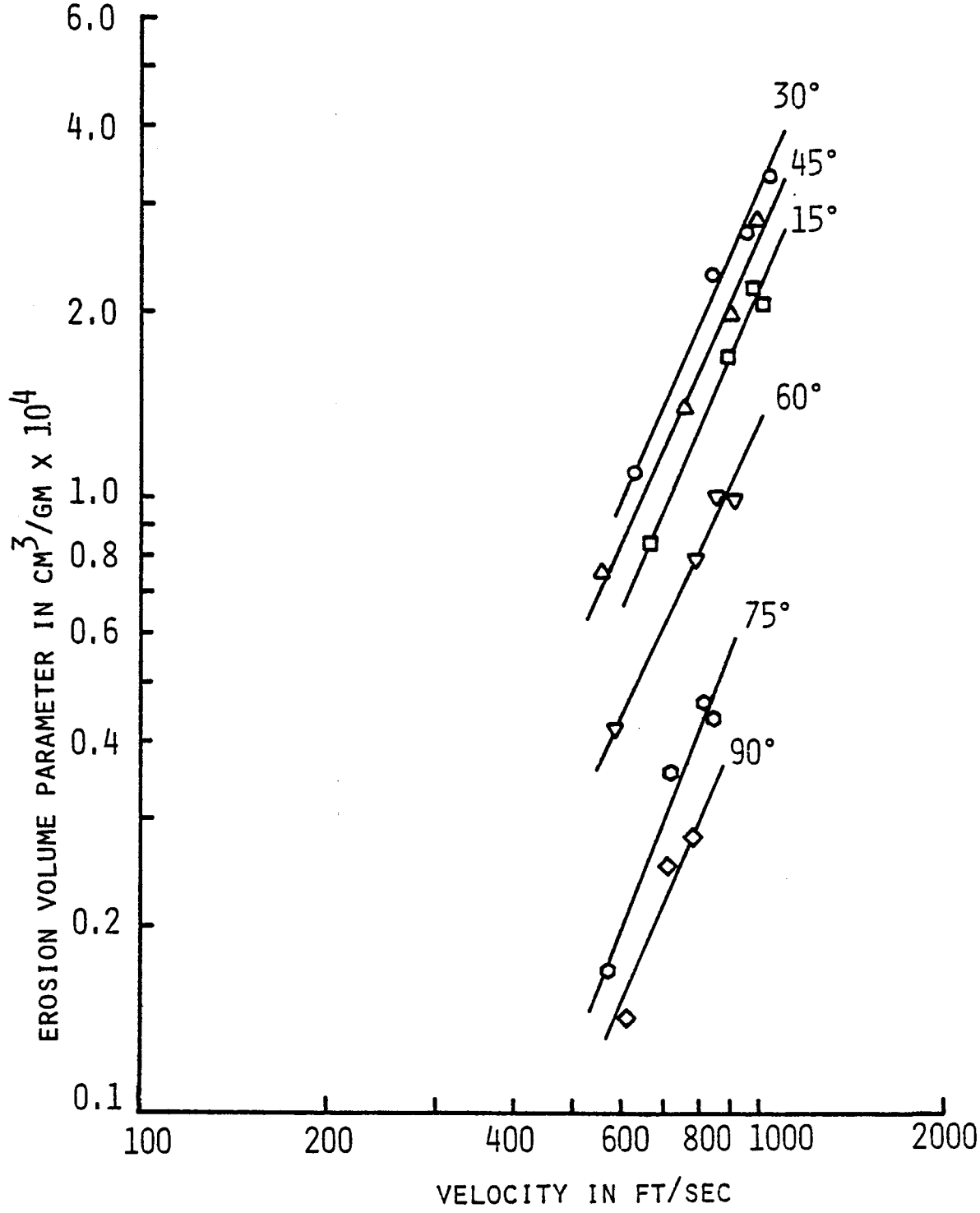

FIG. 15. EFFECT OF VELOCITY ON A286 AT 900°F.

TABLE VI

SERIES IV - 900°F

Target Material	Angle of Attack	Erosion Vol. Parameter (in $CM^3/GM \times 10^4$) Particle Velocity (in ft/sec) 600	800	1000	Velocity Index 'n'
304 Steel	15	0.61	0.88	1.2	1.32
	25	0.9	1.6	2.6	2.08
	45	0.82	1.3	1.8	1.54
	60	0.5	0.7	0.9	1.15
	75	0.285	0.39	0.5	1.10
	90	0.165	0.225	0.285	1.07
Rene 41	15	0.55	0.98	1.5	1.96
	30	0.94	1.8	2.9	2.21
	45	0.8	1.5	2.4	2.15
	60	0.5	0.88	1.45	2.08
	75	0.37	0.57	0.78	1.46
	90	0.235	0.34	0.455	1.29
A286	15	0.68	1.3	2.1	2.21
	30	0.9	1.9	3.0	2.36
	45	0.84	1.6	2.6	2.21
	60	0.44	0.8	1.25	2.04
	75	0.19	0.42	0.72	2.61
	90	0.15	0.3	0.5	2.36

SERIES V - TESTS AT 1200°F

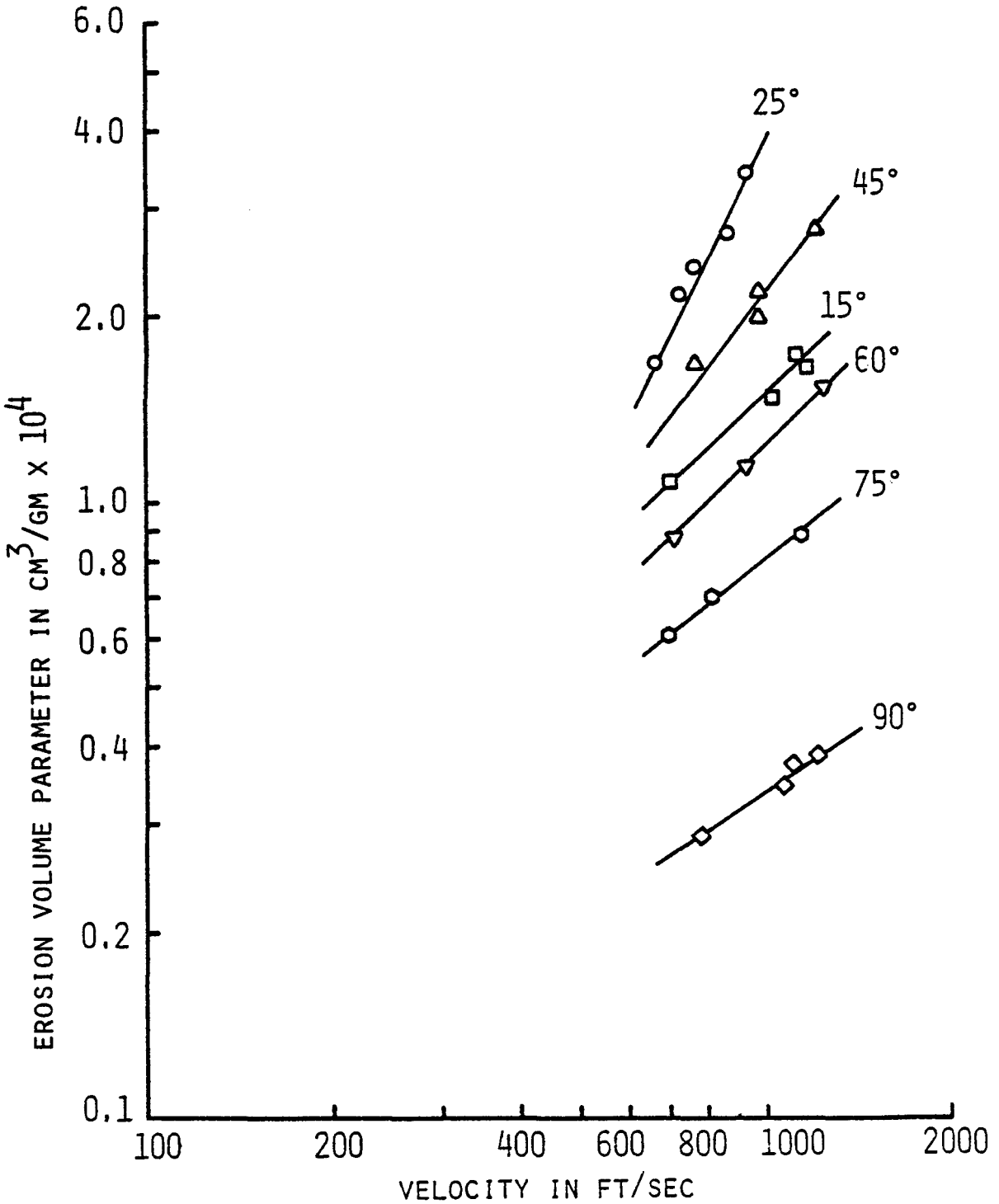

FIG. 16. EFFECT OF VELOCITY ON 304 STEEL AT 1200°F.

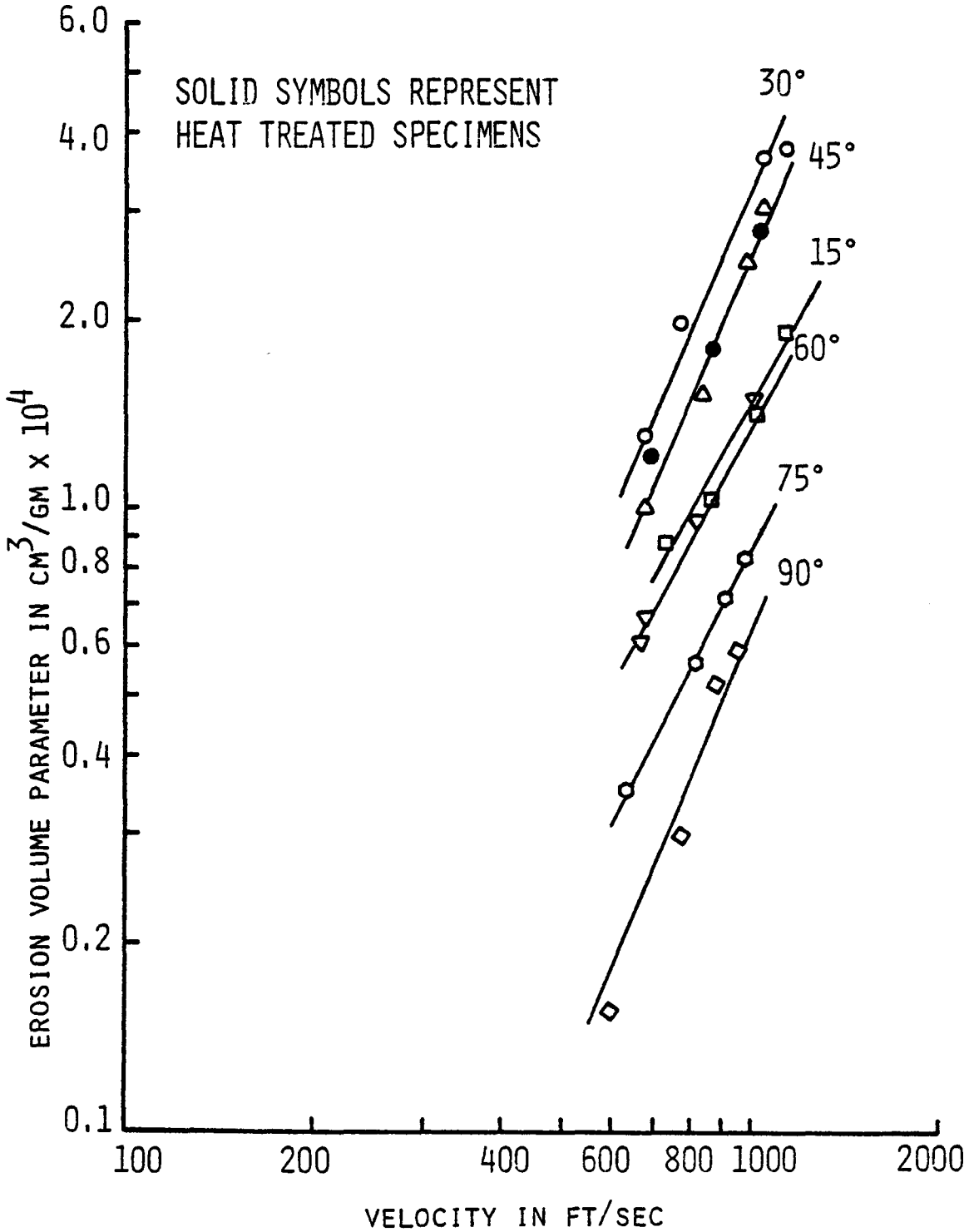

FIG. 17. EFFECT OF VELOCITY ON RENE 41 AT 1200°F

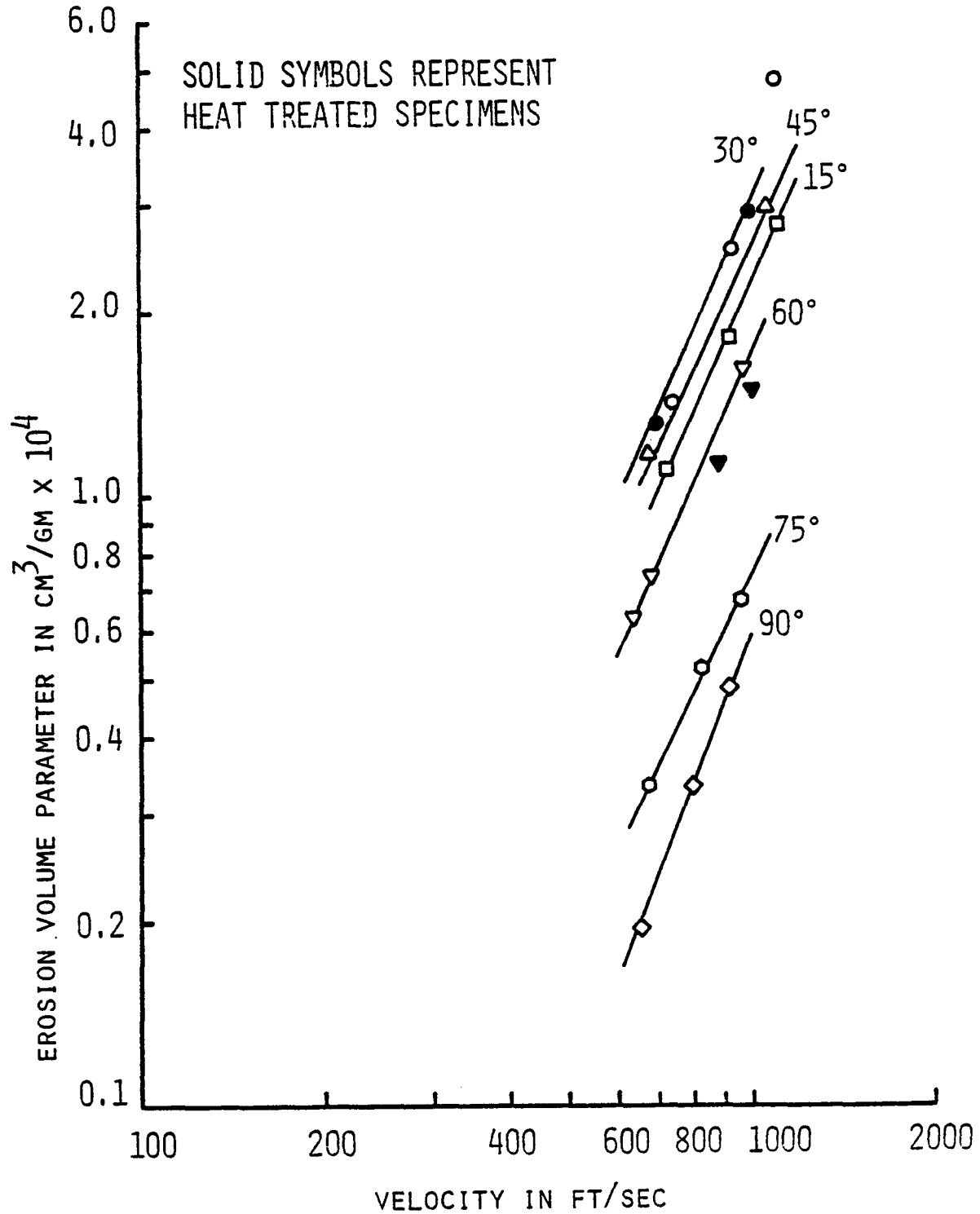

FIG. 18. EFFECT OF VELOCITY ON A286 AT 1200°F.

TABLE VII

SERIES V - 1200°F

Target Material	Angle of Attack	Erosion Vol. Parameter (in $CM^3/GM \times 10^4$) Particle Velocity (in ft/sec) 600	800	1000	Velocity Index 'n'
304 Steel	15	0.92	1.2	1.5	0.96
	25	1.35	2.5	3.9	2.08
	45	1.1	1.65	2.2	1.36
	60	0.76	1.0	1.2	0.89
	75	0.54	0.68	0.8	0.77
	90	0.24	0.29	0.34	0.68
Rene 41	15	0.59	0.98	1.5	1.83
	30	0.98	1.9	3.3	2.38
	45	0.8	1.5	2.5	2.23
	60	0.51	0.88	1.35	1.91
	75	0.31	0.55	0.86	2.00
	90	0.17	0.36	0.62	2.53
A286	15	0.72	1.35	2.2	2.19
	30	1.0	1.7	3.2	2.28
	45	0.84	1.6	2.6	2.21
	60	0.54	1.05	1.7	2.25
	75	0.26	0.46	0.72	1.99
	90	0.16	0.34	0.58	2.52

EROSION CHARACTERISTICS OF 304 STAINLESS STEEL

(WITH RESPECT TO ANGLE OF ATTACK)

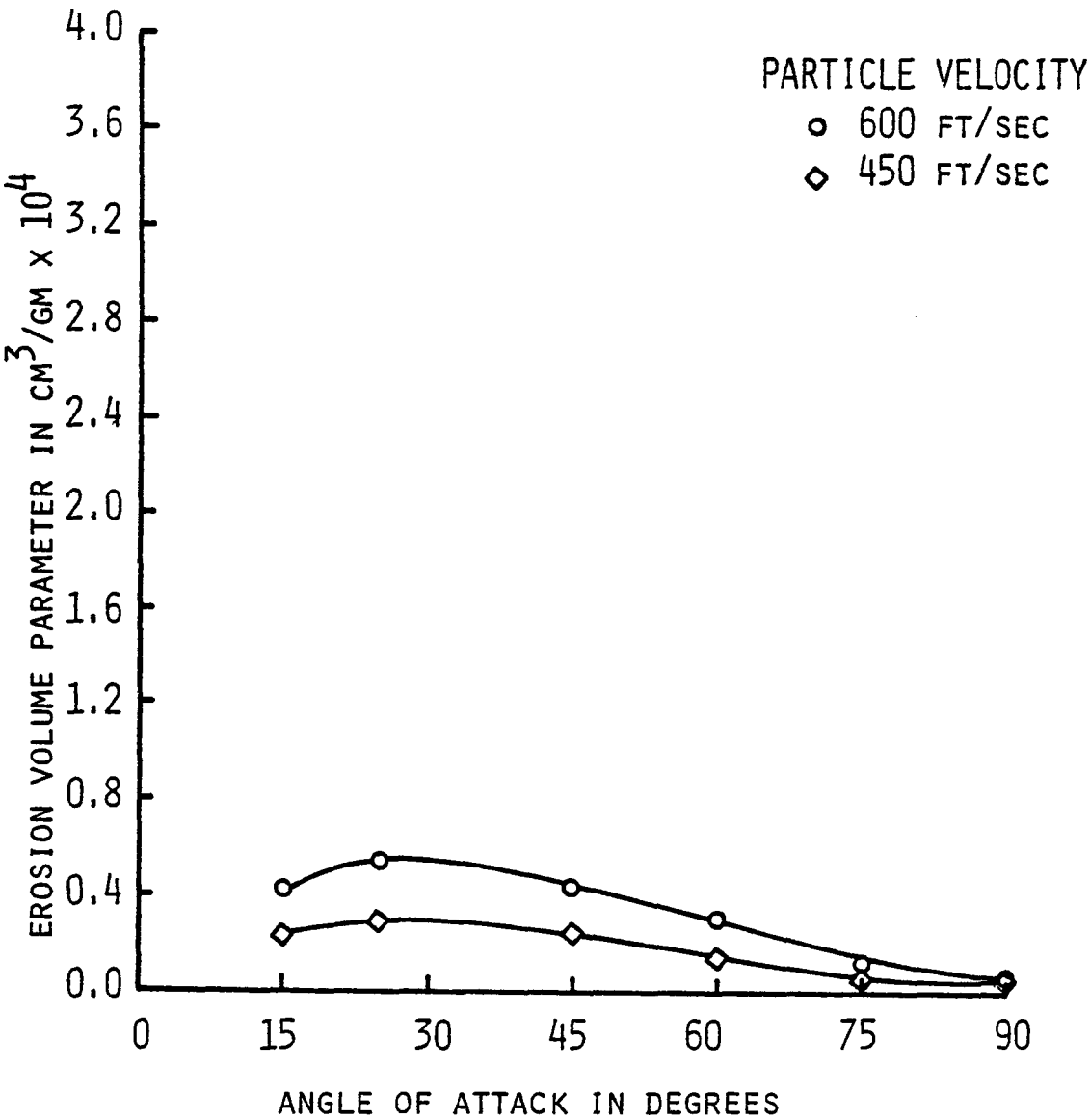

FIG. 19. EFFECT OF ANGLE OF ATTACK ON 304 STEEL AT ROOM TEMPERATURE.

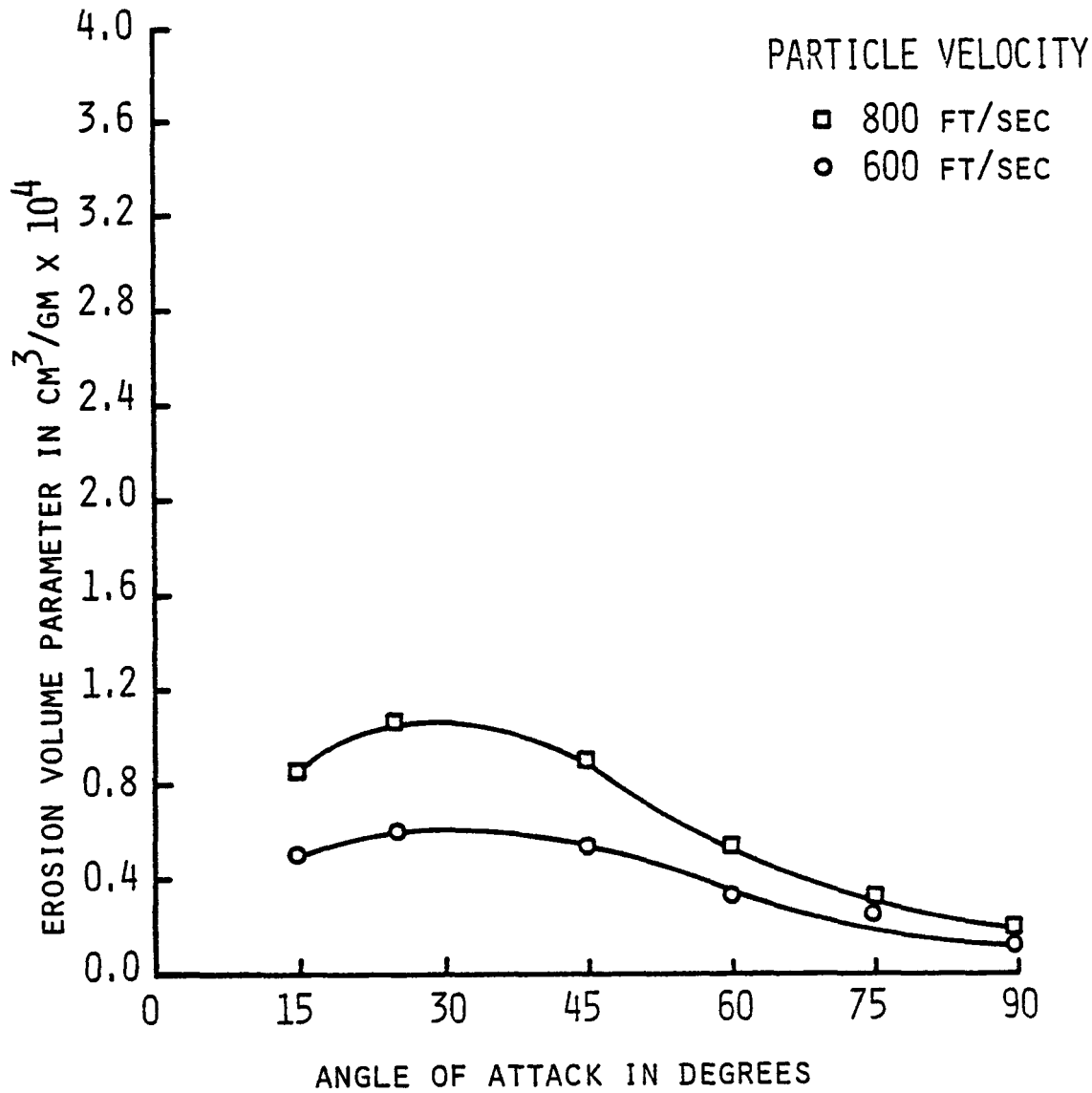

FIG. 20. EFFECT OF ANGLE OF ATTACK ON 304 STEEL AT 300°F.

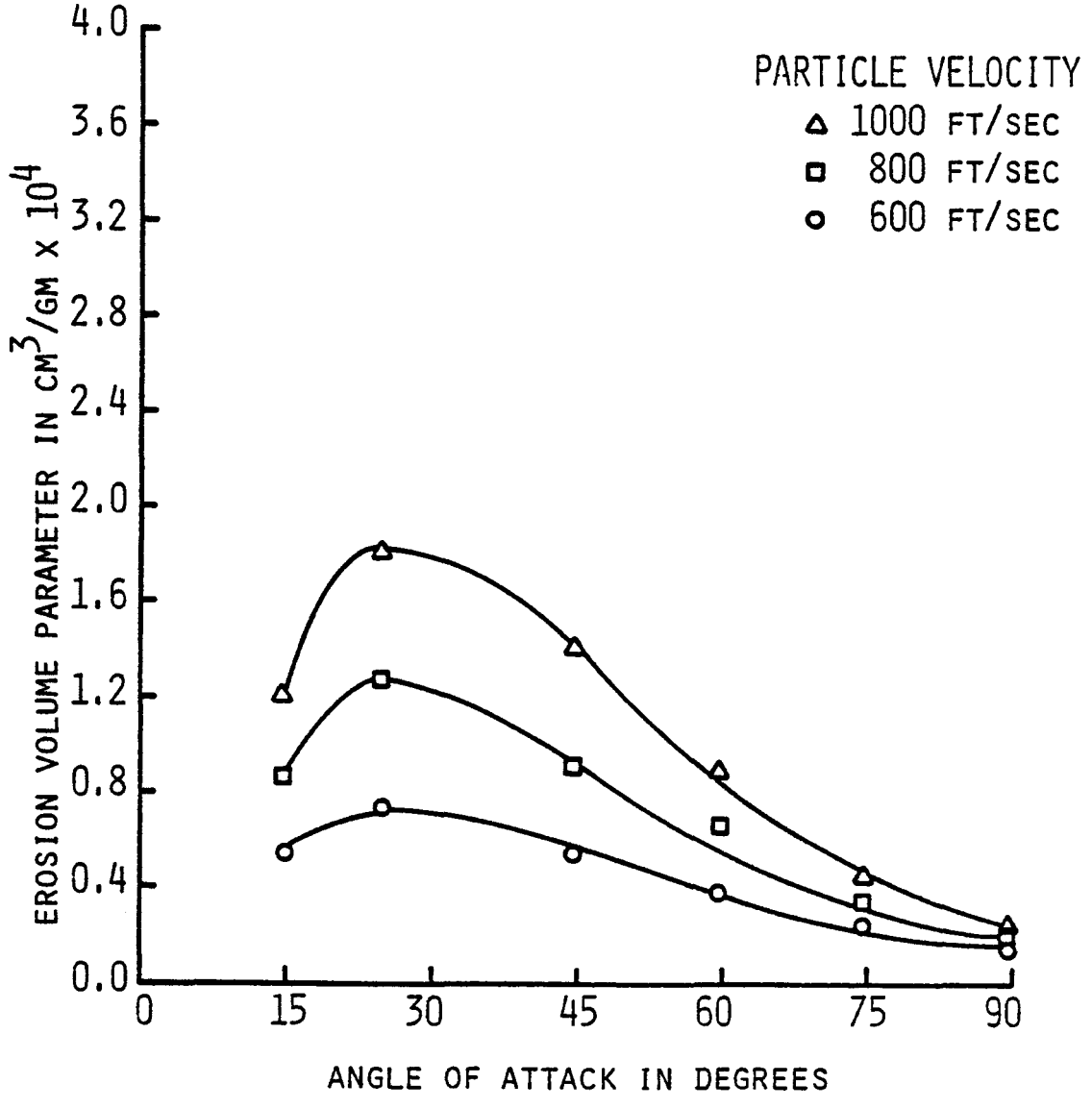

FIG. 21. EFFECT OF ANGLE OF ATTACK ON 304 STEEL AT 600°F.

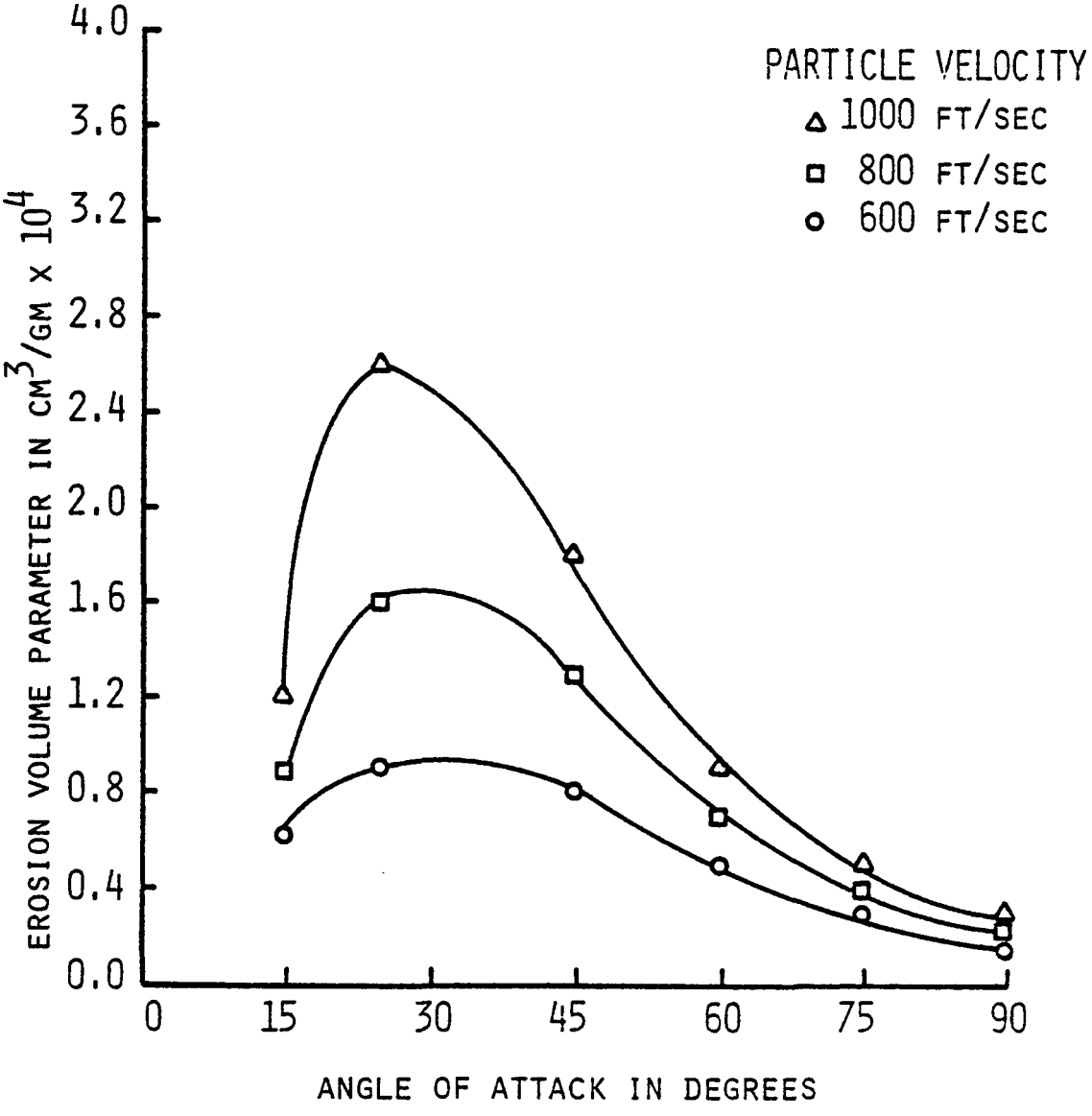

FIG. 22. EFFECT OF ANGLE OF ATTACK ON 304 STEEL AT 900°F.

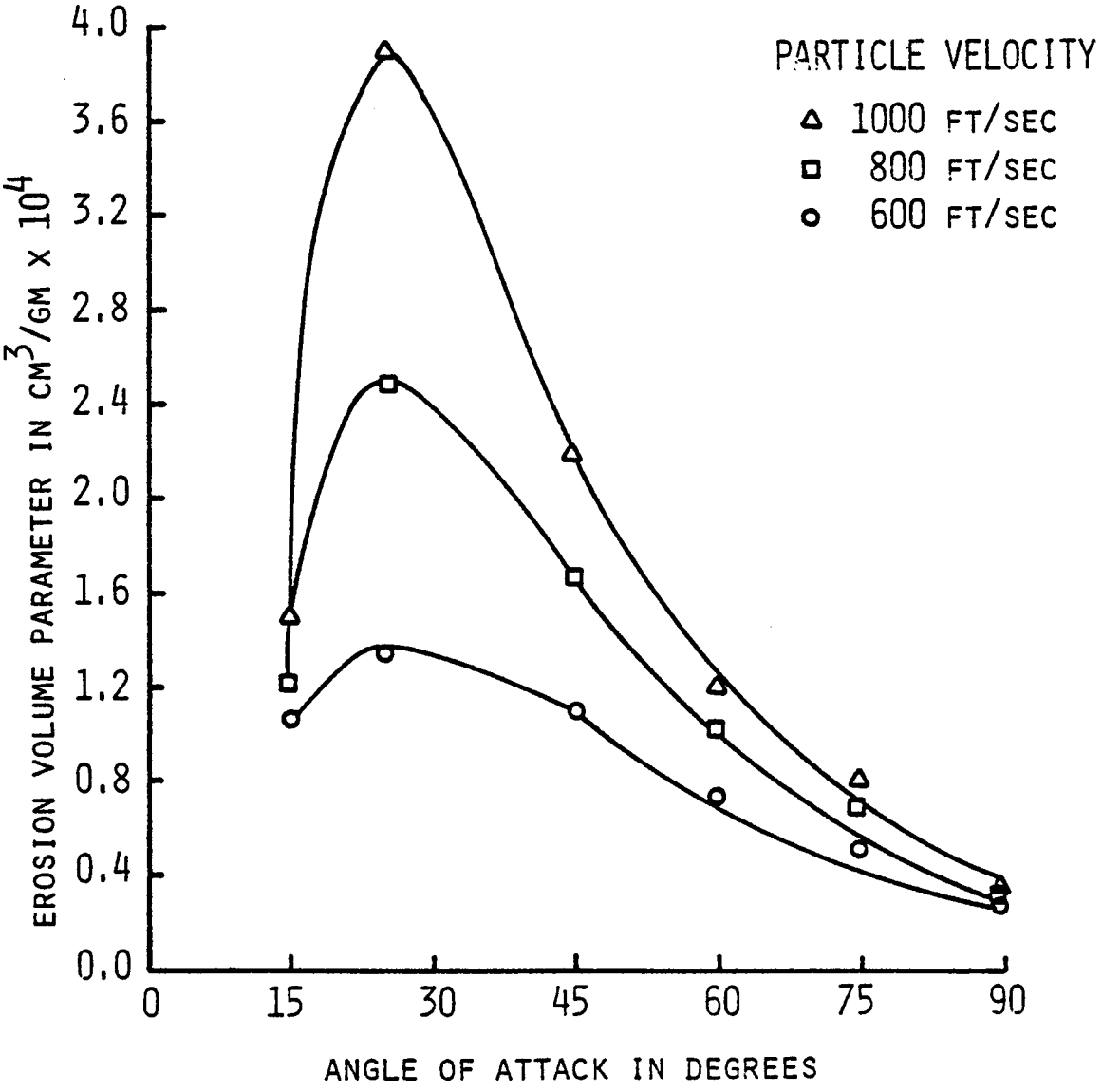

FIG. 23. EFFECT OF ANGLE OF ATTACK ON 304 STEEL AT 1200°F.

EROSION CHARACTERISTICS OF RENE 41

(WITH RESPECT TO ANGLE OF ATTACK)

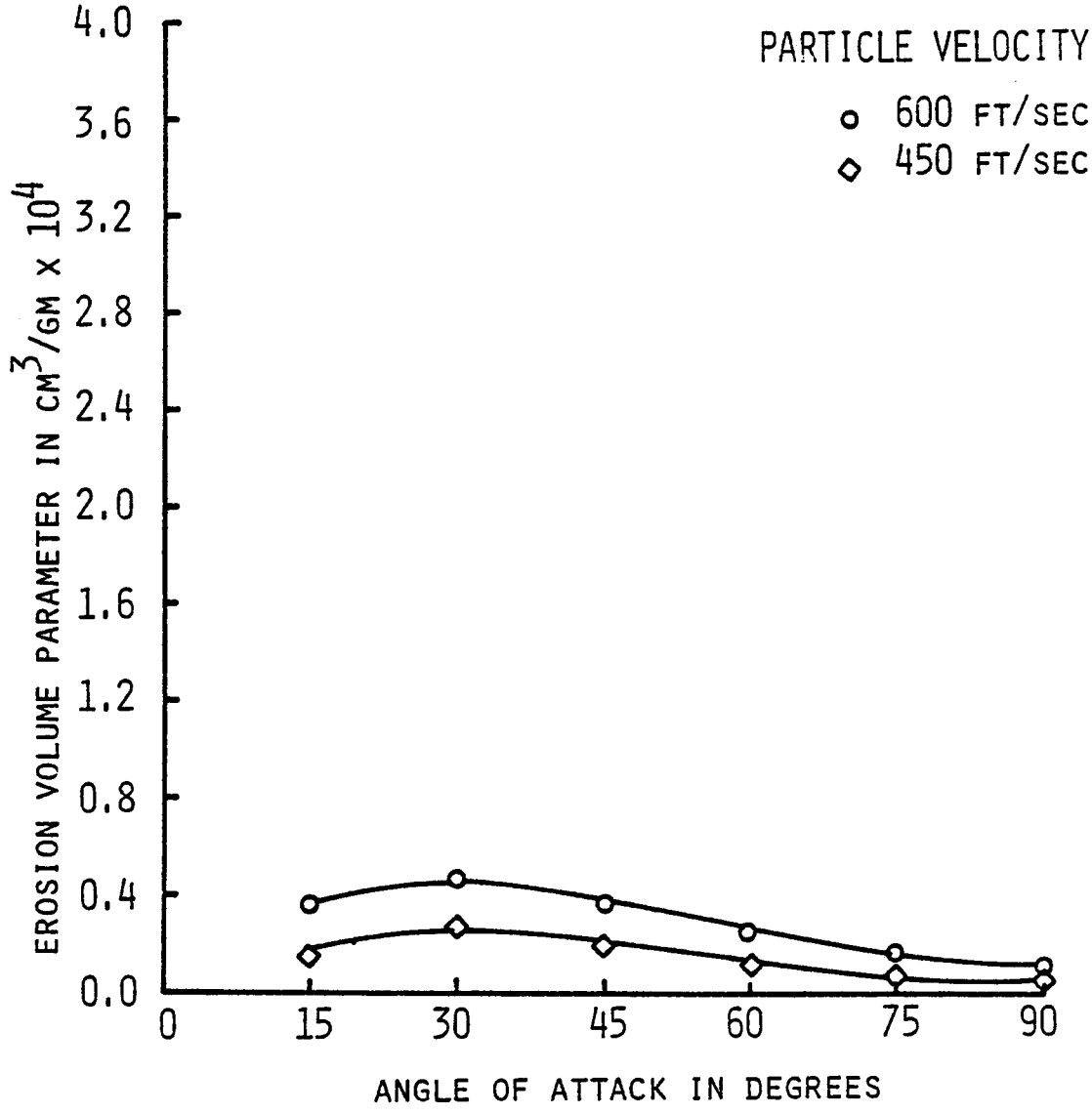

FIG. 24. EFFECT OF ANGLE OF ATTACK ON RENE 41 AT ROOM TEMPERATURE.

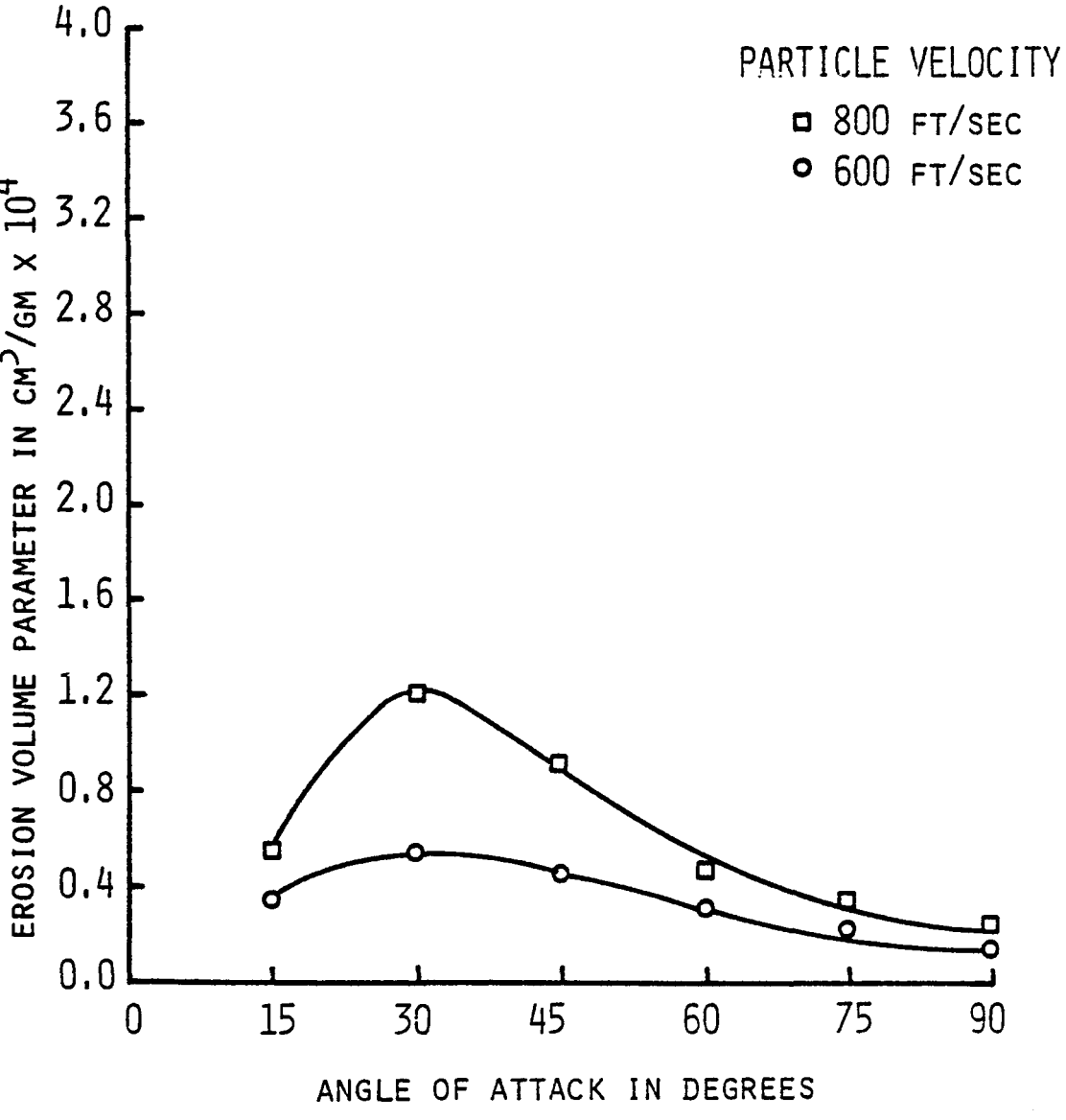

FIG. 25. EFFECT OF ANGLE OF ATTACK ON RENE 41 AT 300°F.

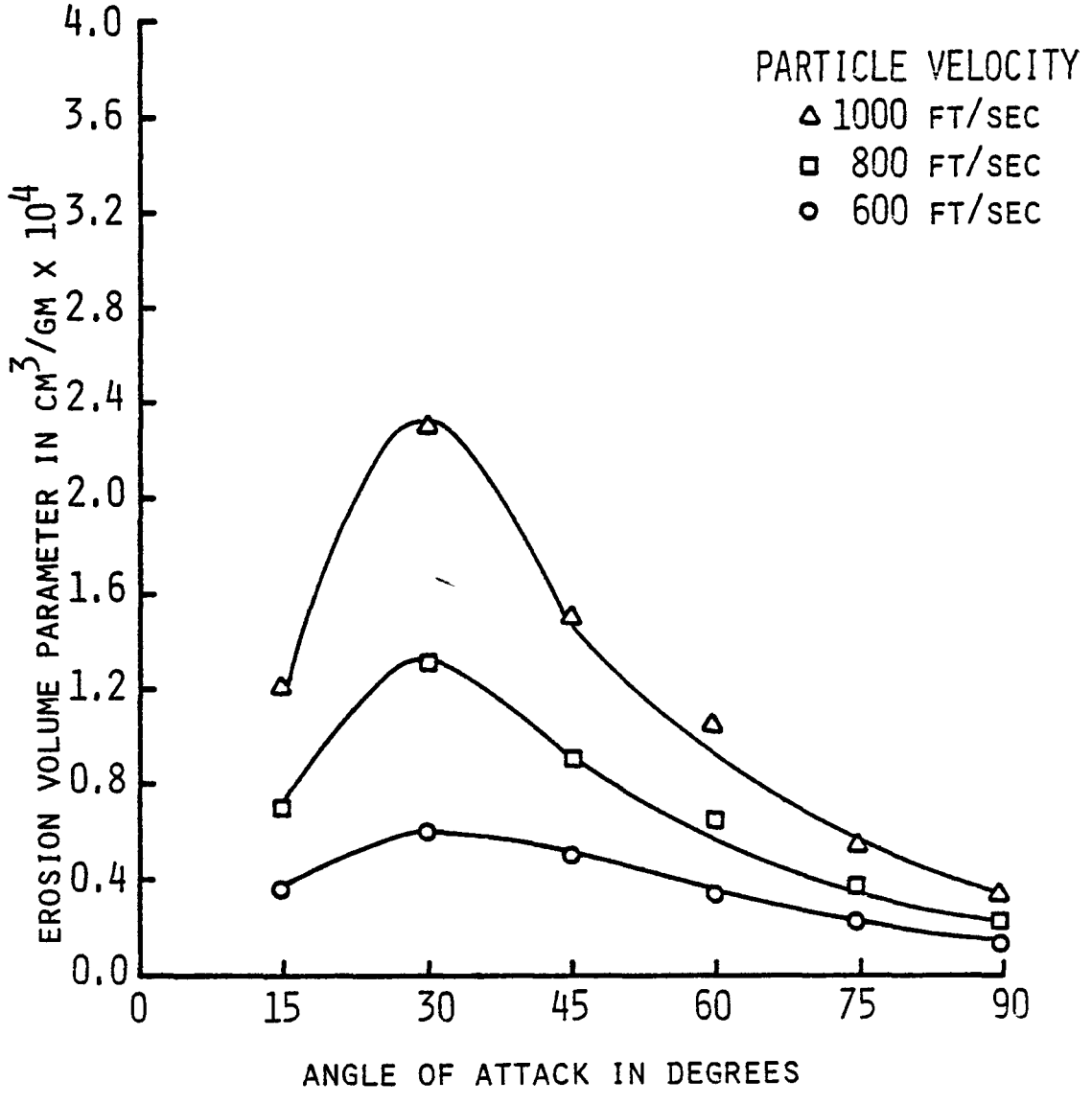

FIG. 26. EFFECT OF ANGLE OF ATTACK ON RENE 41 AT 600°F.

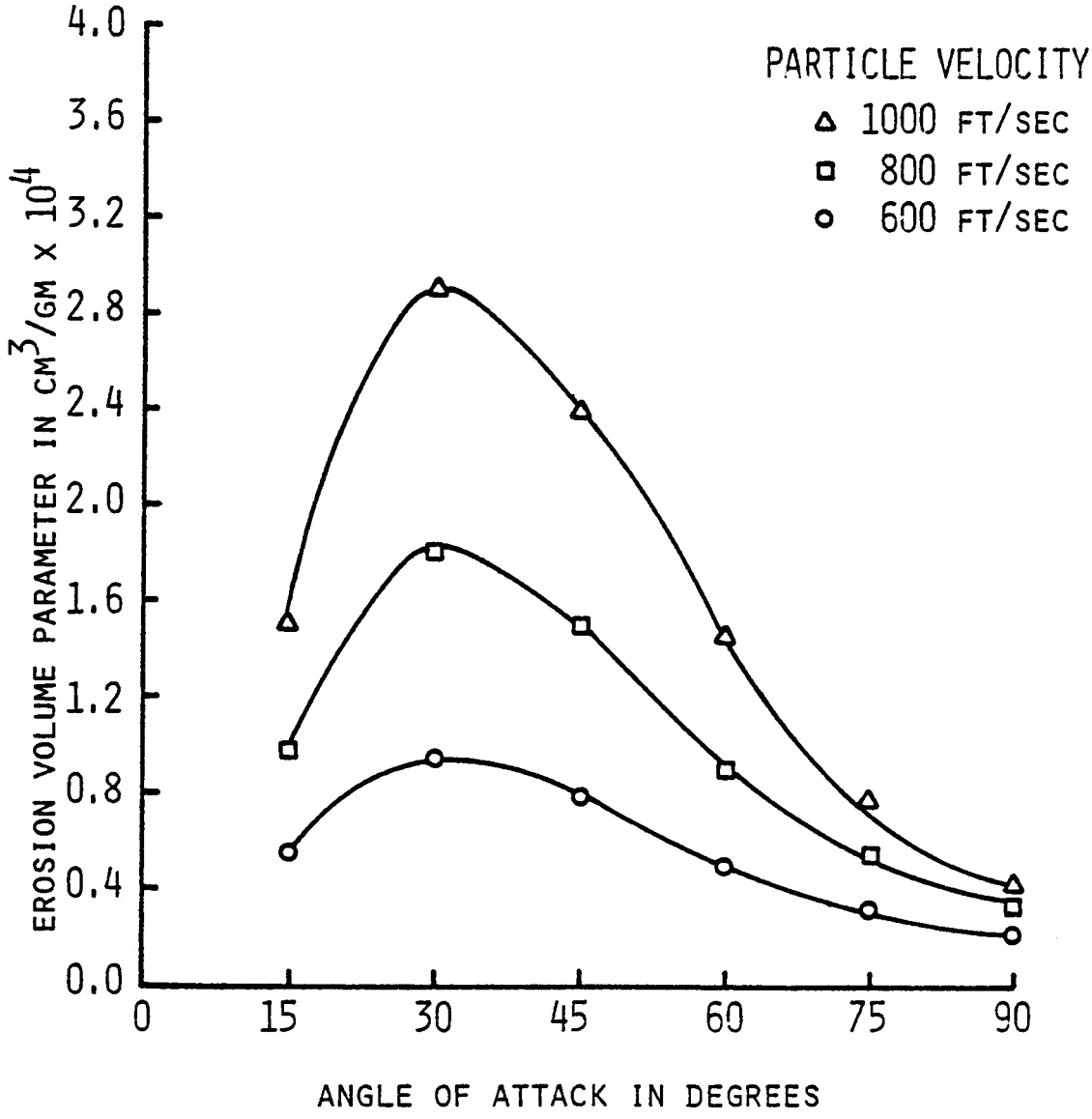

FIG. 27. EFFECT OF ANGLE OF ATTACK ON RENE 41 AT 900°F.

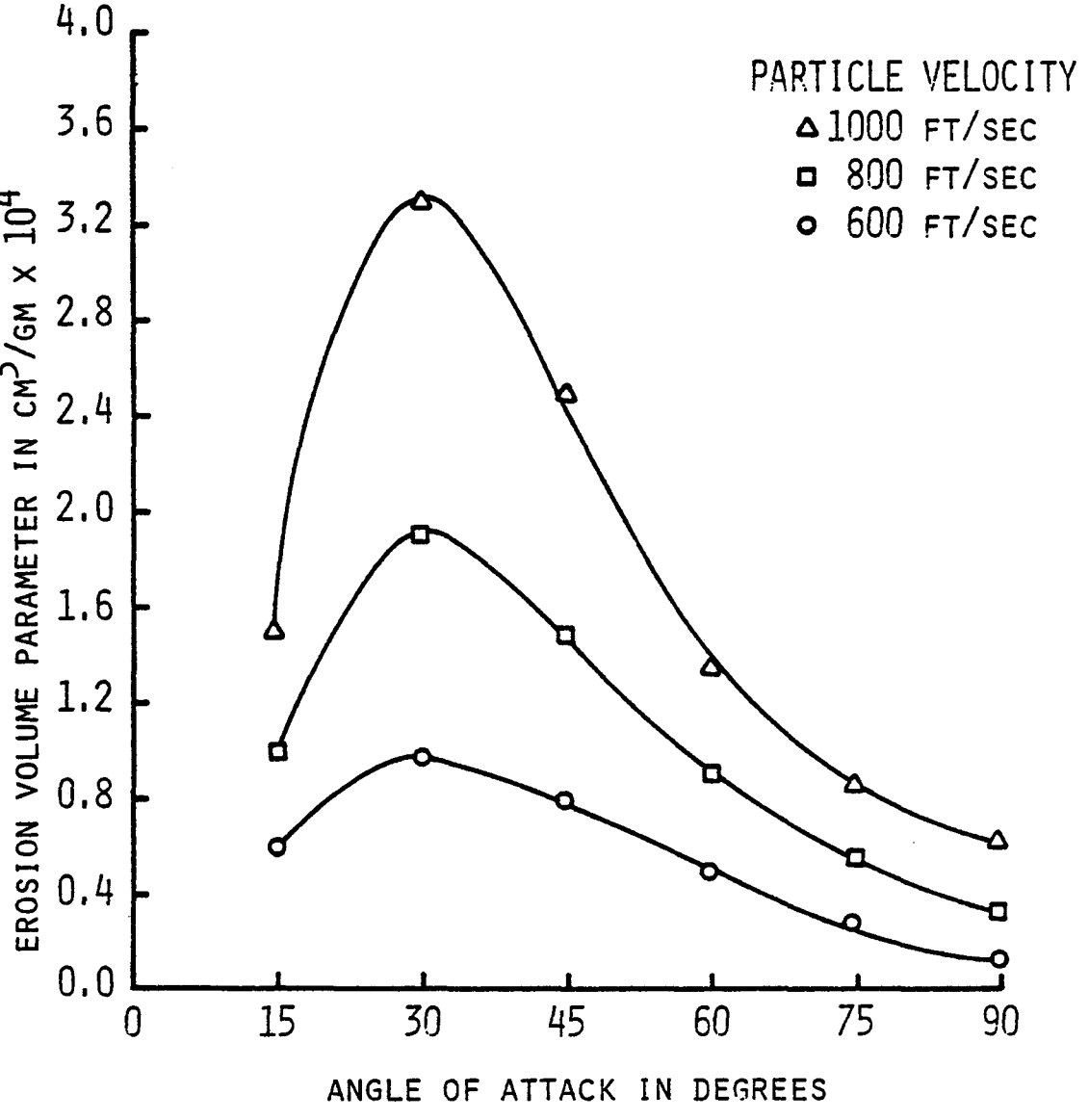

FIG. 28. EFFECT OF ANGLE OF ATTACK ON RENE 41 AT 1200°F.

EROSION CHARACTERISTICS OF A286

(WITH RESPECT TO ANGLE OF ATTACK)

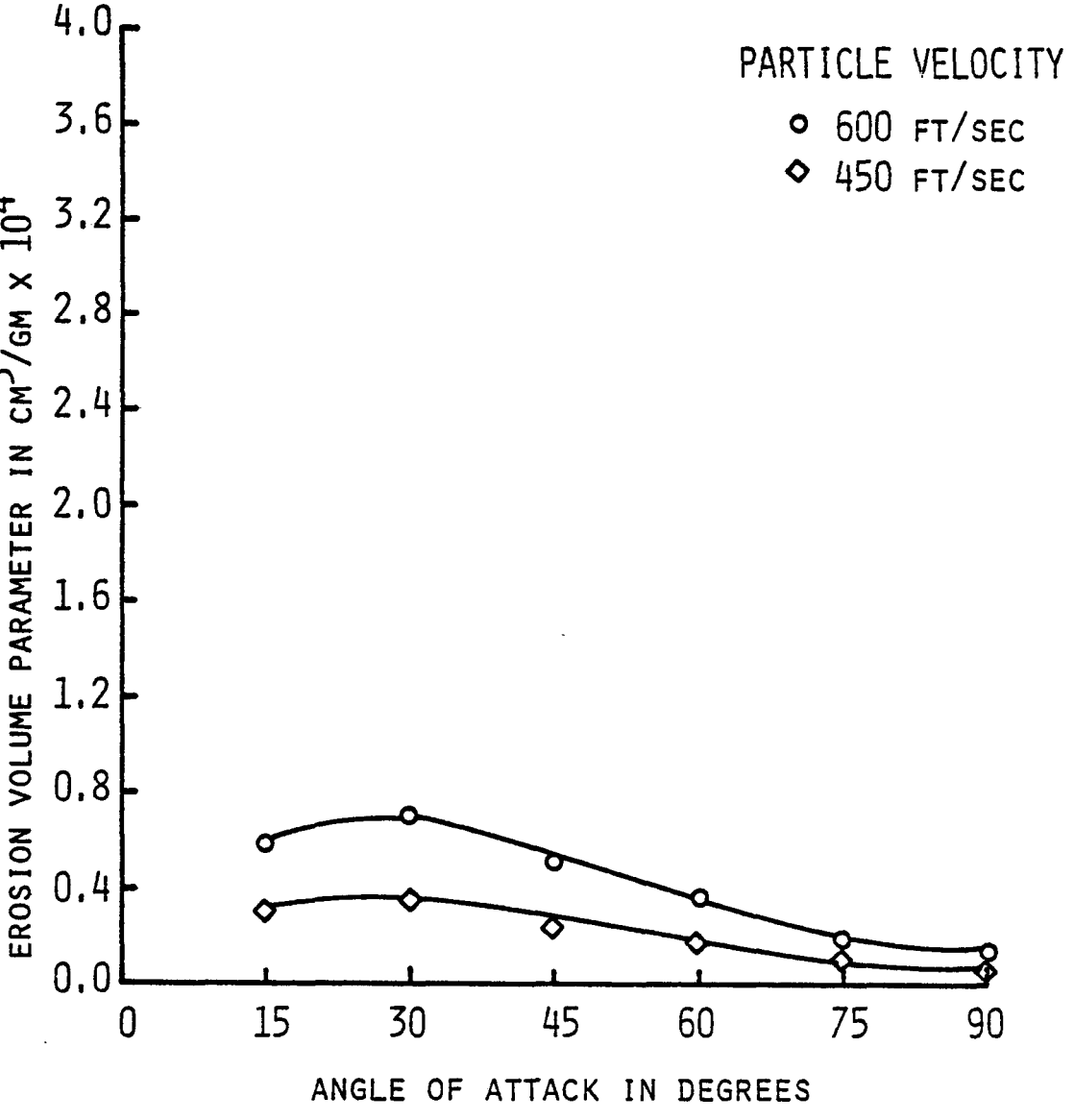

FIG. 29. EFFECT OF ANGLE OF ATTACK ON A286 AT ROOM TEMPERATURE.

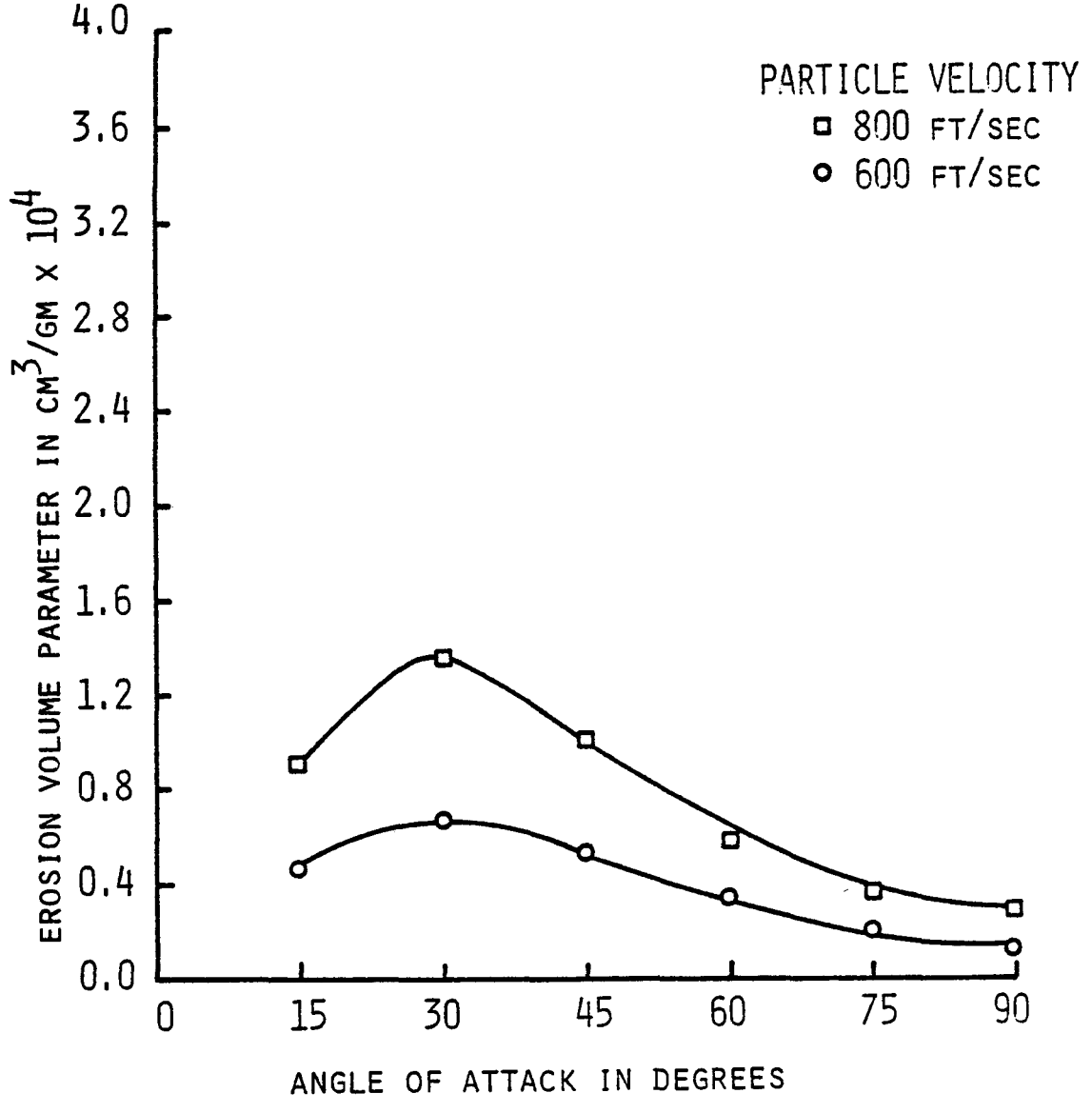

FIG. 30. EFFECT OF ANGLE OF ATTACK ON A286 AT 300°F.

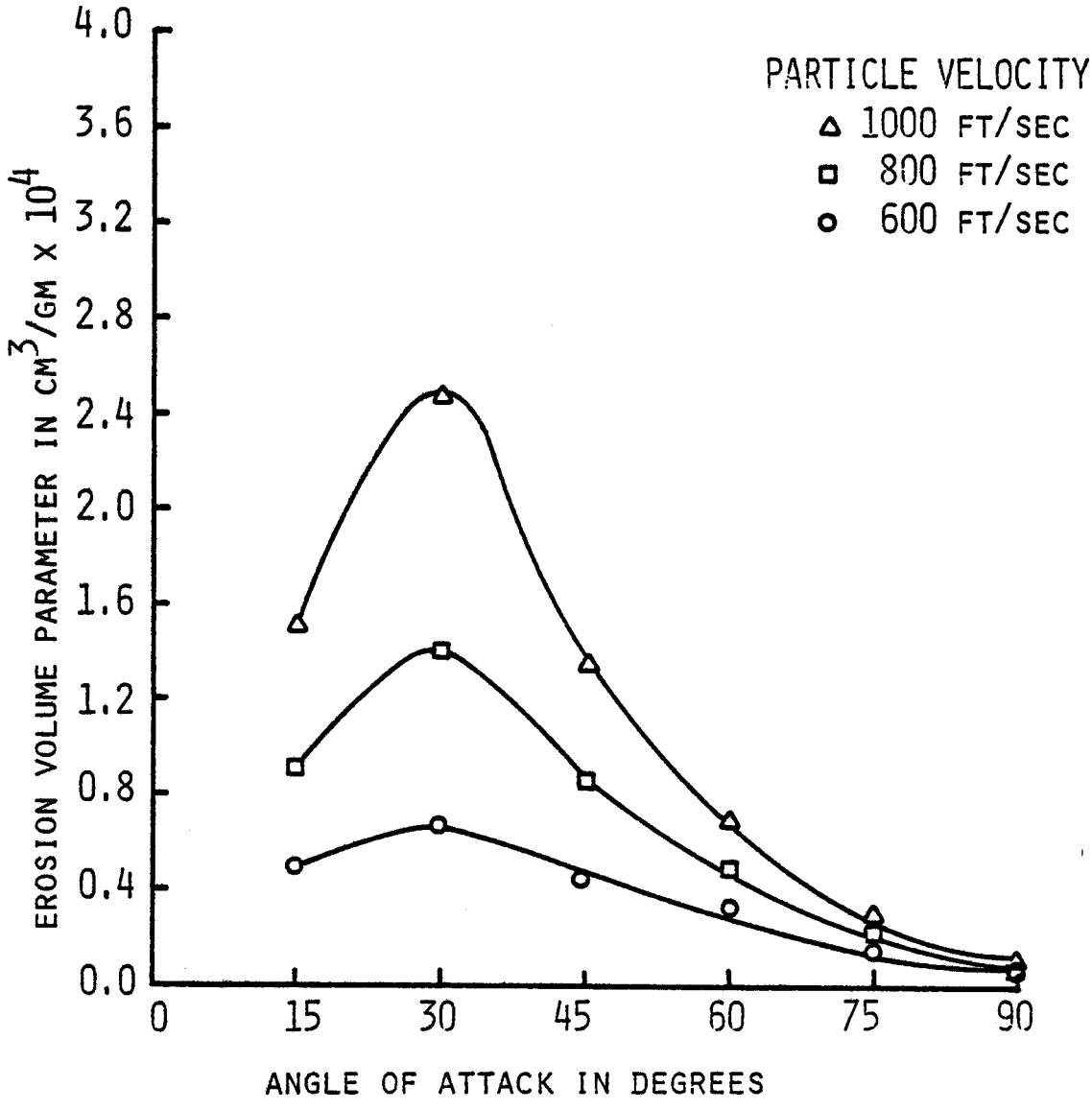

FIG. 31. EFFECT OF ANGLE OF ATTACK ON A286 AT 600°F

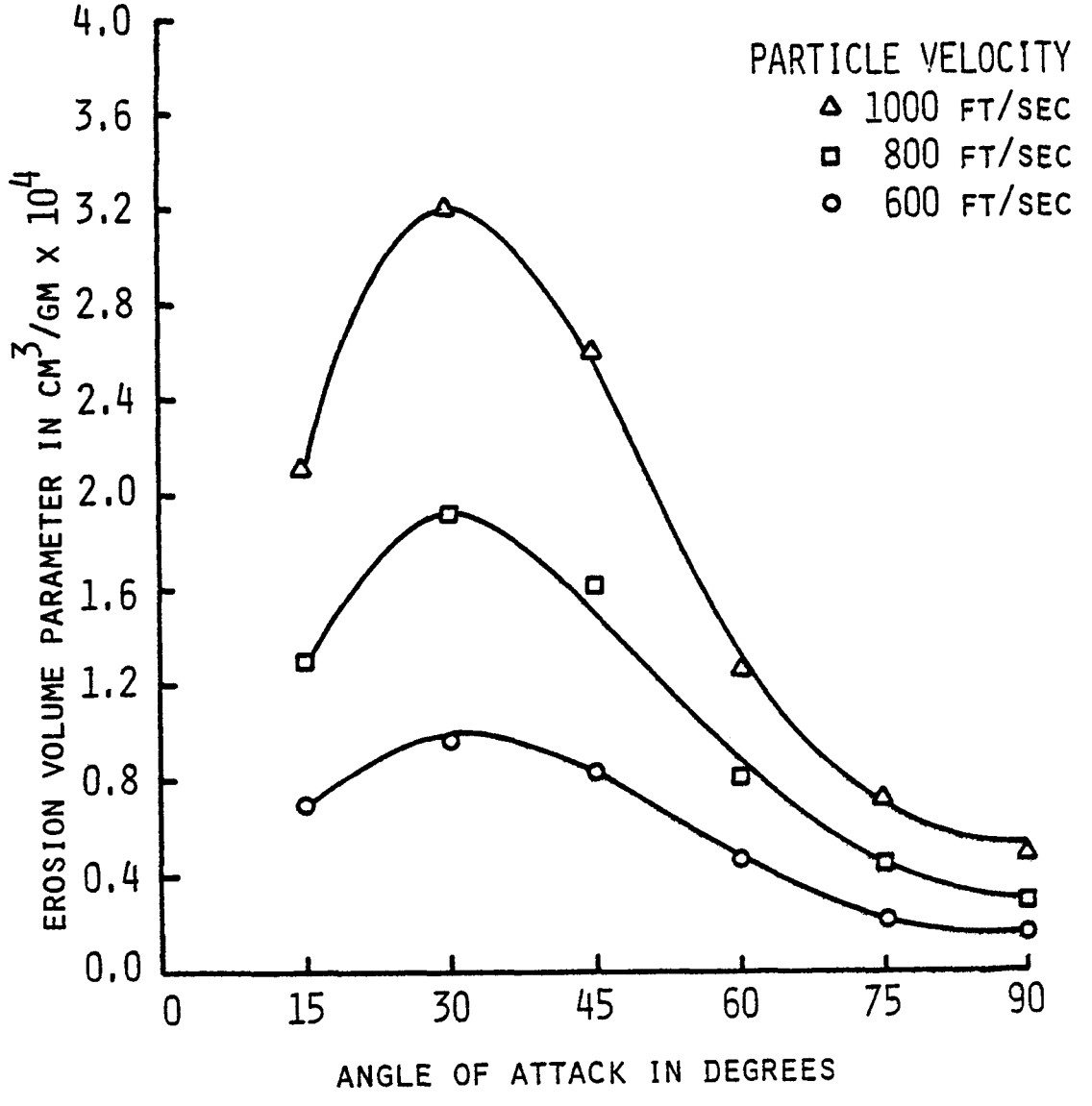

FIG. 32. EFFECT OF ANGLE OF ATTACK ON A286 AT 900°F.

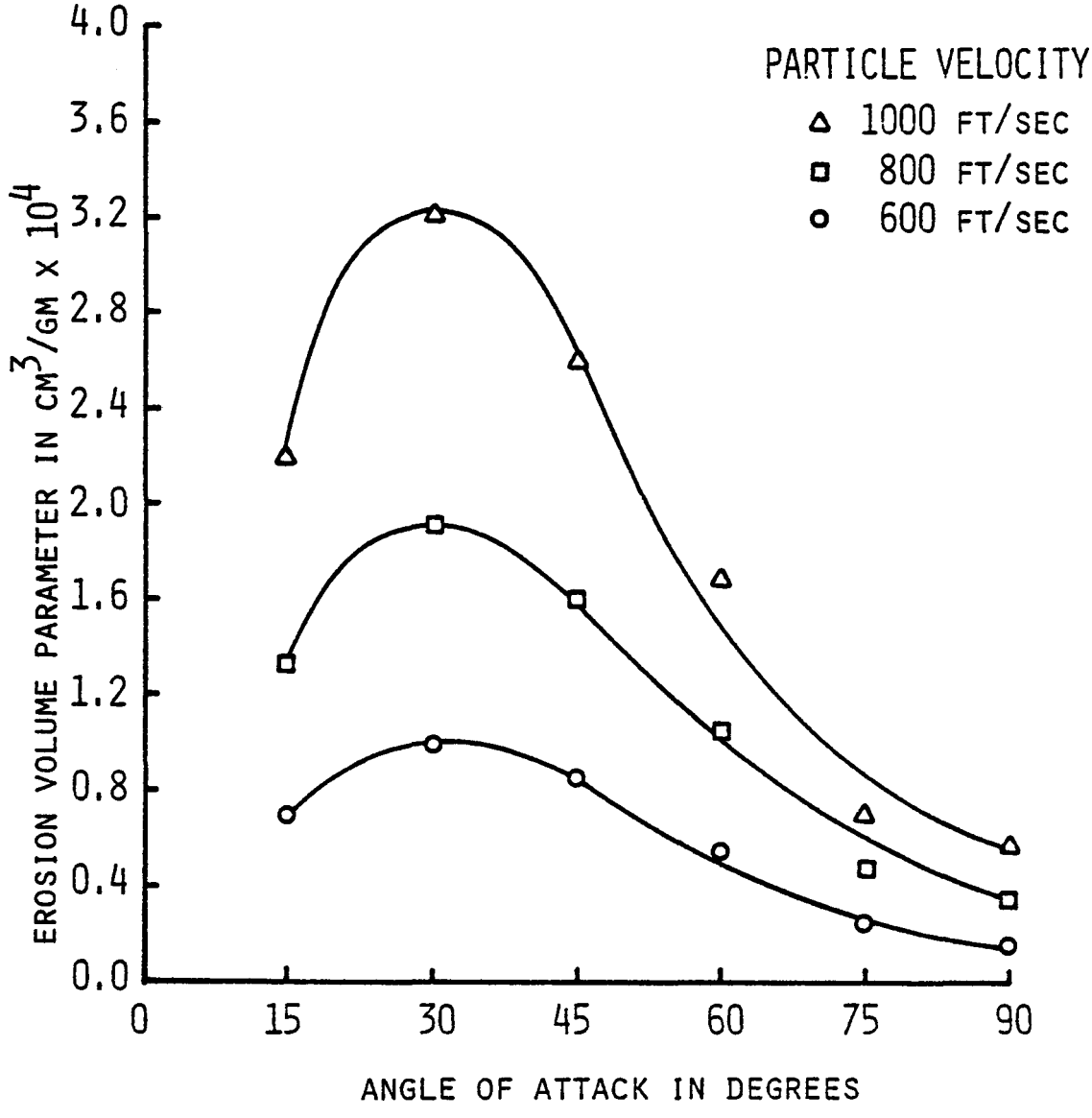

FIG. 33. EFFECT OF ANGLE OF ATTACK ON A286 AT 1200°F.

EROSION CHARACTERISTICS OF:

304 STEEL

RENE 41

A286

(WITH RESPECT TO TEMPERATURE)

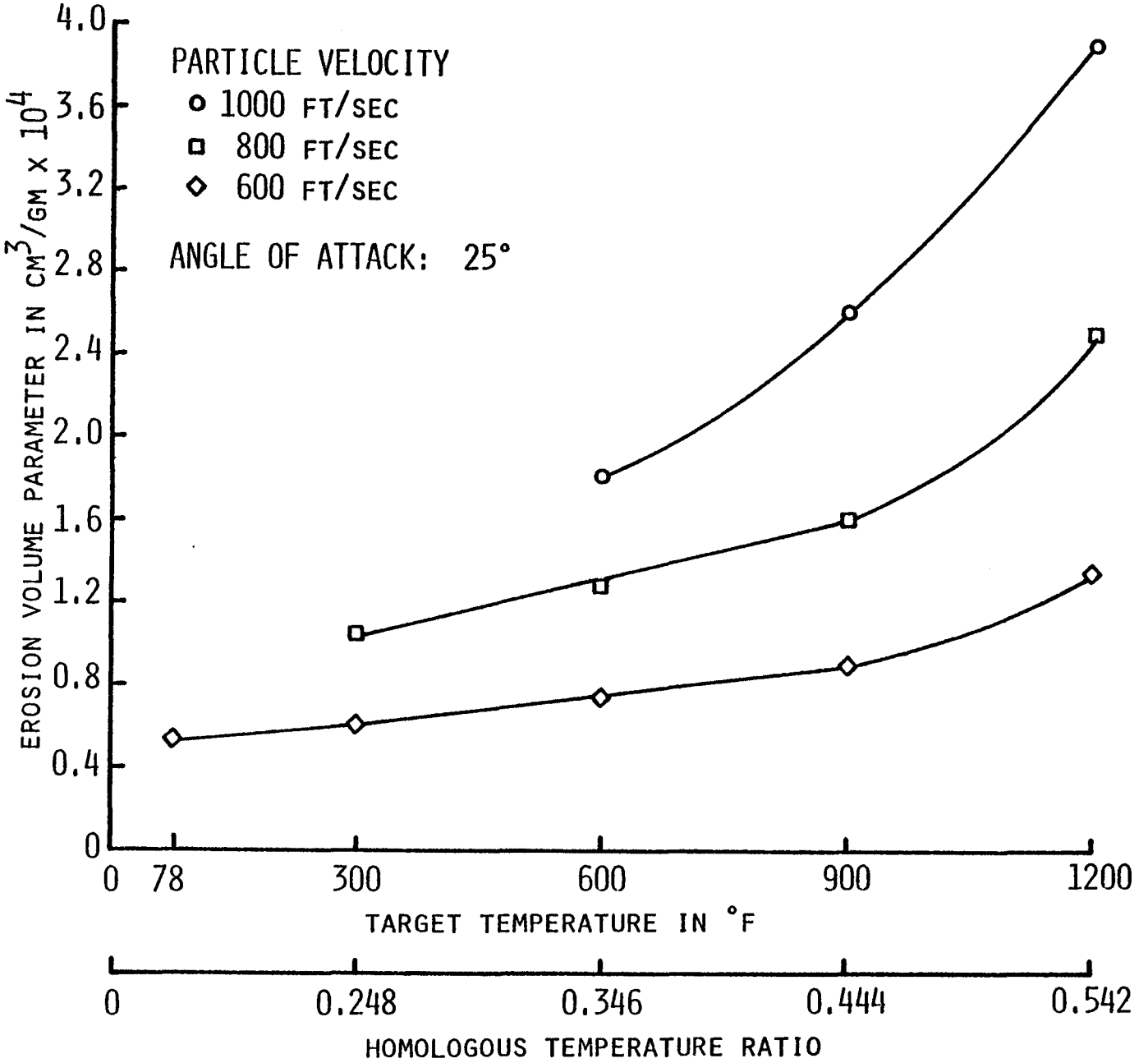

FIG. 34. EFFECT OF TEMPERATURE ON 304 STEEL.

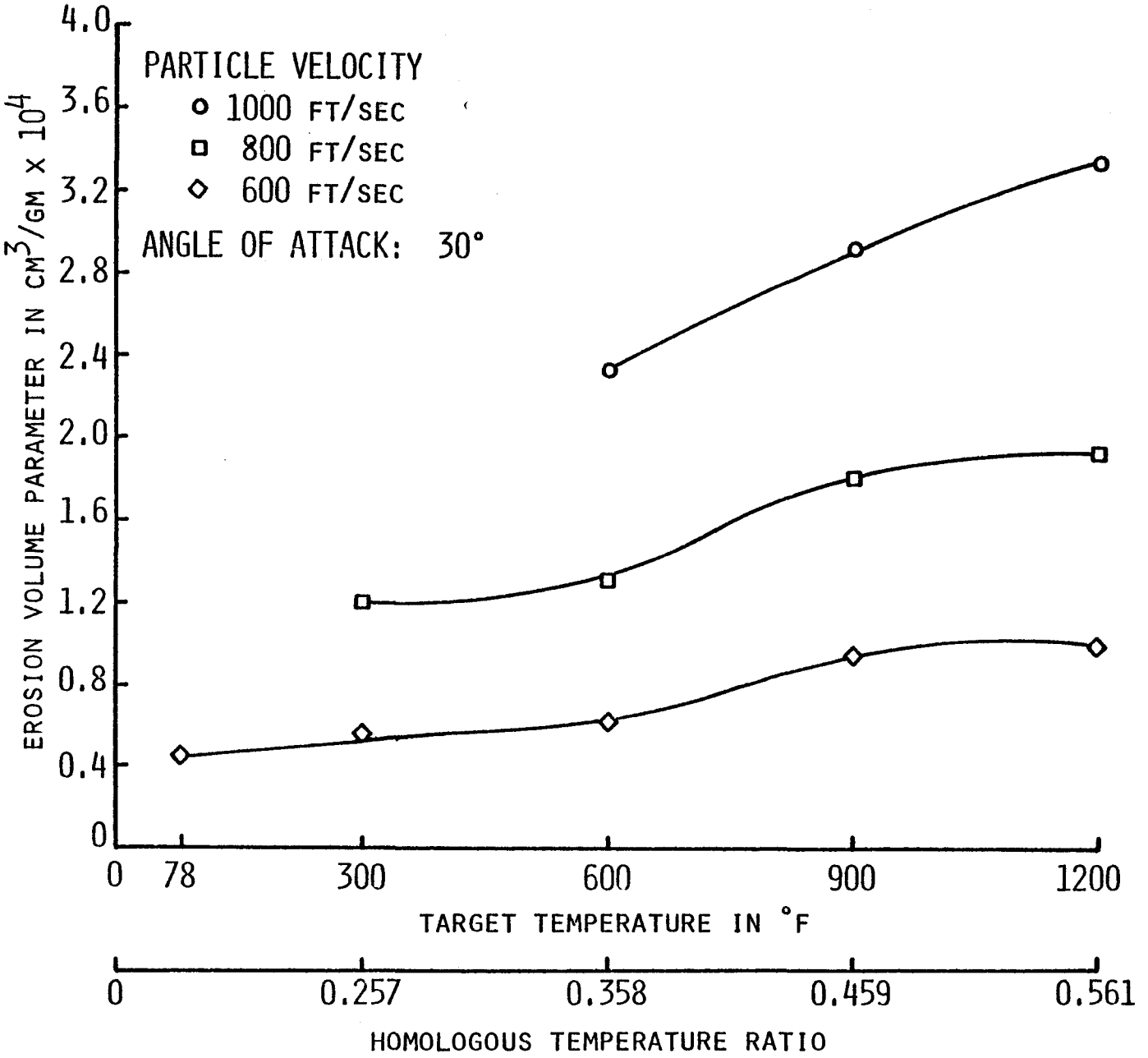

FIG. 35. EFFECT OF TEMPERATURE ON RENE 41.

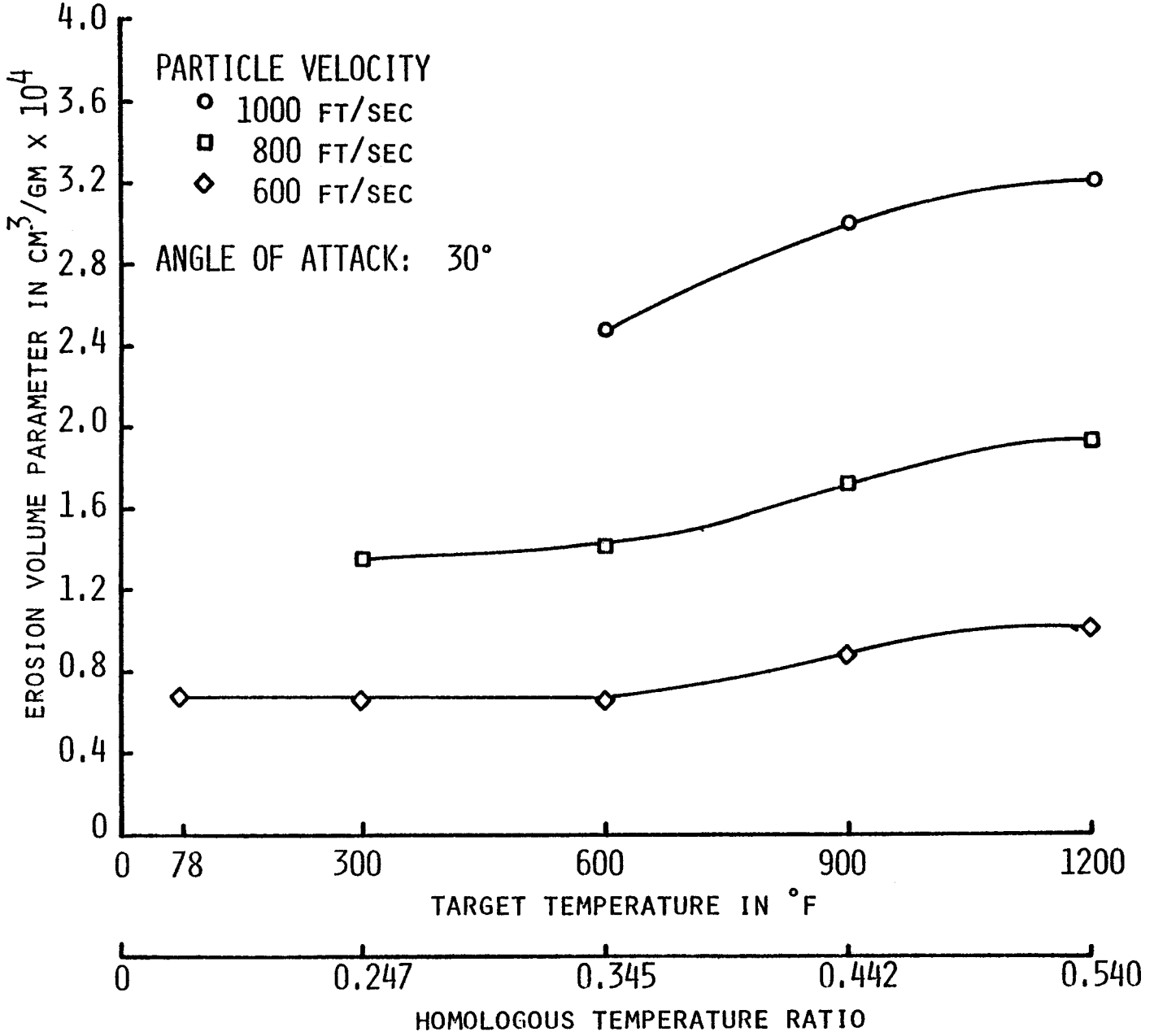

FIG. 36. EFFECT OF TEMPERATURE ON A286.

COMPARATIVE EROSION DAMAGE ON:

304 STEEL

RENE 41

A286

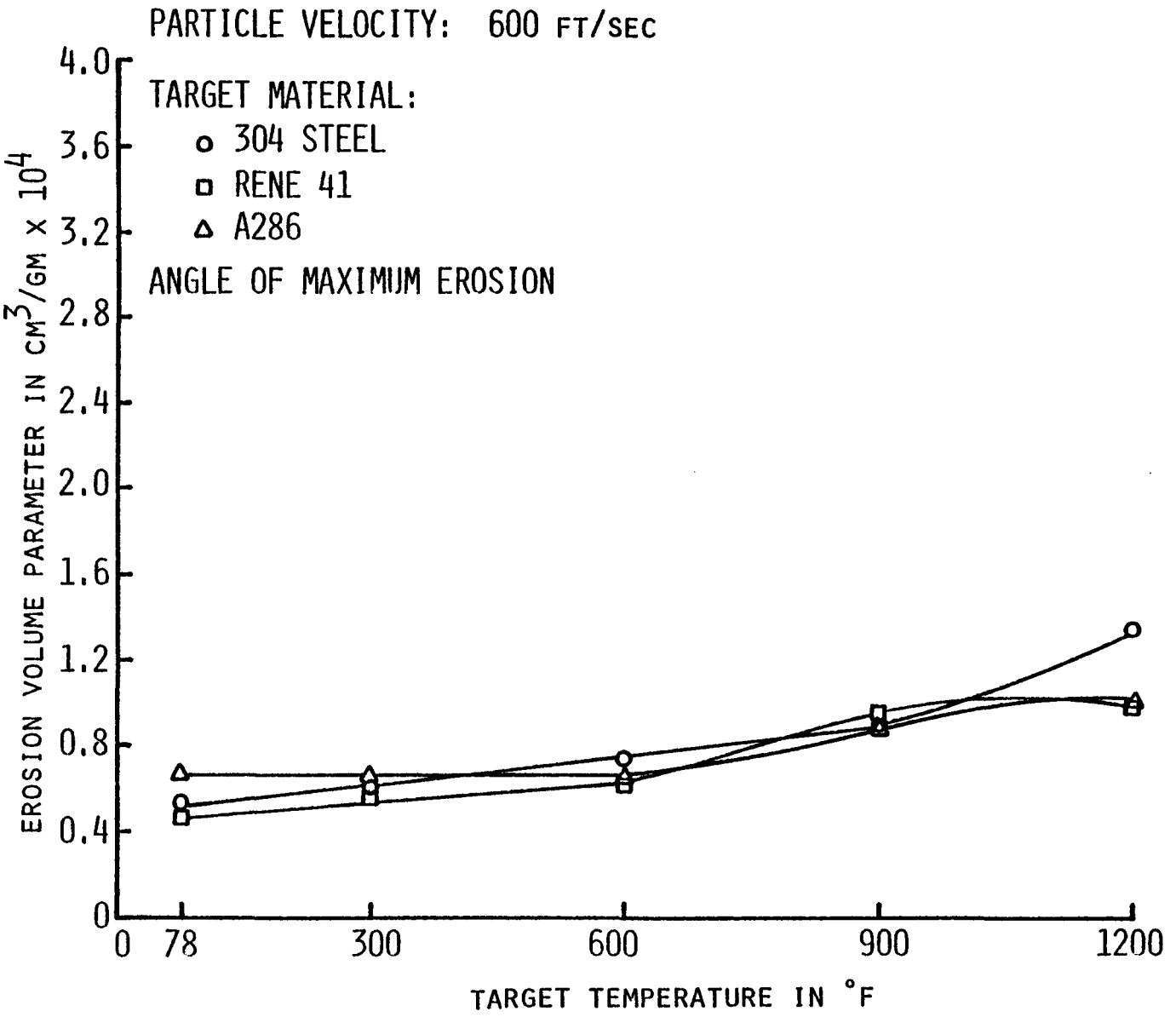

FIG. 37. COMPARATIVE EROSION DAMAGE AT PARTICLE VELOCITIES OF 600 FT/SEC.

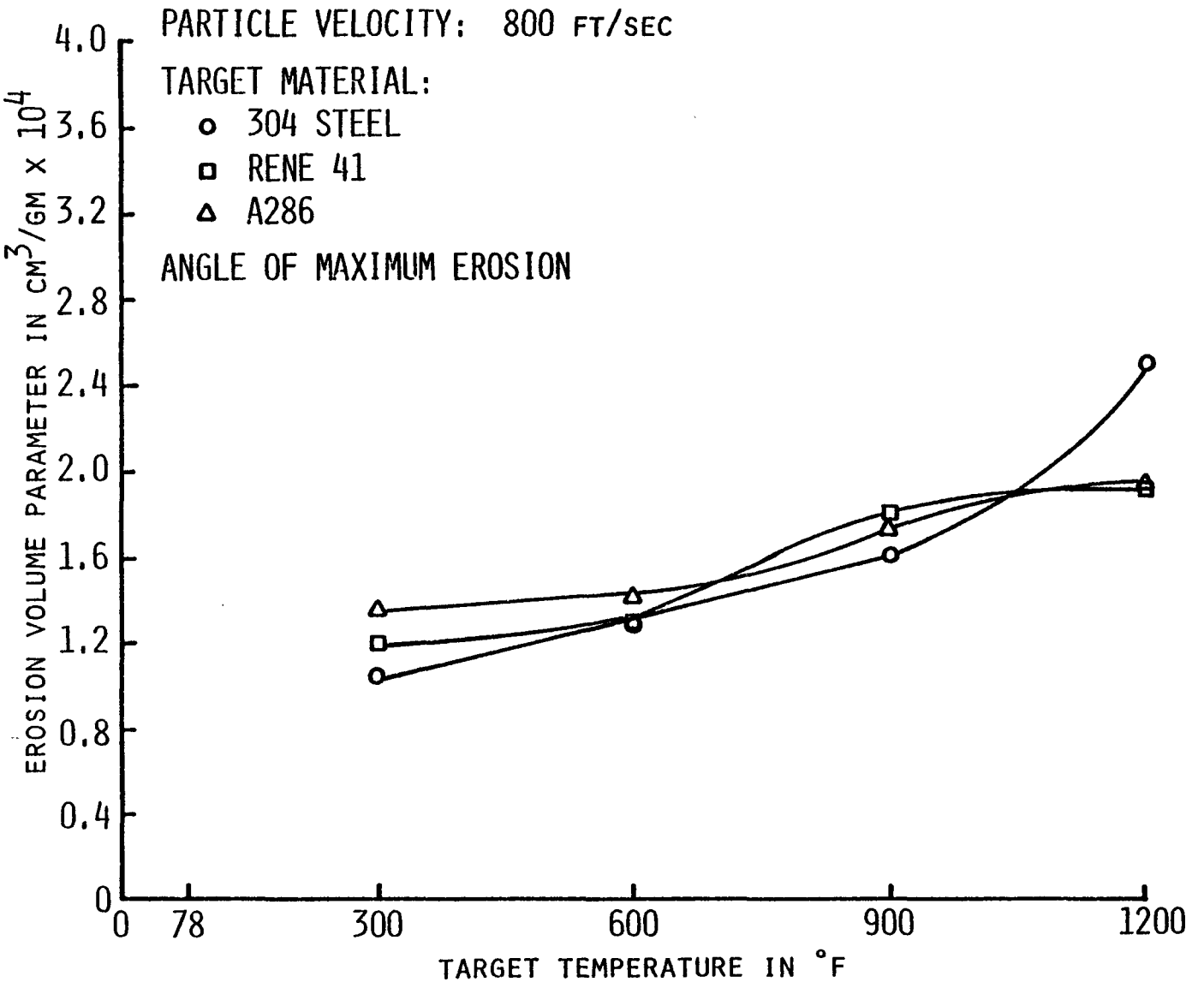

FIG. 38. COMPARATIVE EROSION DAMAGE AT PARTICLE VELOCITIES OF 800 FT/SEC.

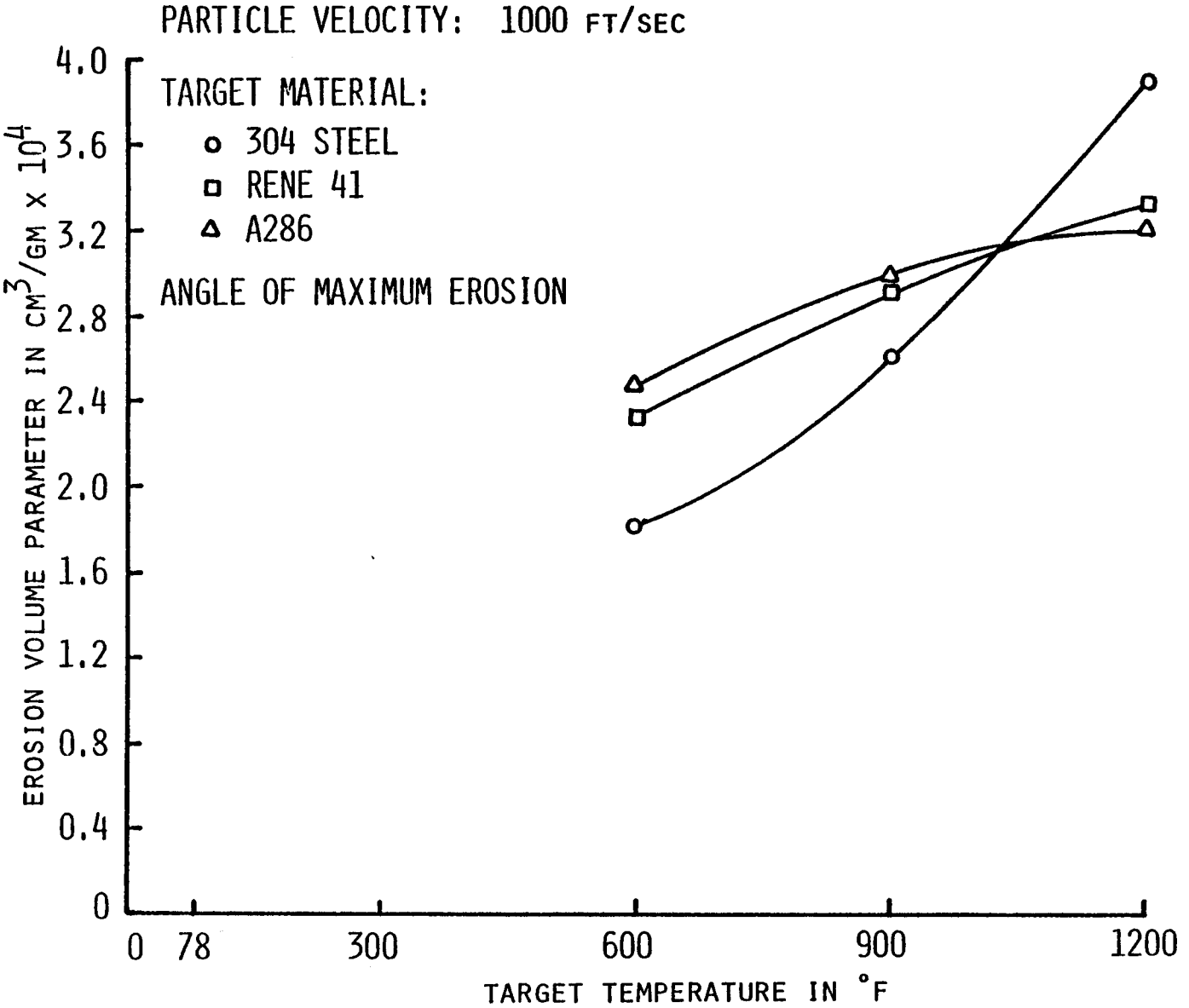

FIG. 39. COMPARATIVE EROSION DAMAGE AT PARTICLE VELOCITIES OF 1000 FT/SEC

TABLE VIII. CHEMICAL ANALYSIS OF FLY-ASH

Substance	Amount Present (%)		
	Kingston Fly-Ash	CG&E Fly-Ash	Exxon Fly-Ash (3rd Cyclone)
Si	54.39	48.08	15.40
Al	28.58	21.16	25.40
Fe	10.08	20.05	5.53
Ca	1.28	--	7.20
Ti	0.47	--	--
Mg	1.04	0.93	3.84
Na	0.20	0.64	0.59
K	2.09	--	1.16
S	1.03	1.20	0.05
P_2O_5	0.06	--	--
SO_4	--	--	22.4
Cl	--	--	0.14
PO_4	--	--	0.25
C	--	--	1.2
F	--	--	0.02
Undetermined	0.78	7.94	16.82
Total	100.00	100.00	100.00

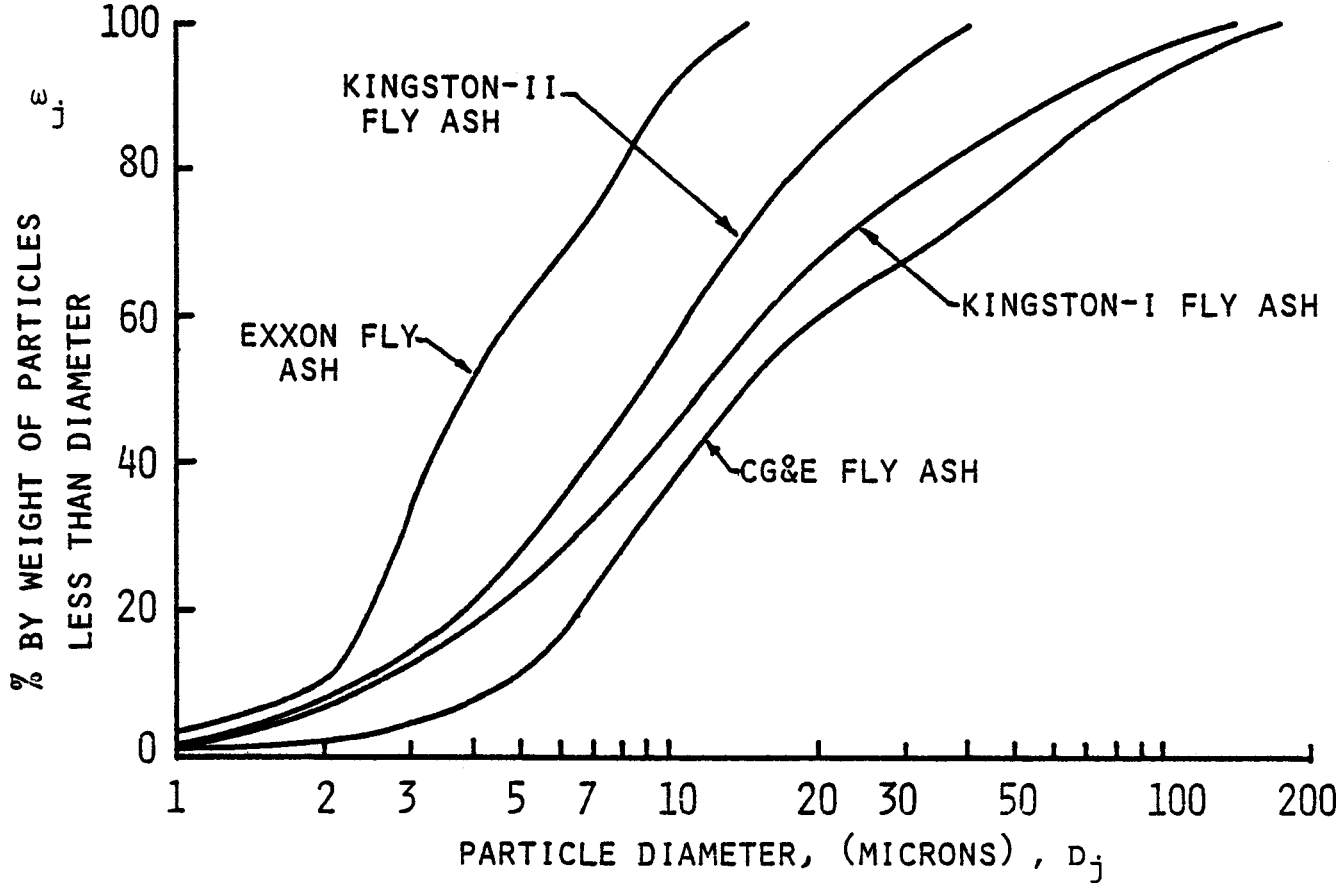

FIG. 40. FLY ASH PARTICLE SIZE DISTRIBUTIONS.

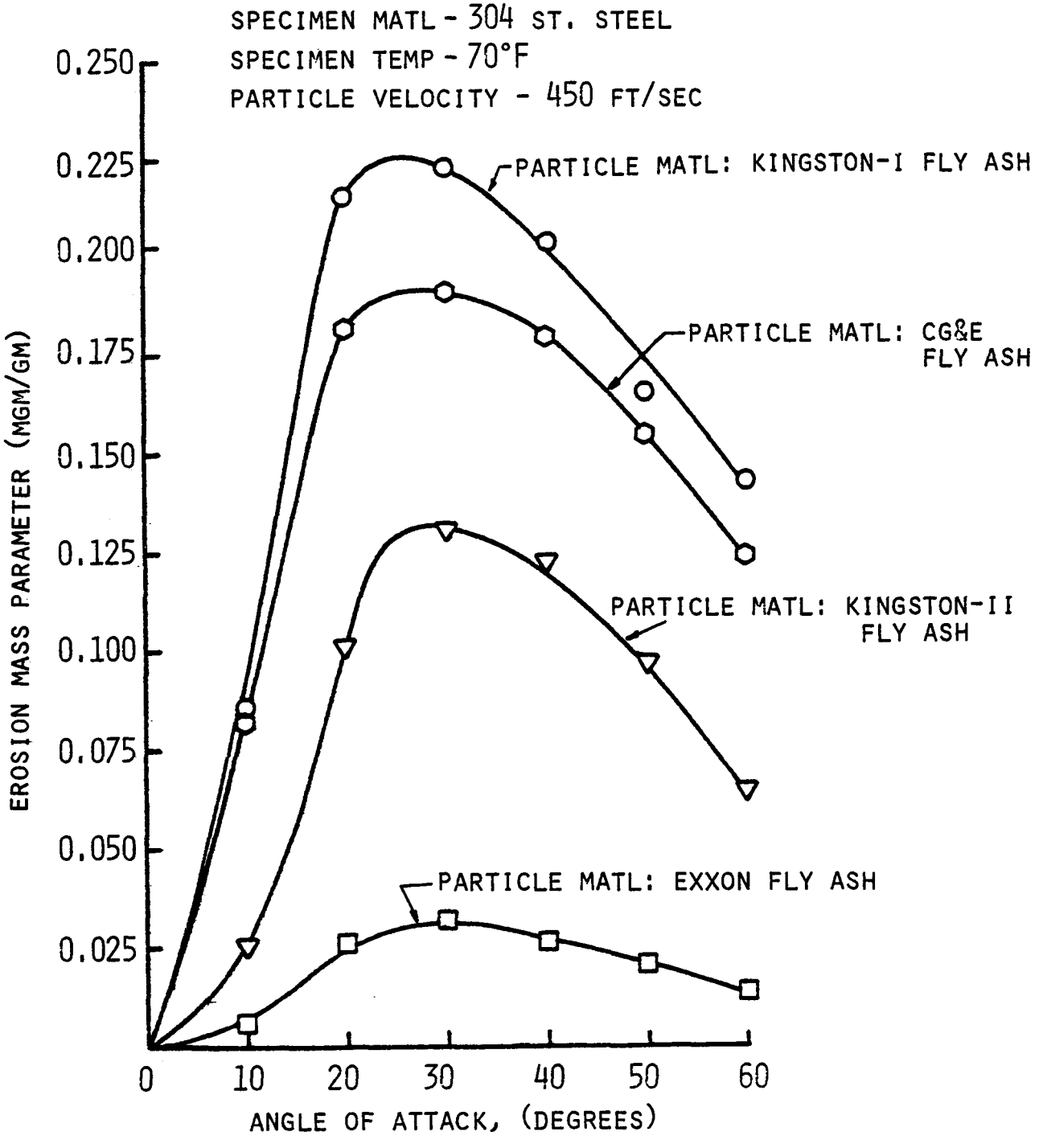

FIG. 41. EROSION CAUSED BY VARIOUS TYPES OF FLY ASH PARTICLES (EXPERIMENTAL RESULTS).

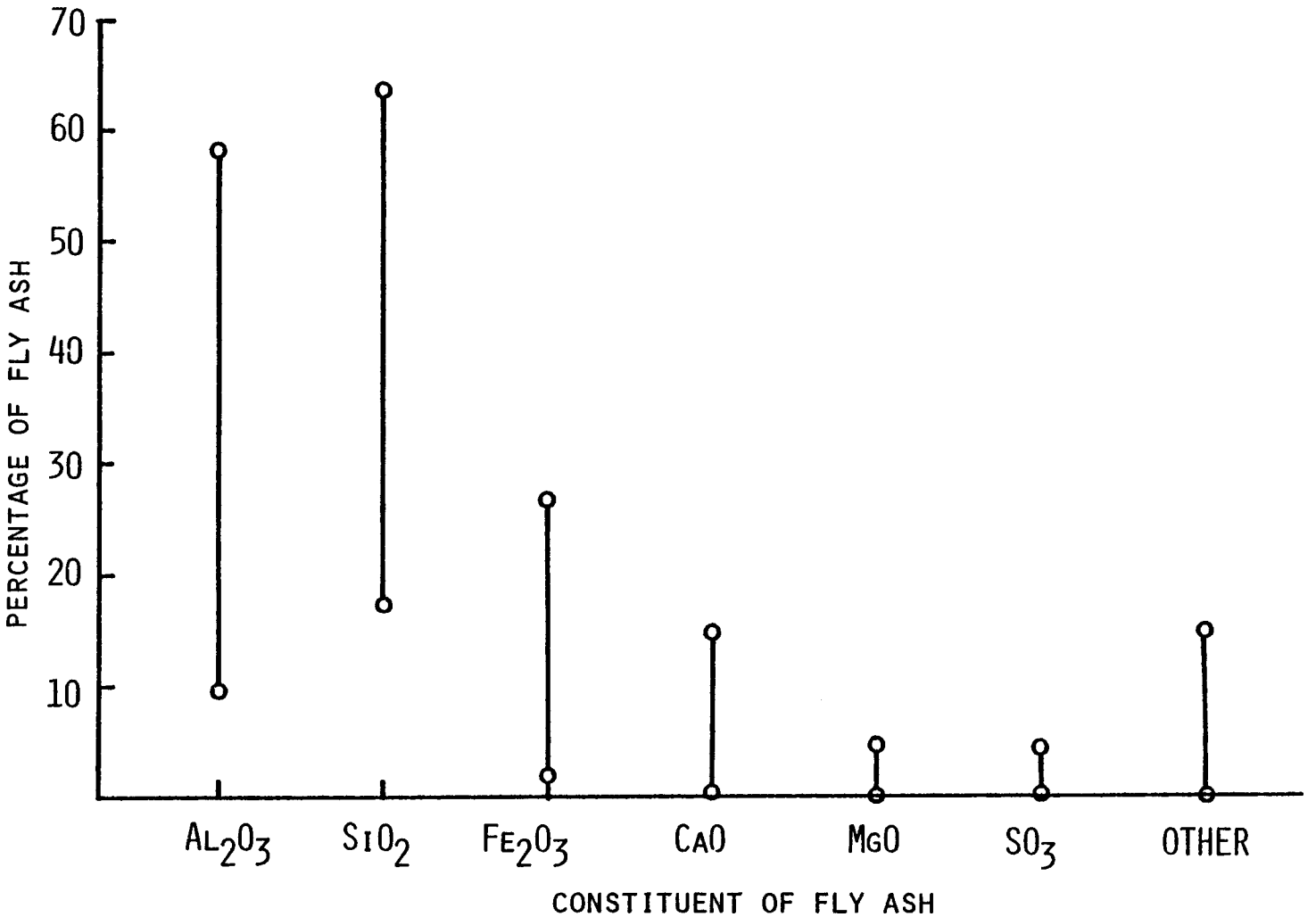

FIG. 42. RANGES IN ANALYSIS OF FLY ASH (REF. 14).

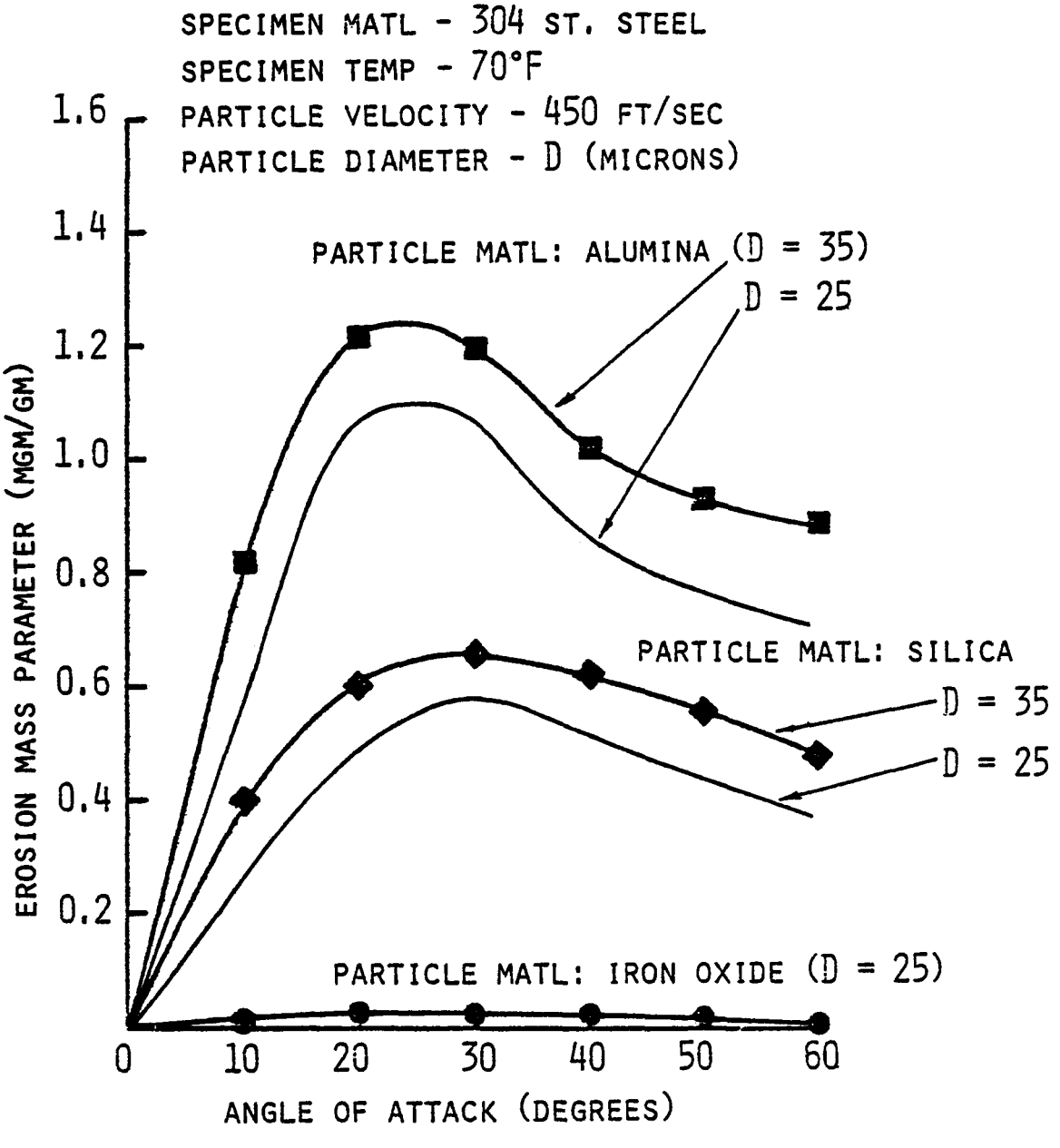

FIG. 43. EROSION VS. ANGLE OF ATTACK FOR DIFFERENT COMMERCIAL ABRASIVES (EXPERIMENTAL RESULTS).

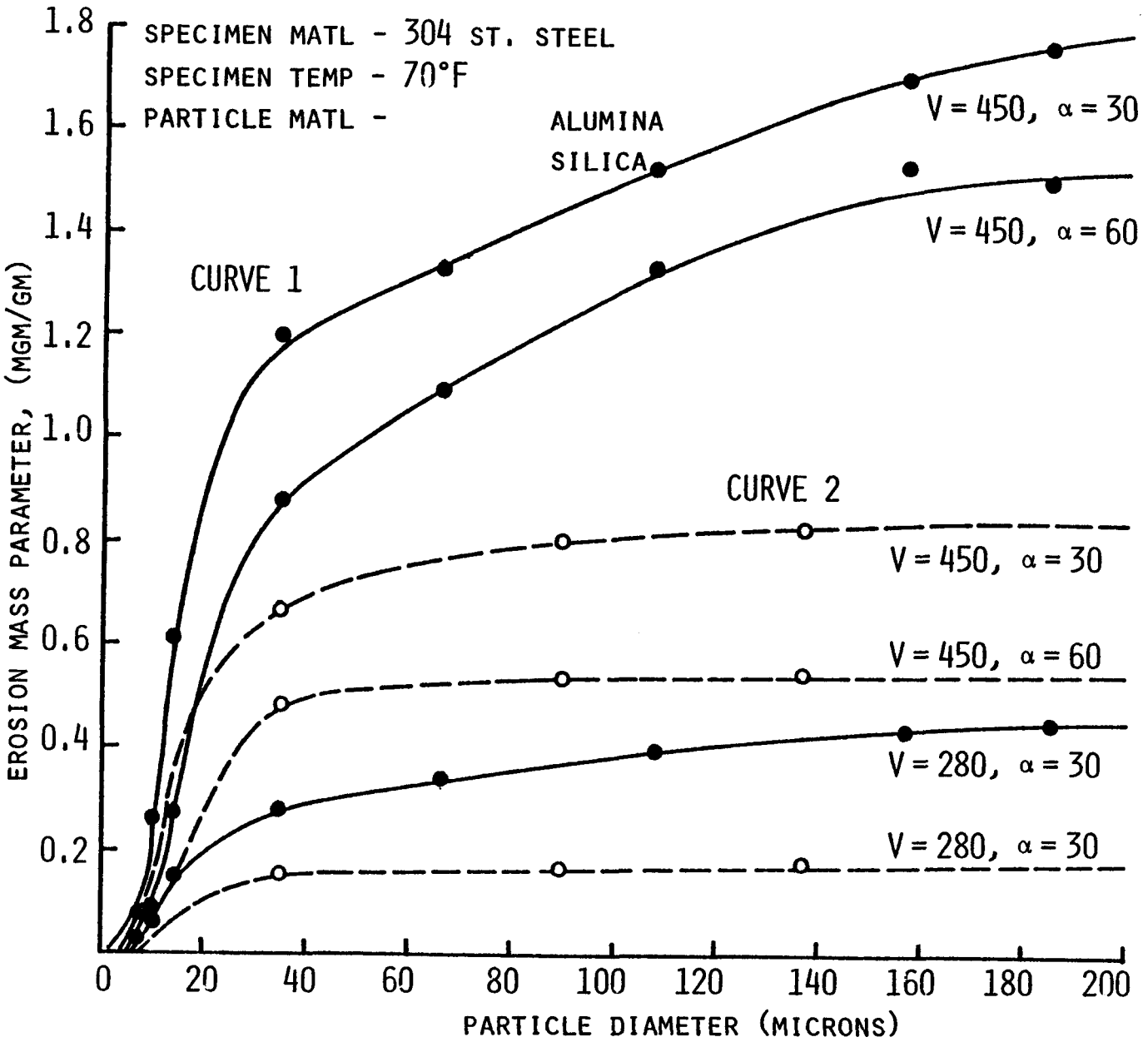

FIG. 44. EROSION VS. PARTICLE SIZE AT ROOM TEMPERATURE (EXPERIMENTAL RESULTS).

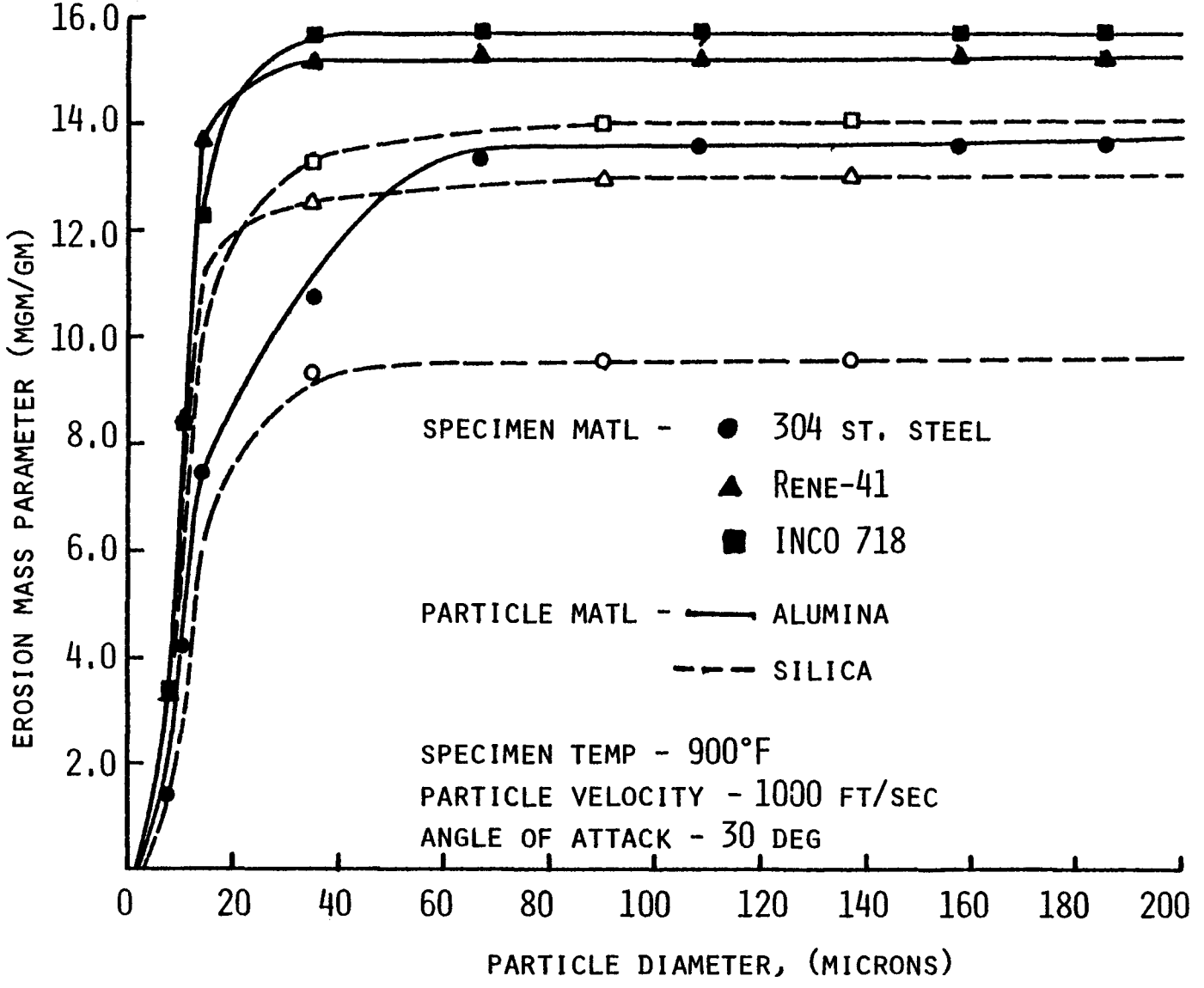

FIG. 45. EROSION VS. PARTICLE SIZE AT 900°F (EXPERIMENTAL RESULTS).

TABLE IX. VALUE OF EROSION CONSTANT IN EQUATION (4)

TARGET MATERIAL	TARGET TEMPERATURE (°F)	PARTICLE VELOCITY (ft/sec)	ANGLE OF ATTACK (degree)	EROSION CONSTANT ψ
304 St. Steel	70	200-500	0-90	0.65
304 St. Steel	900	500-1000	30	0.425
Rene 41	900	500-1000	30	0.480
INCO 718	900	500-1000	30	0.525

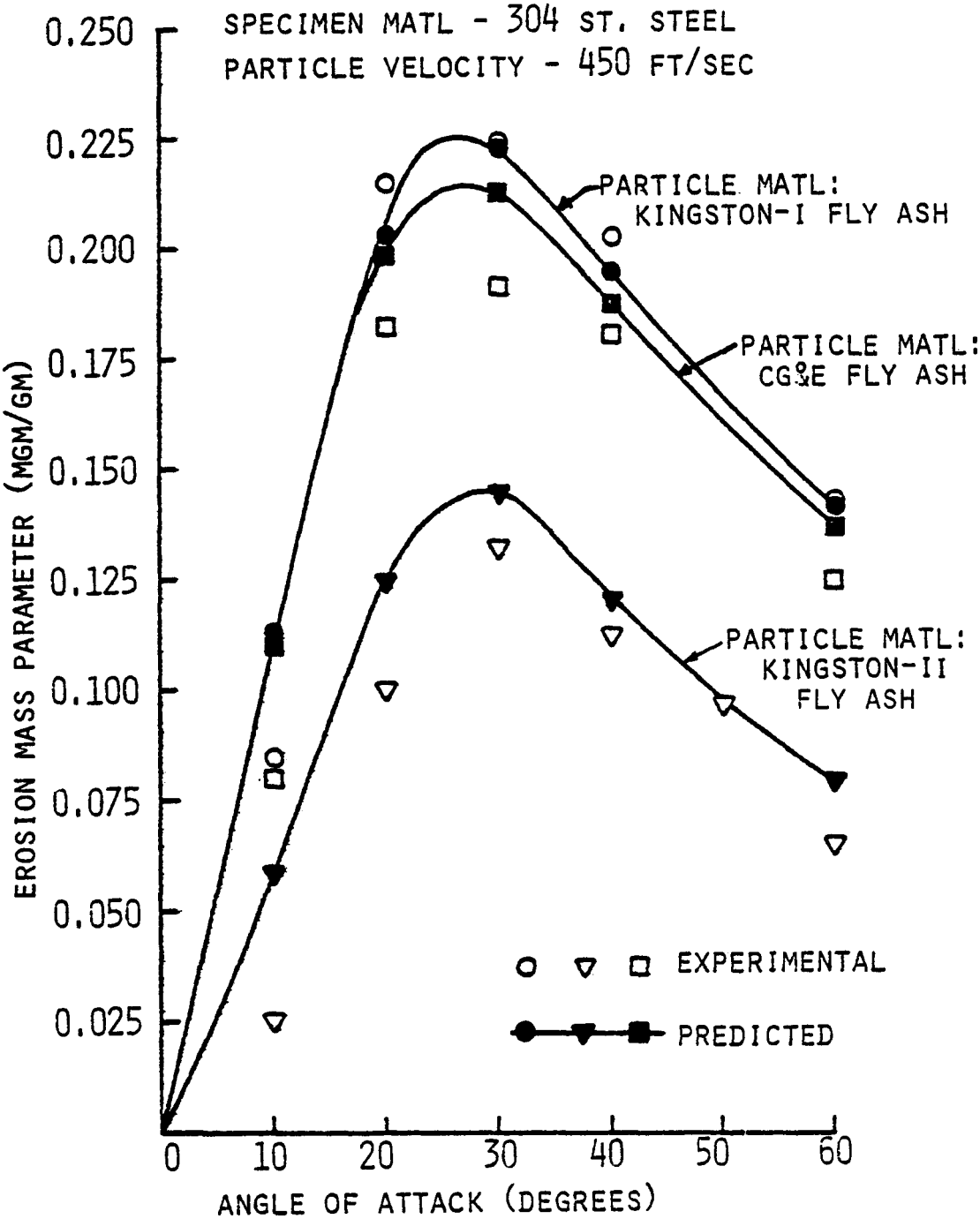

FIG. 46. EROSION VS. ANGLE OF ATTACK (EXPERIMENTAL AND PREDICTED RESULTS).

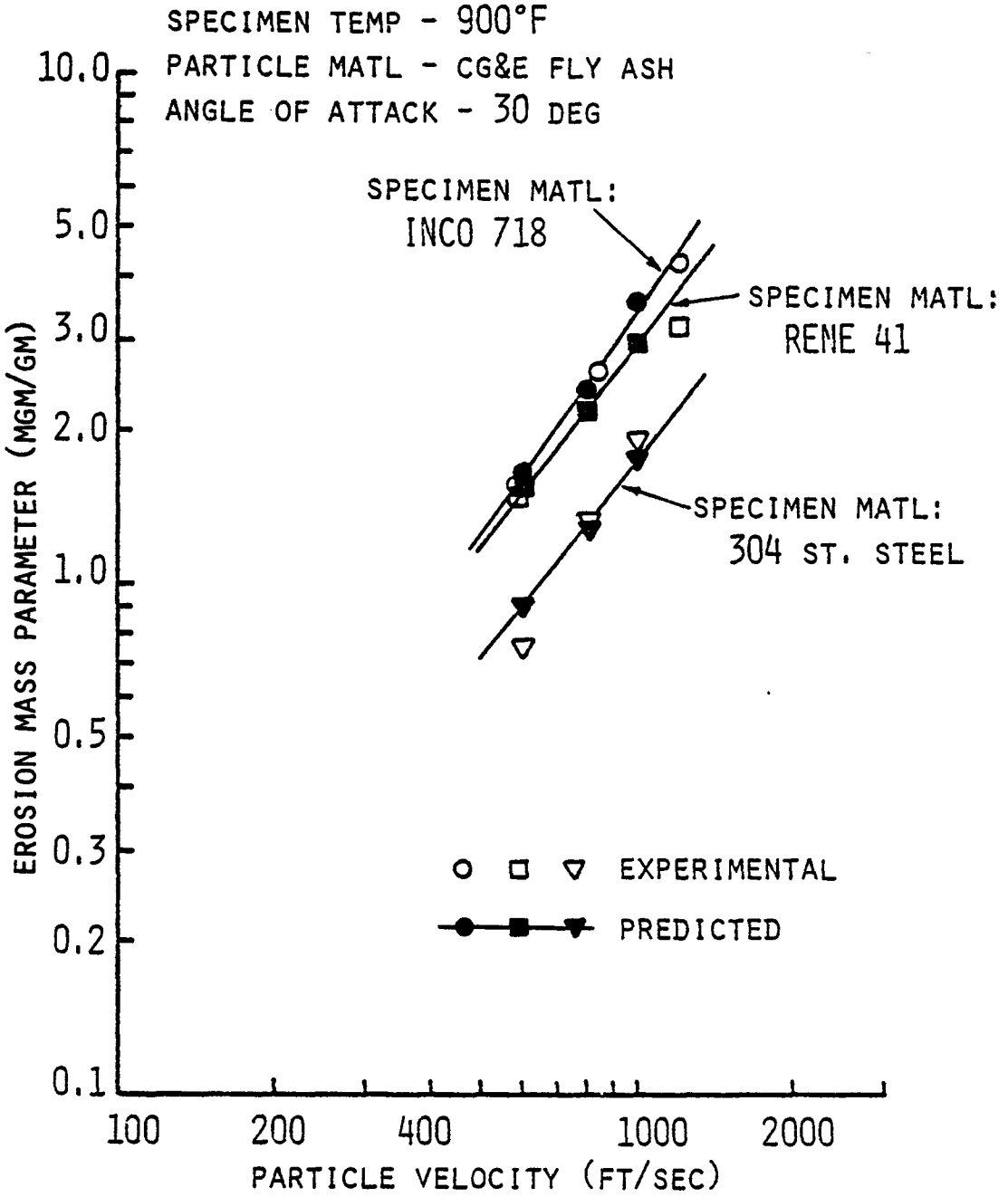

FIG. 47. EROSION VS. PARTICLE VELOCITY (EXPERIMENTAL AND PREDICTED RESULTS).

TABLE X. ASSUMED FLY ASH COMPOSITIONS.

Composition Name	Fly Ash Composition			
	Si Compound	Al Compound	Fe Compound	Other
A	60.00	30.00	5.00	5.00
B	60.00	25.00	10.00	5.00
C	60.00	20.00	15.00	5.00
D	55.00	30.00	10.00	5.00
E	55.00	25.00	15.00	5.00
F	55.00	20.00	20.00	5.00
G	50.00	30.00	15.00	5.00
H	50.00	25.00	20.00	5.00
I	50.00	20.00	25.00	5.00
J	45.00	30.00	20.00	5.00
K	45.00	25.00	25.00	5.00
L	40.00	30.00	25.00	5.00

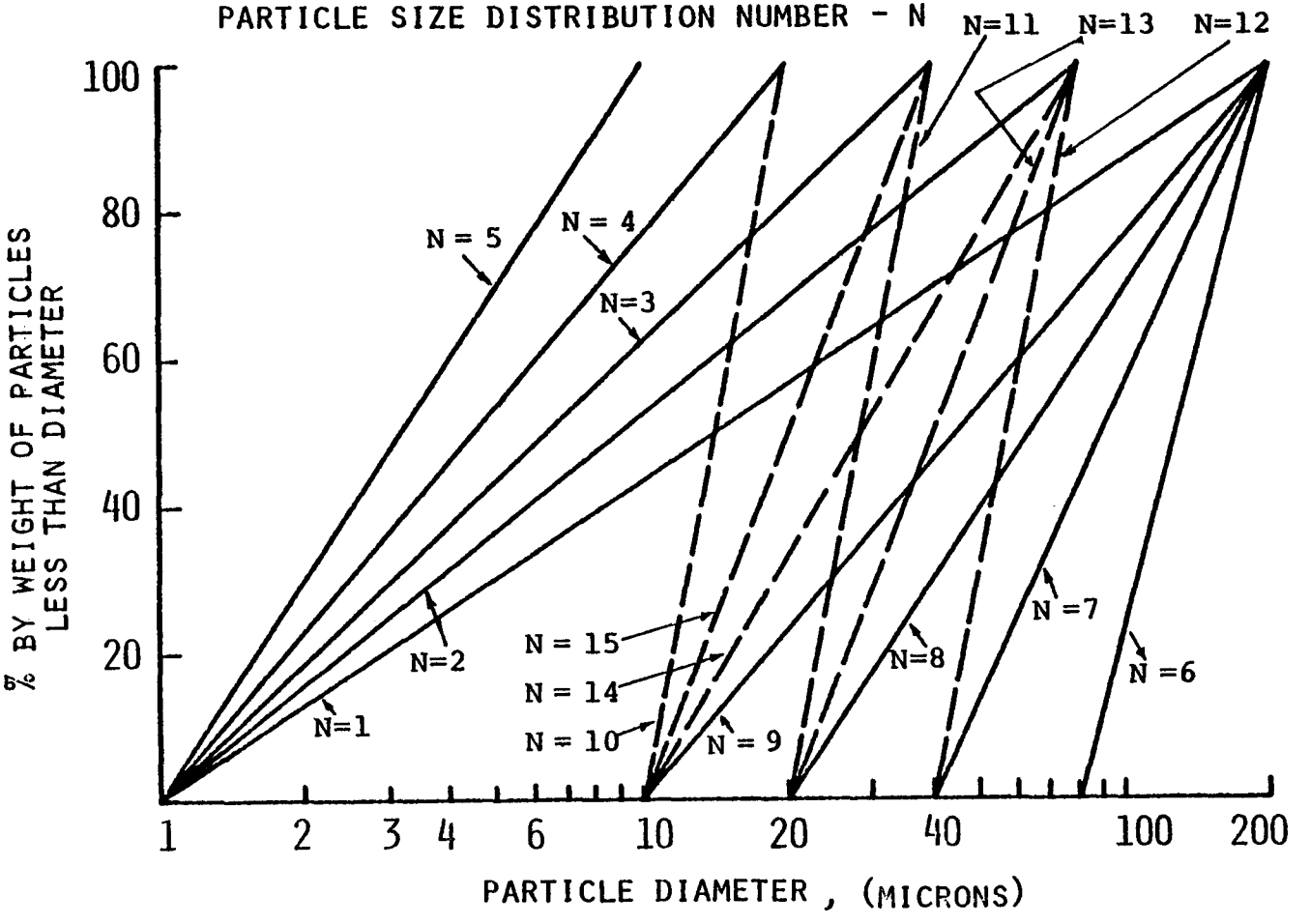

FIG.48. ASSUMED PARTICLE SIZE DISTRIBUTIONS.

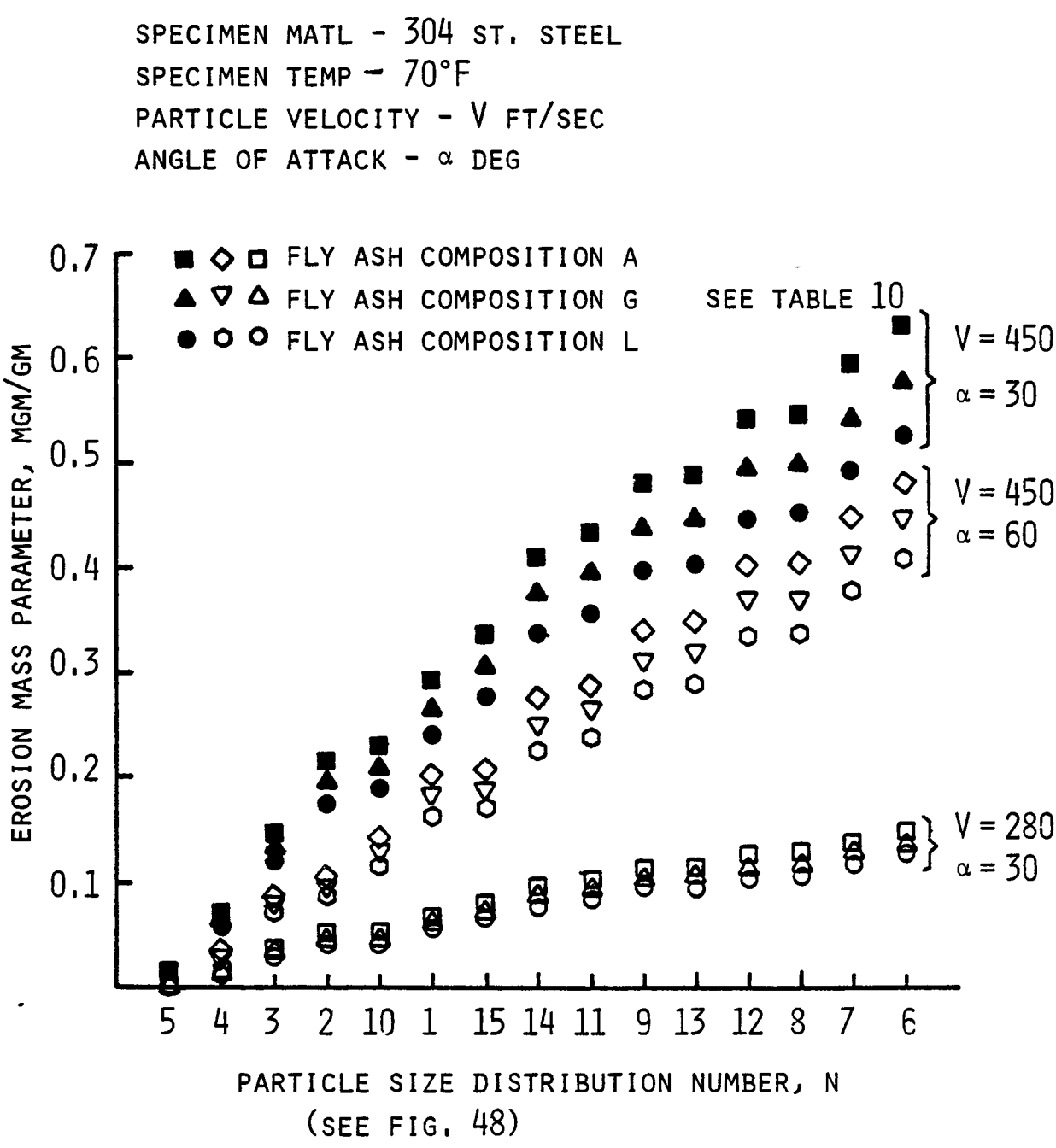

FIG. 49. RELATIVE EROSION LOSS CAUSED BY DIFFERENT TYPES OF FLY ASH ON 304 ST. STEEL SPECIMENS (PREDICTED RESULTS).

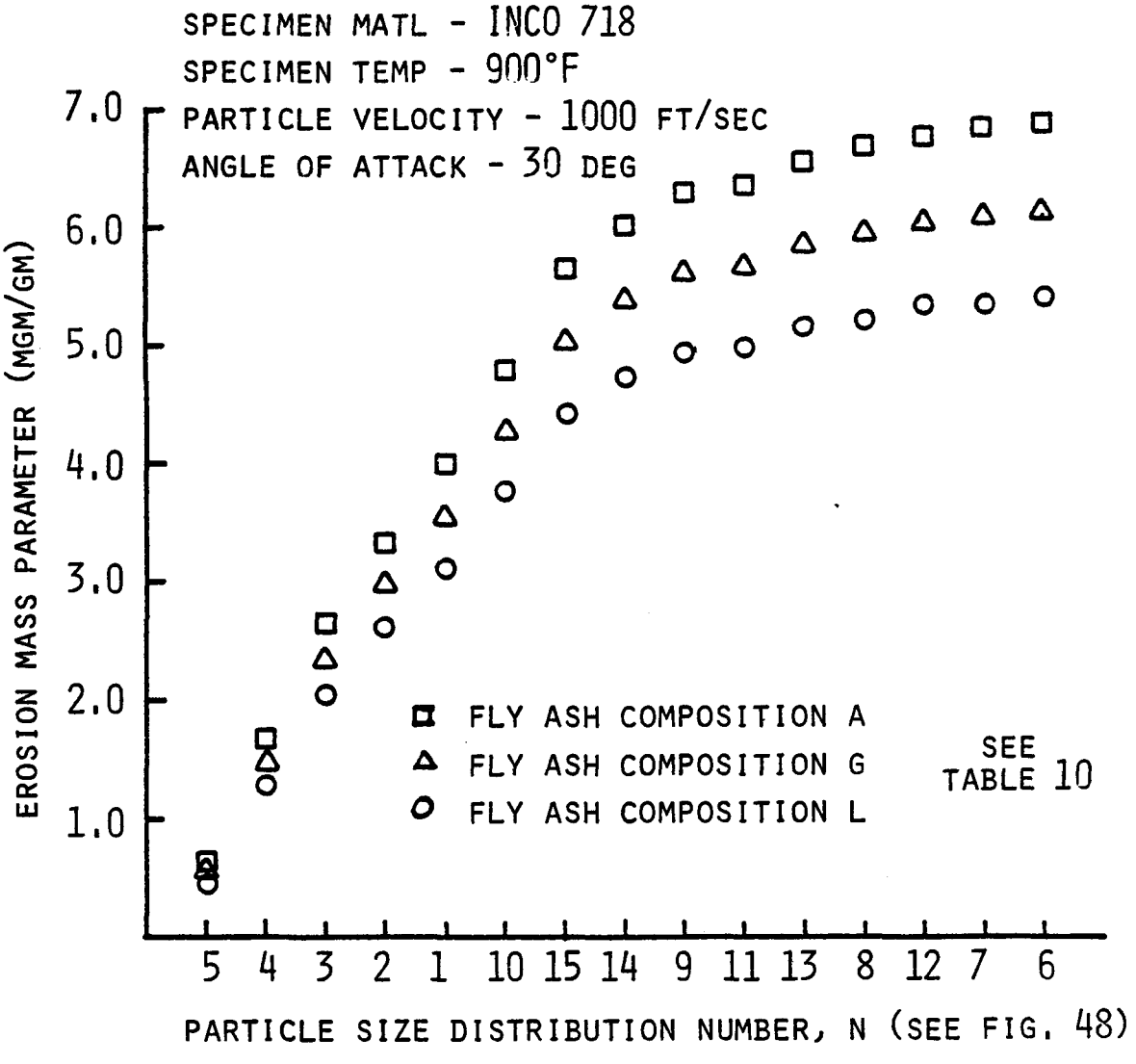

FIG. 50. RELATIVE EROSION LOSS CAUSED BY DIFFERENT TYPES OF FLY ASH PARTICLES ON INCO-718 SPECIMENS. (PREDICTED RESULTS).

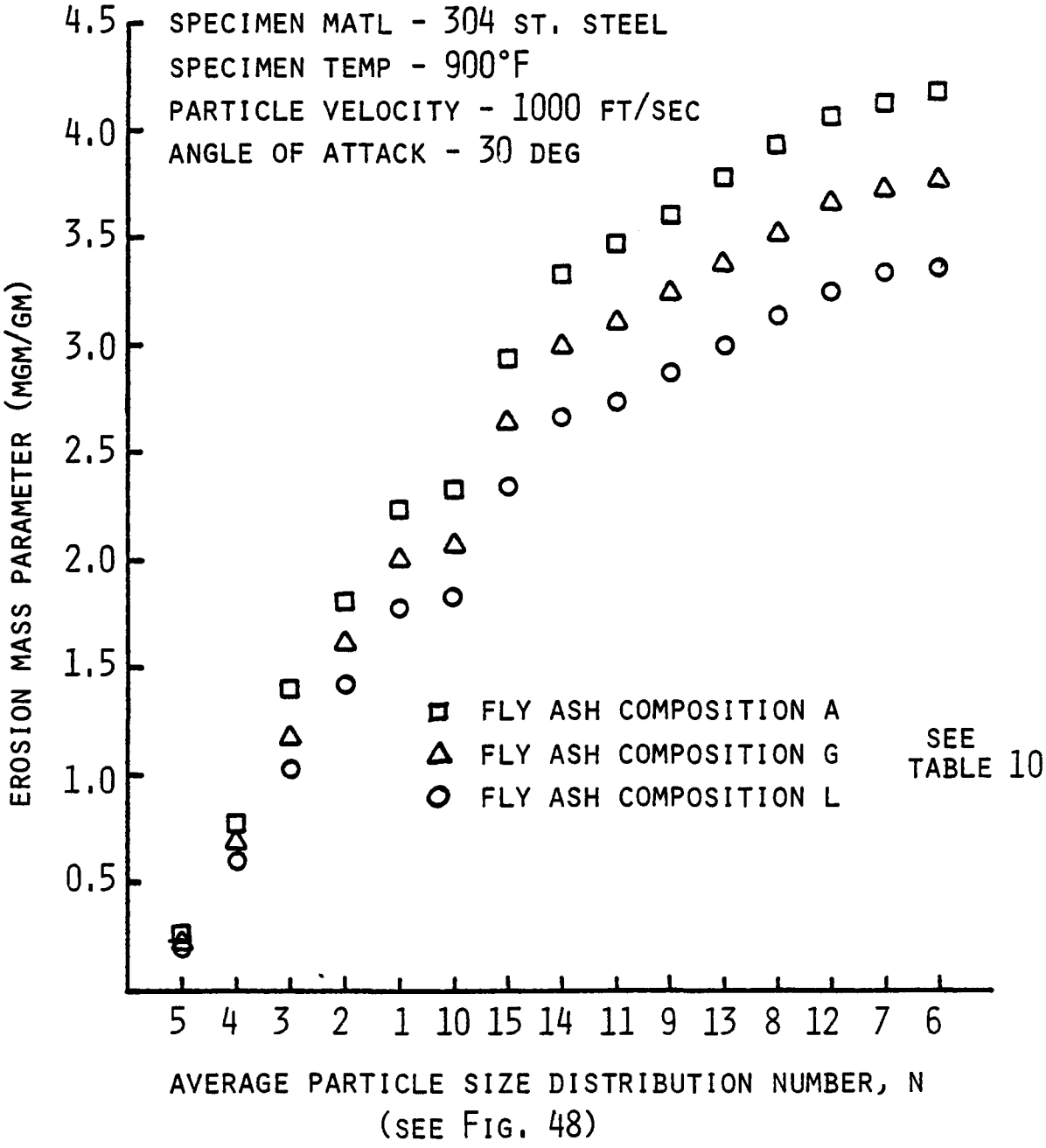

FIG. 51. RELATIVE EROSION LOSS CAUSED BY DIFFERENT TYPES OF FLY ASH PARTICLES ON 304 ST. STEEL SPECIMENS. (PREDICTED RESULTS)

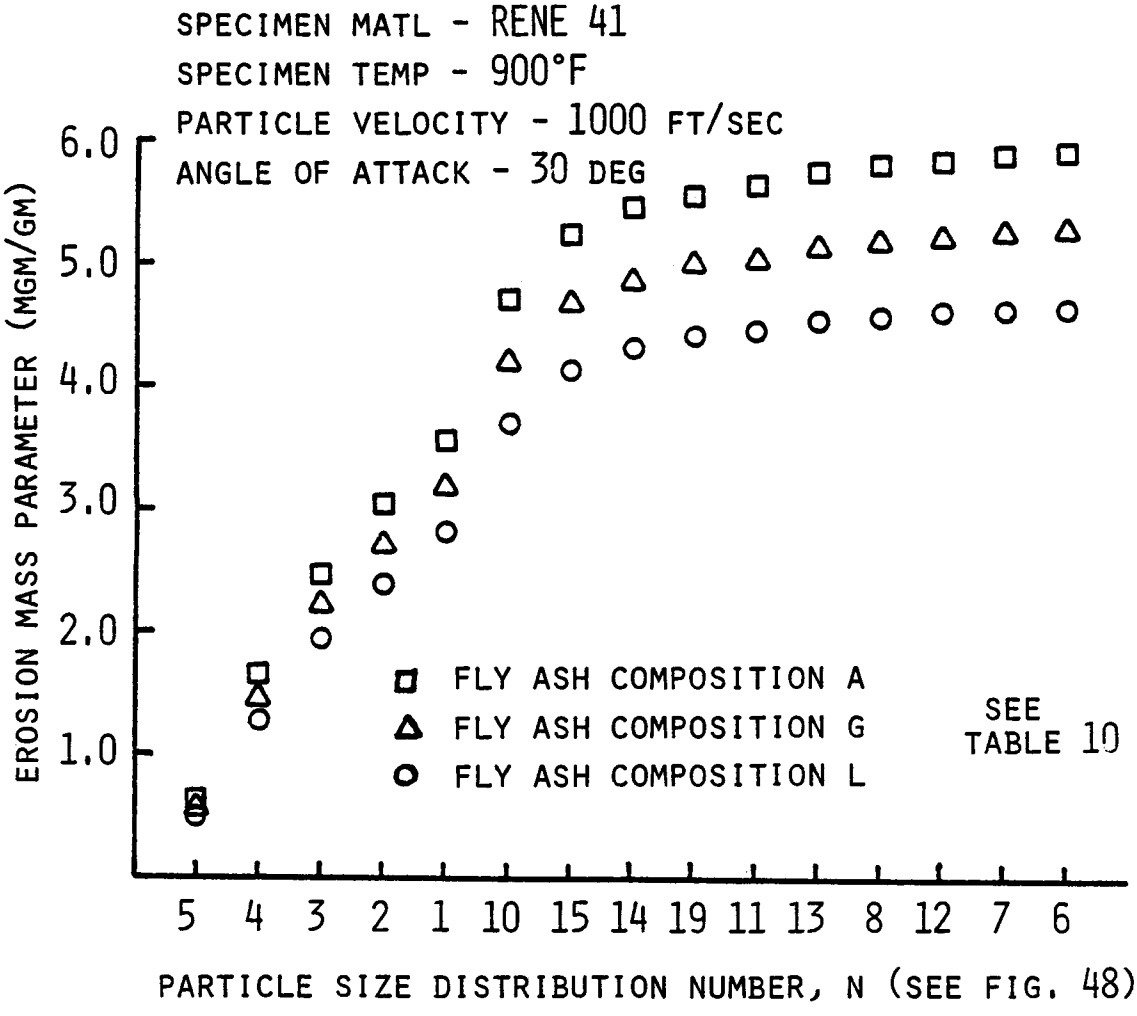

FIG. 52. RELATIVE EROSION LOSS CAUSED BY DIFFERENT TYPES OF FLY ASH PARTICLES ON RENE 41 SPECIMENS. (PREDICTED RESULTS).

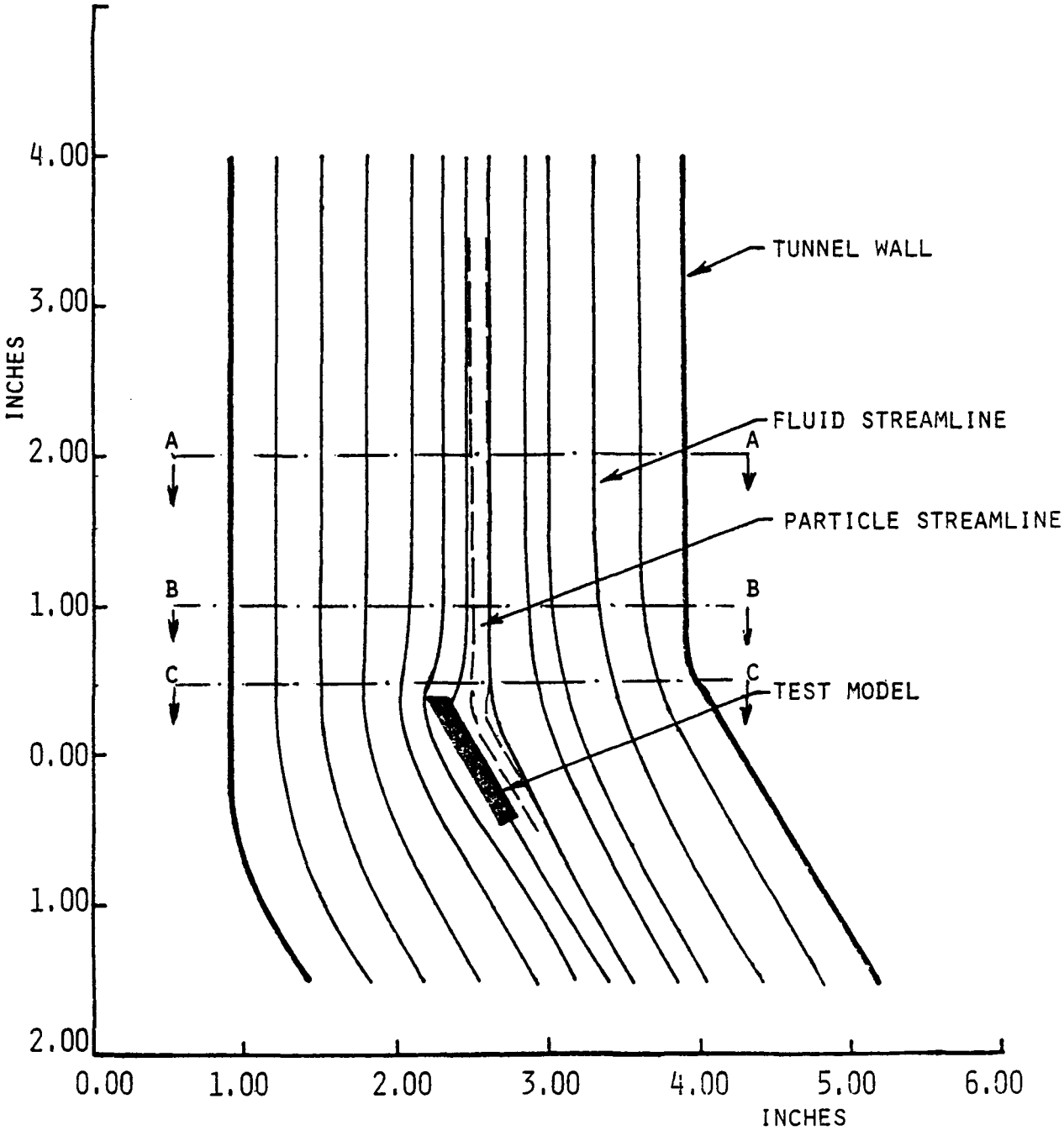

FIG. 53. SCHEMATIC OF WIND TUNNEL TEST SECTION GEOMETRY.

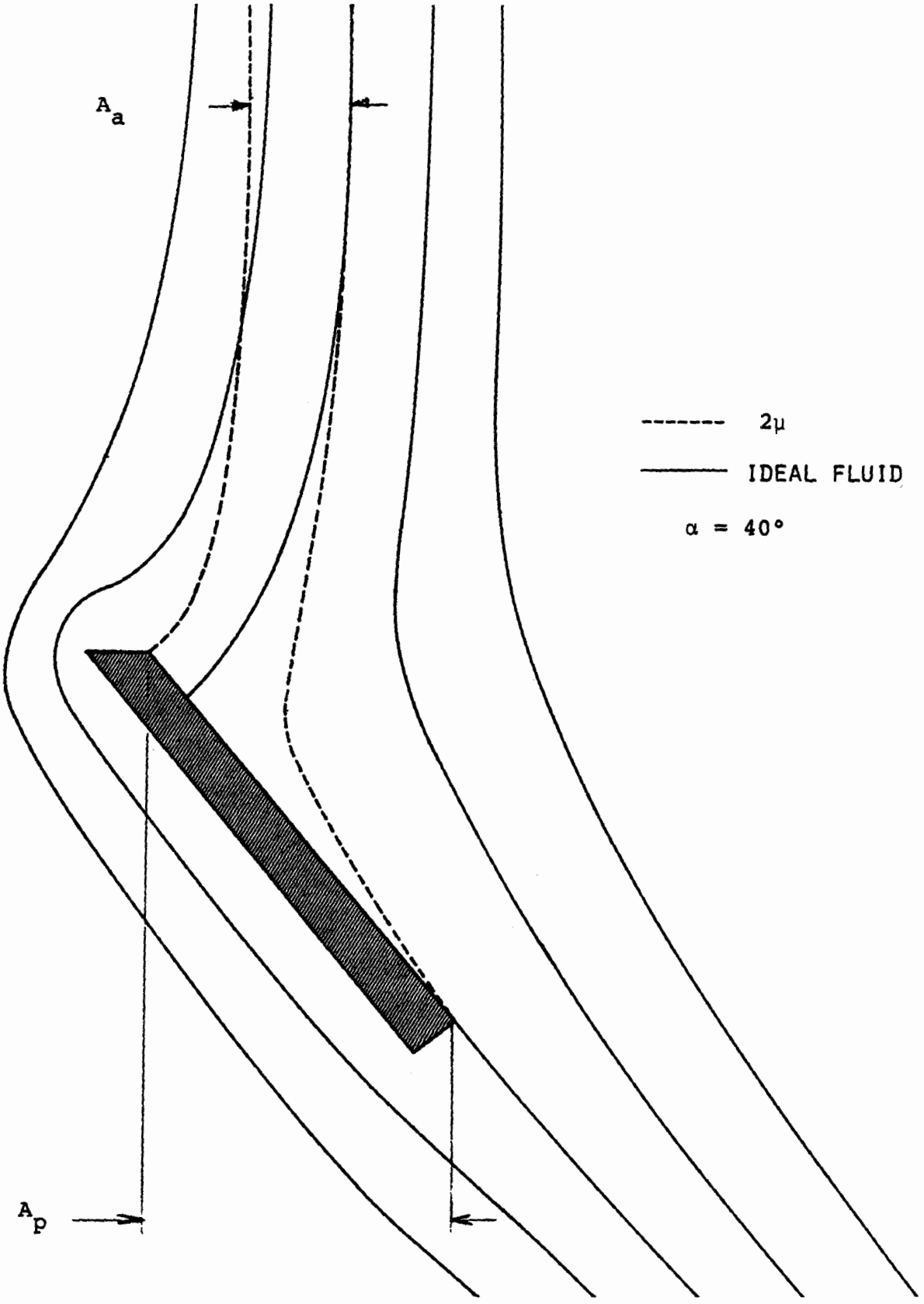

FIG. 54. TRAJECTORIES OF PARTICLES WHICH IMPACT THE SPECIMEN LEADING AND TRAILING EDGES.

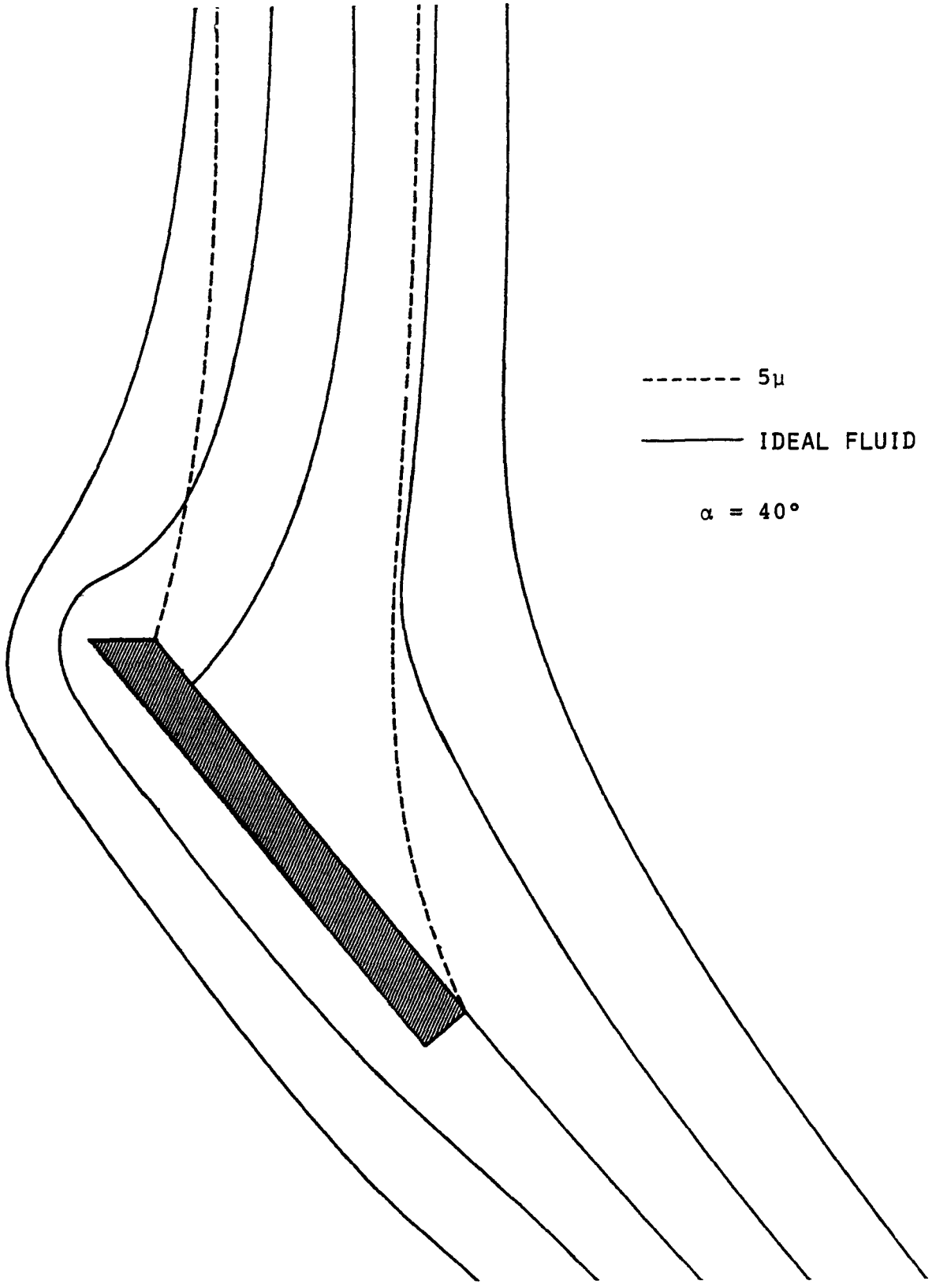

FIG. 55. TRAJECTORIES OF PARTICLES WHICH IMPACT THE SPECIMEN LEADING AND TRAILING EDGES.

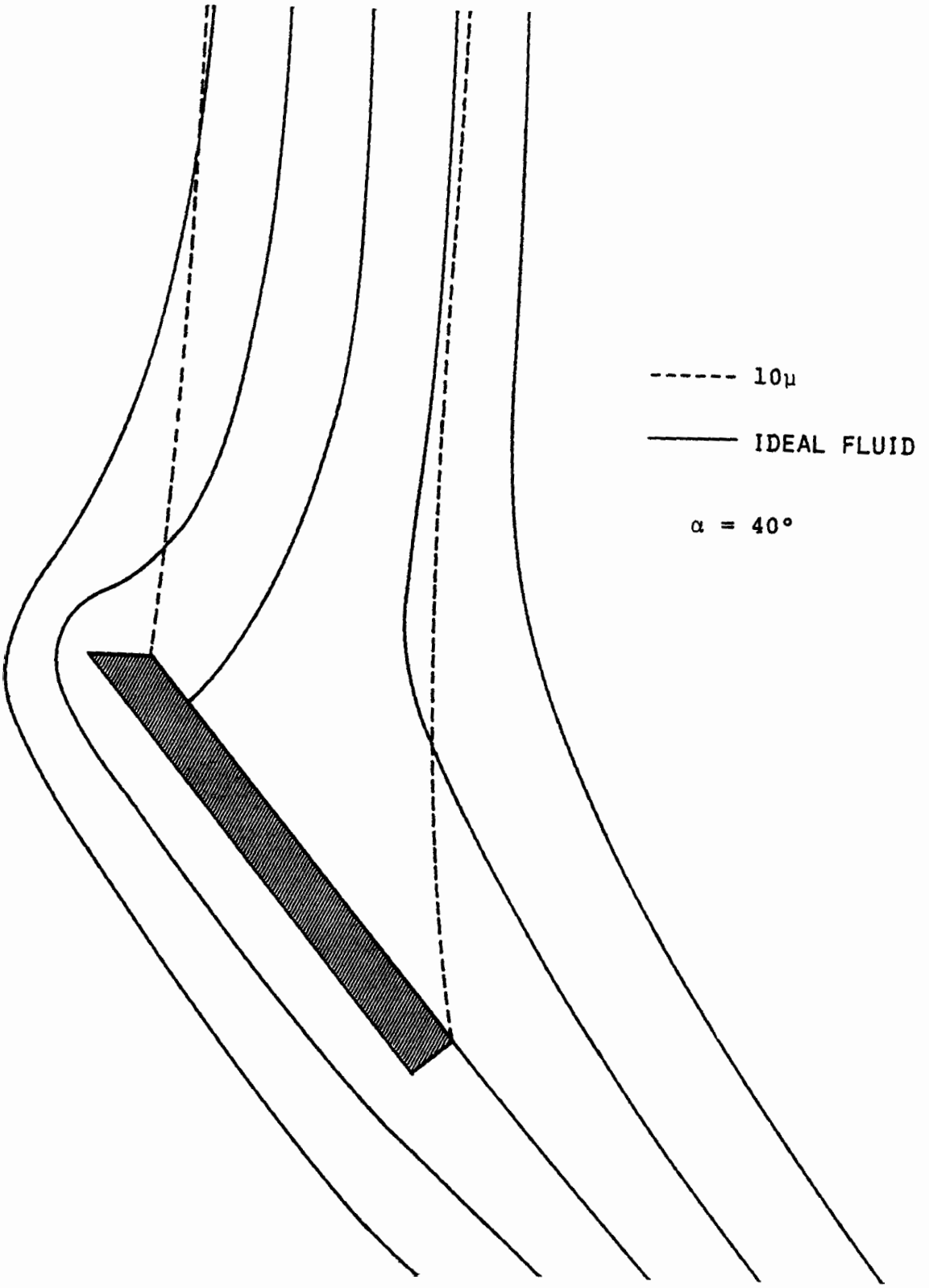

FIG. 56. TRAJECTORIES OF PARTICLES WHICH IMPACT THE SPECIMEN LEADING AND TRAILING EDGES.

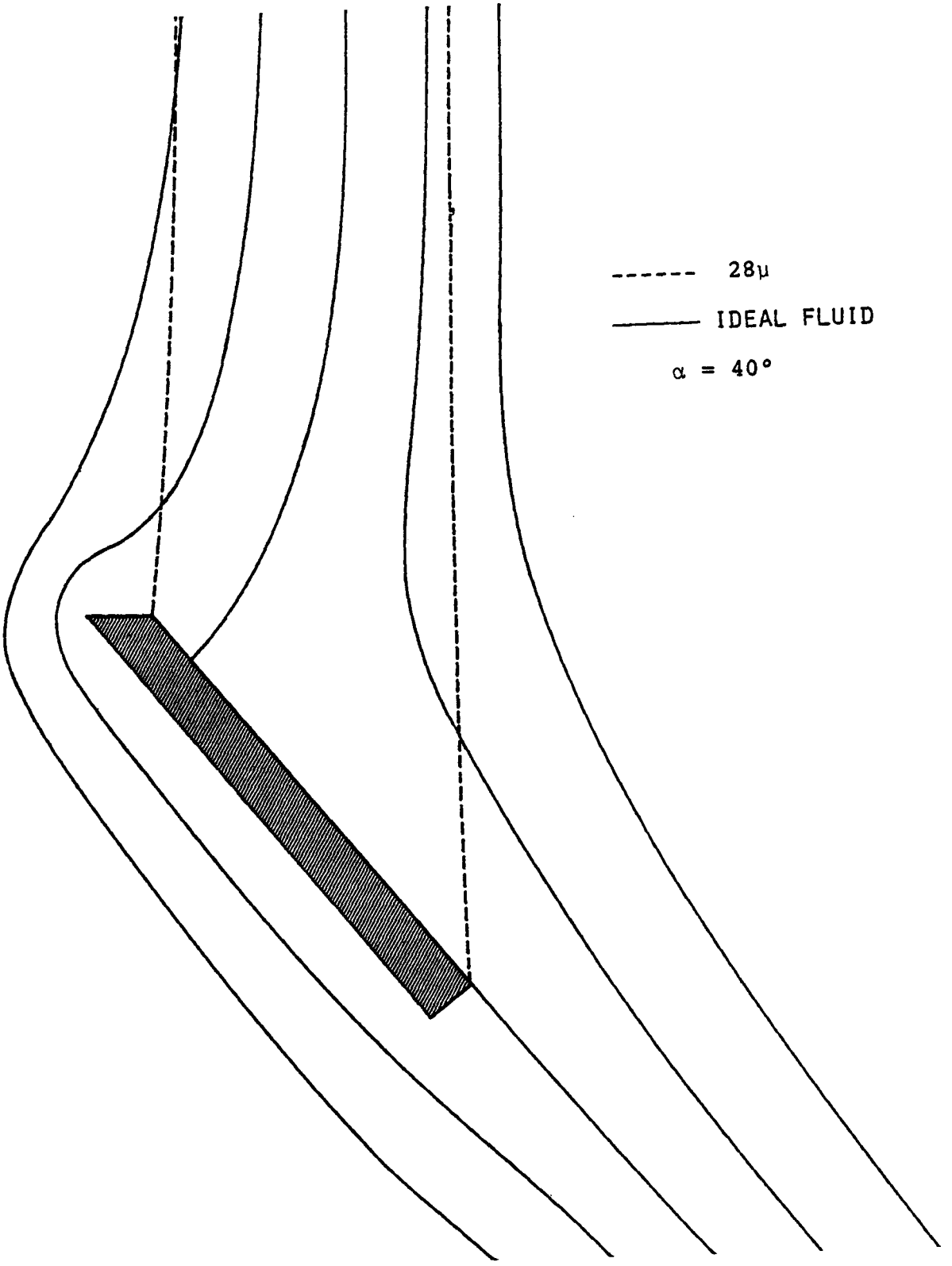

FIG. 57. TRAJECTORIES OF PARTICLES WHICH IMPACT THE SPECIMEN LEADING AND TRAILING EDGES.

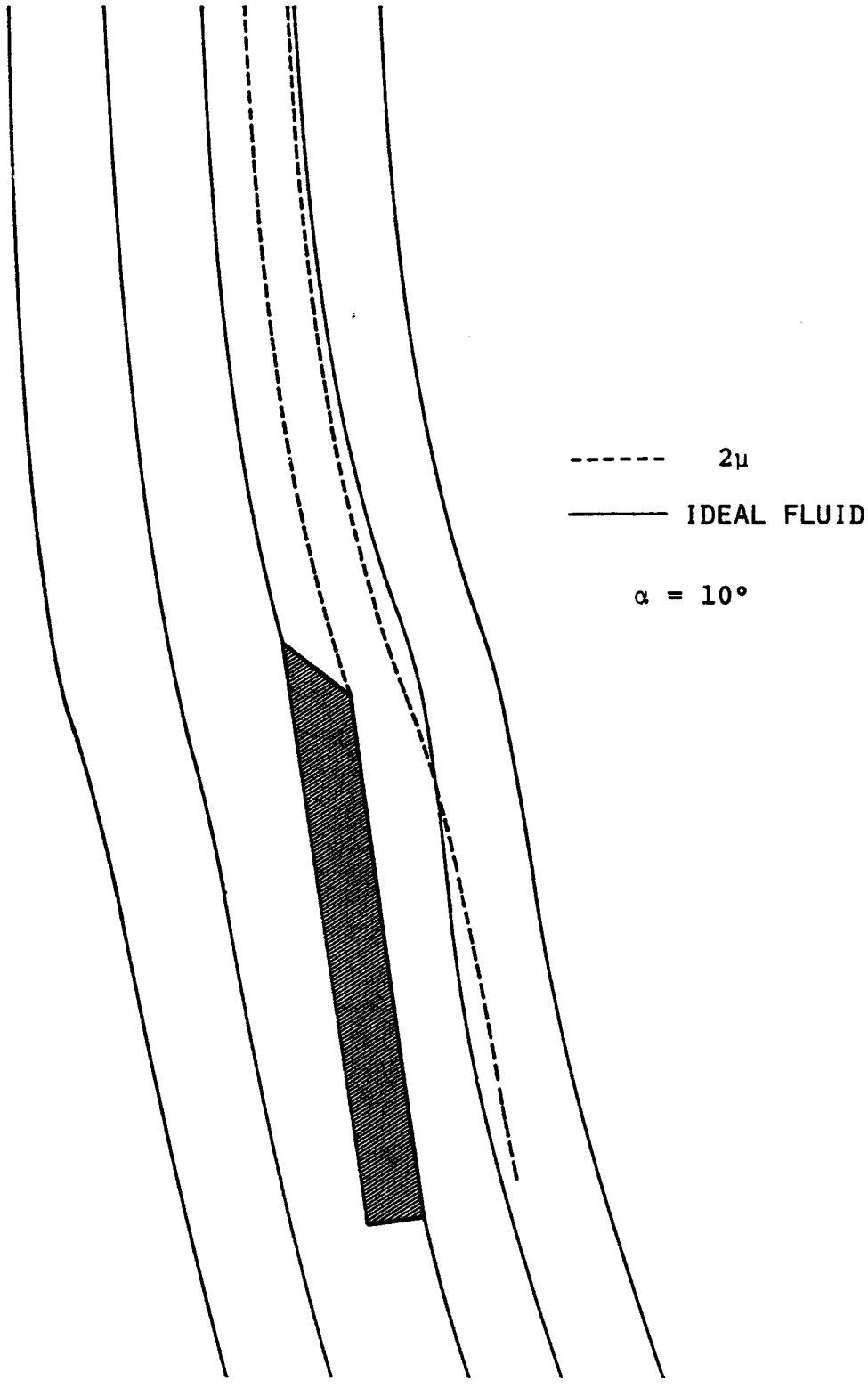

FIG. 58. TRAJECTORIES OF PARTICLES WHICH IMPACT THE SPECIMEN LEADING AND TRAILING EDGES.

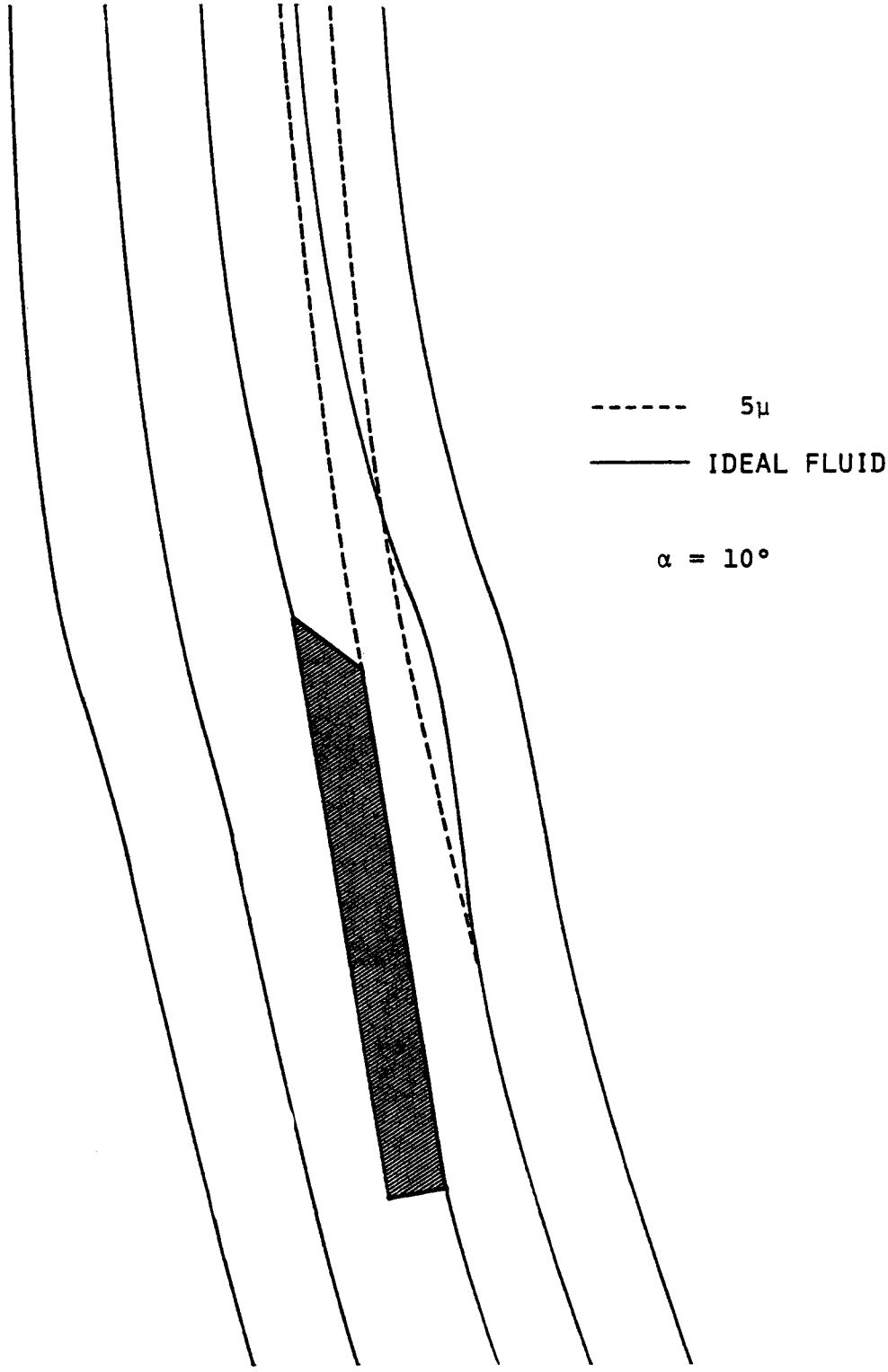

FIG. 59. TRAJECTORIES OF PARTICLES WHICH IMPACT THE SPECIMEN LEADING AND TRAILING EDGES.

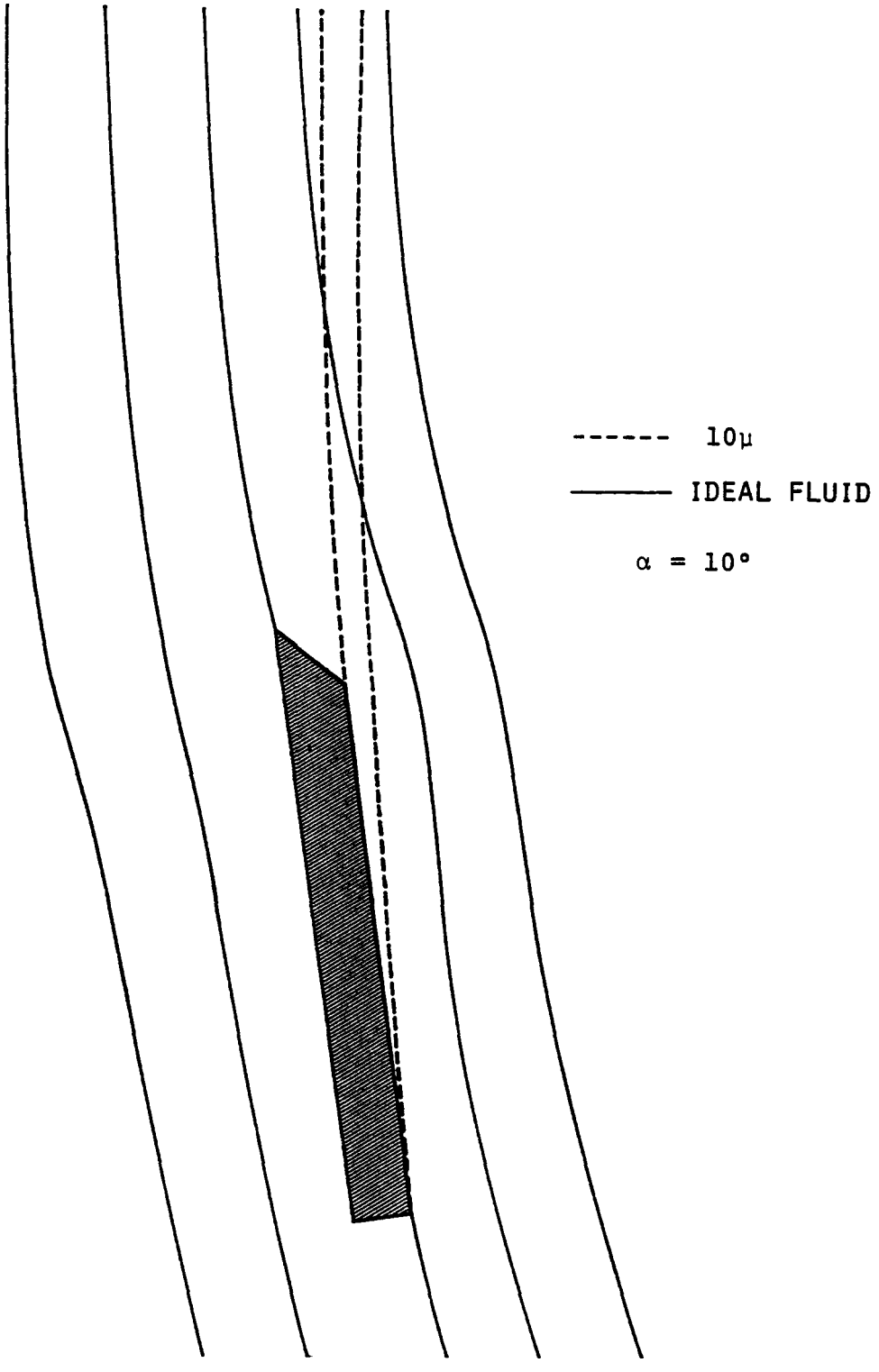

FIG. 60. TRAJECTORIES OF PARTICLES WHICH IMPACT THE SPECIMEN LEADING AND TRAILING EDGES.

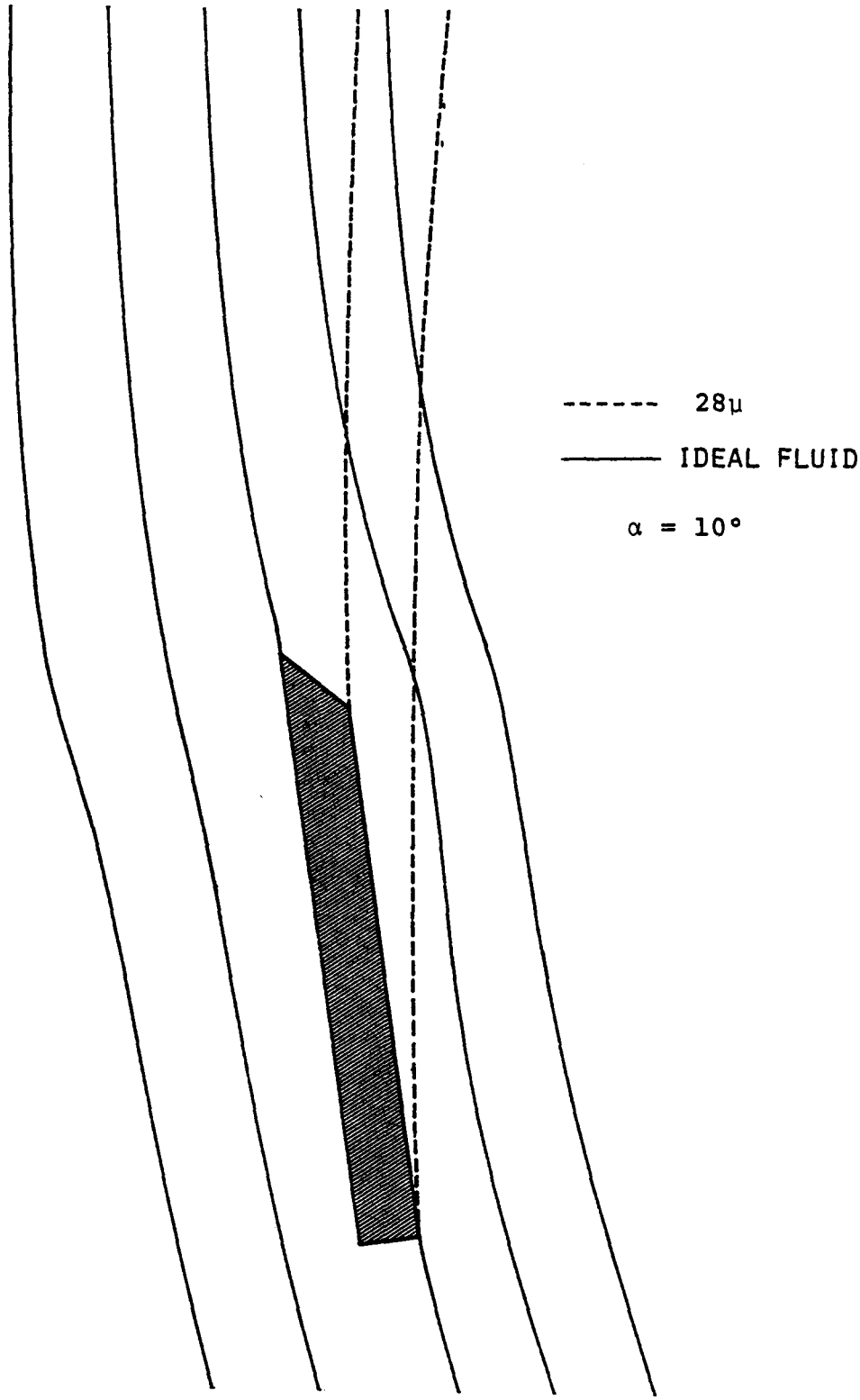

FIG. 61. TRAJECTORIES OF PARTICLES WHICH IMPACT THE SPECIMEN LEADING AND TRAILING EDGES.

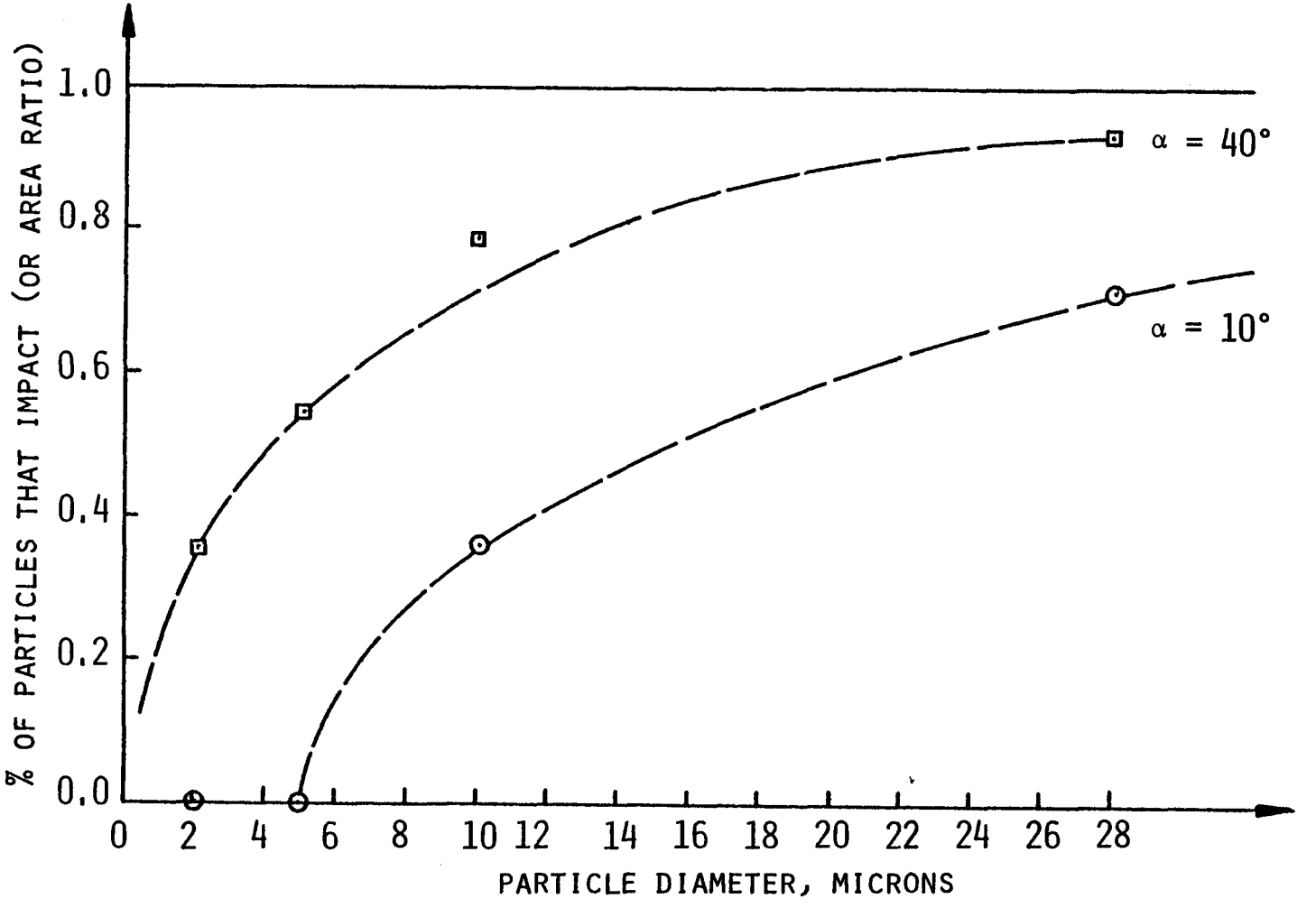

FIG. 62. PERCENT OF PARTICLE THAT IMPACT VS. PARTICLE DIAMETER.

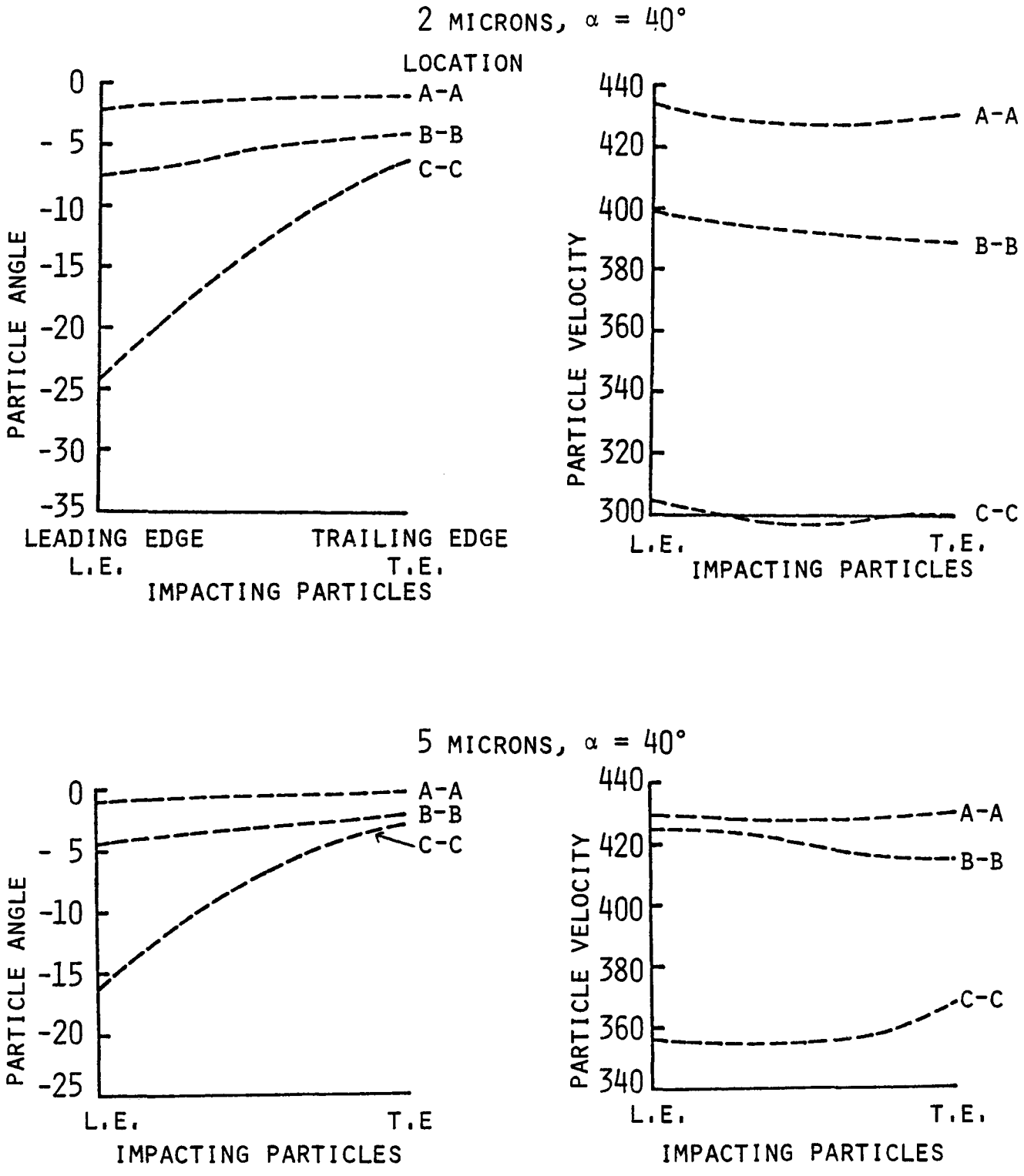

FIG. 63A. PLOTS OF PARTICLE ANGLES AND VELOCITIES AT THREE UPSTREAM LOCATIONS.

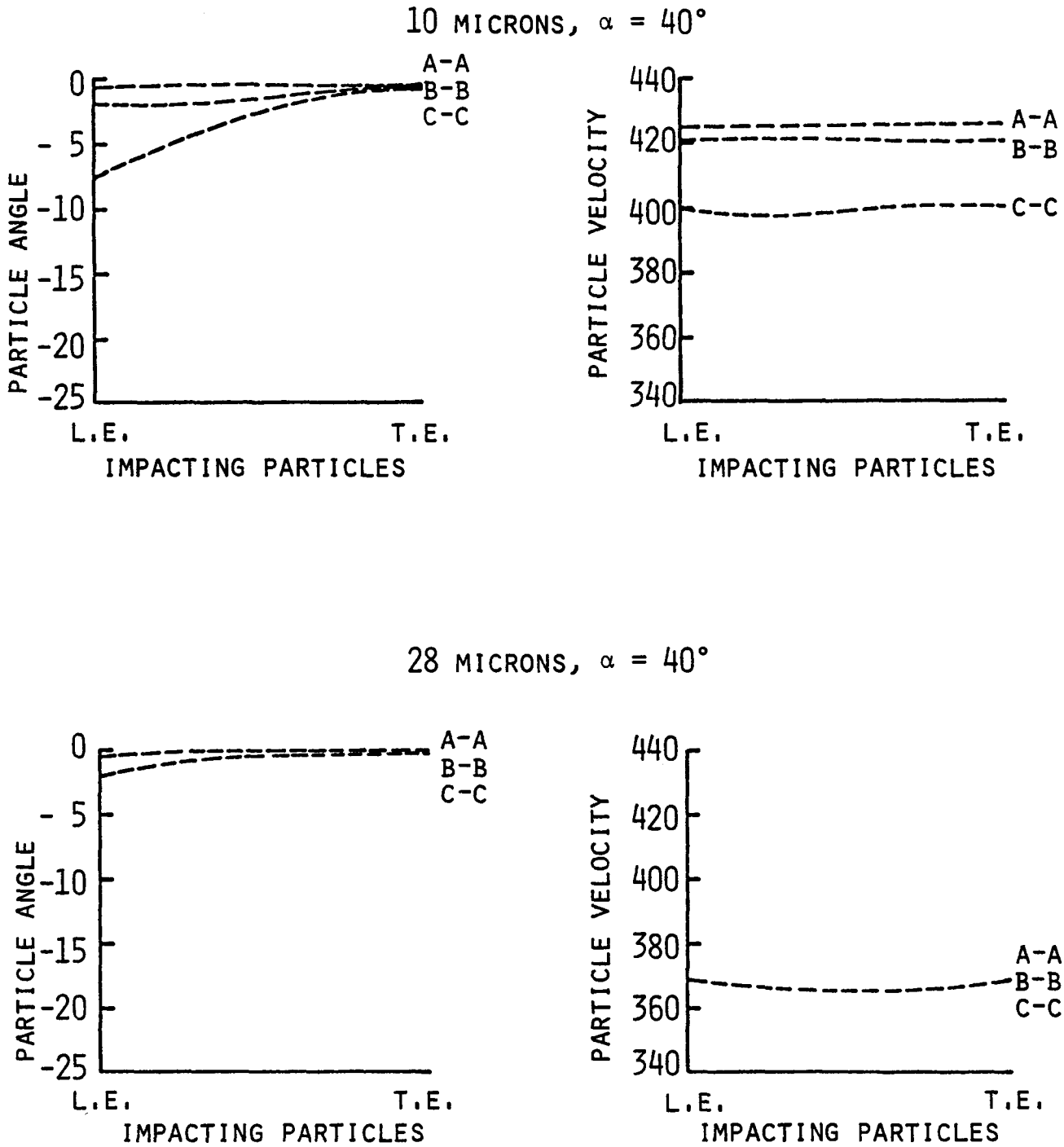

FIG. 63B. PLOTS OF PARTICLE ANGLES AND VELOCITIES AT THREE UPSTREAM LOCATIONS.

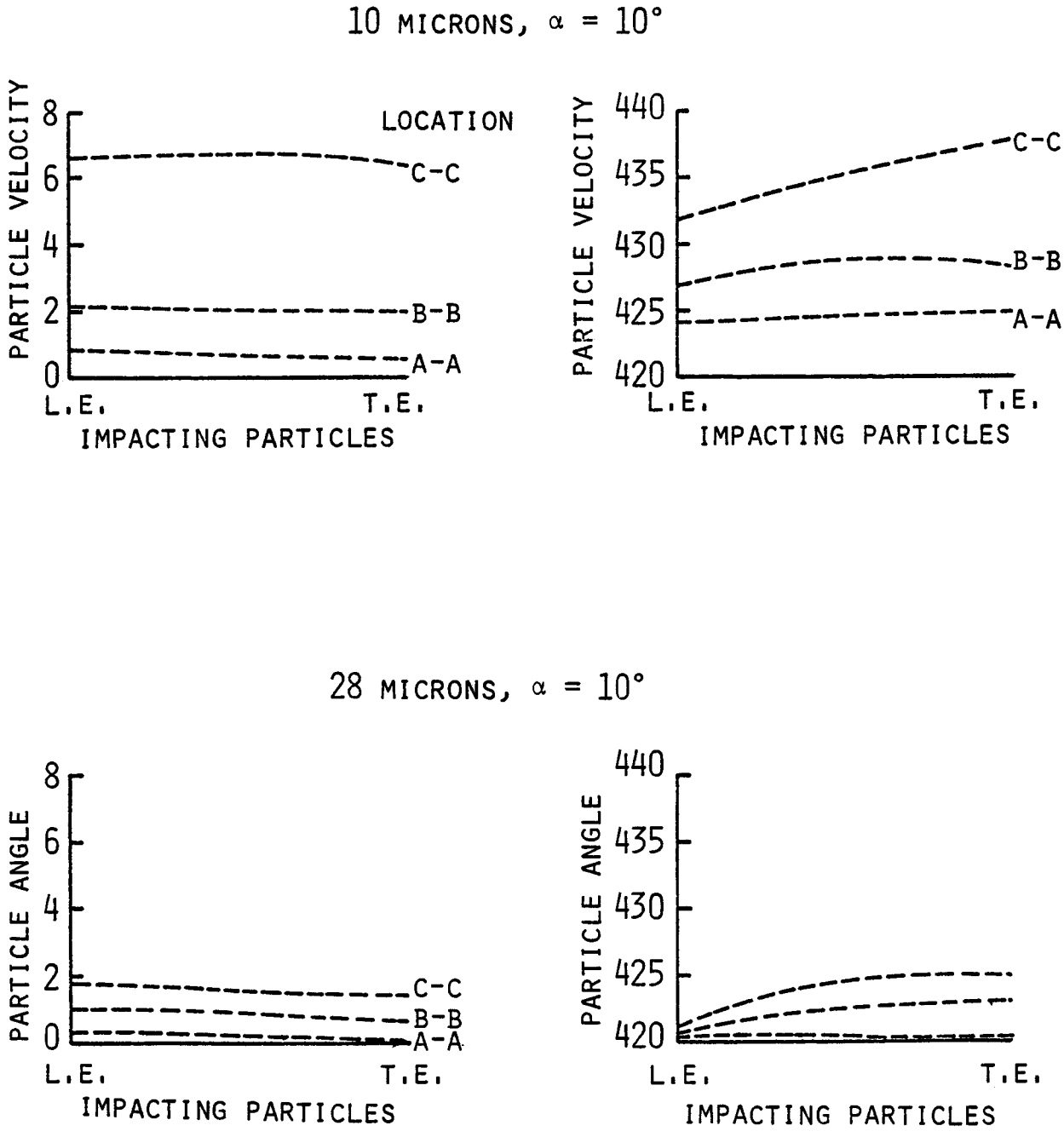

FIG. 64. PLOTS OF PARTICLE ANGLES AND VELOCITIES.

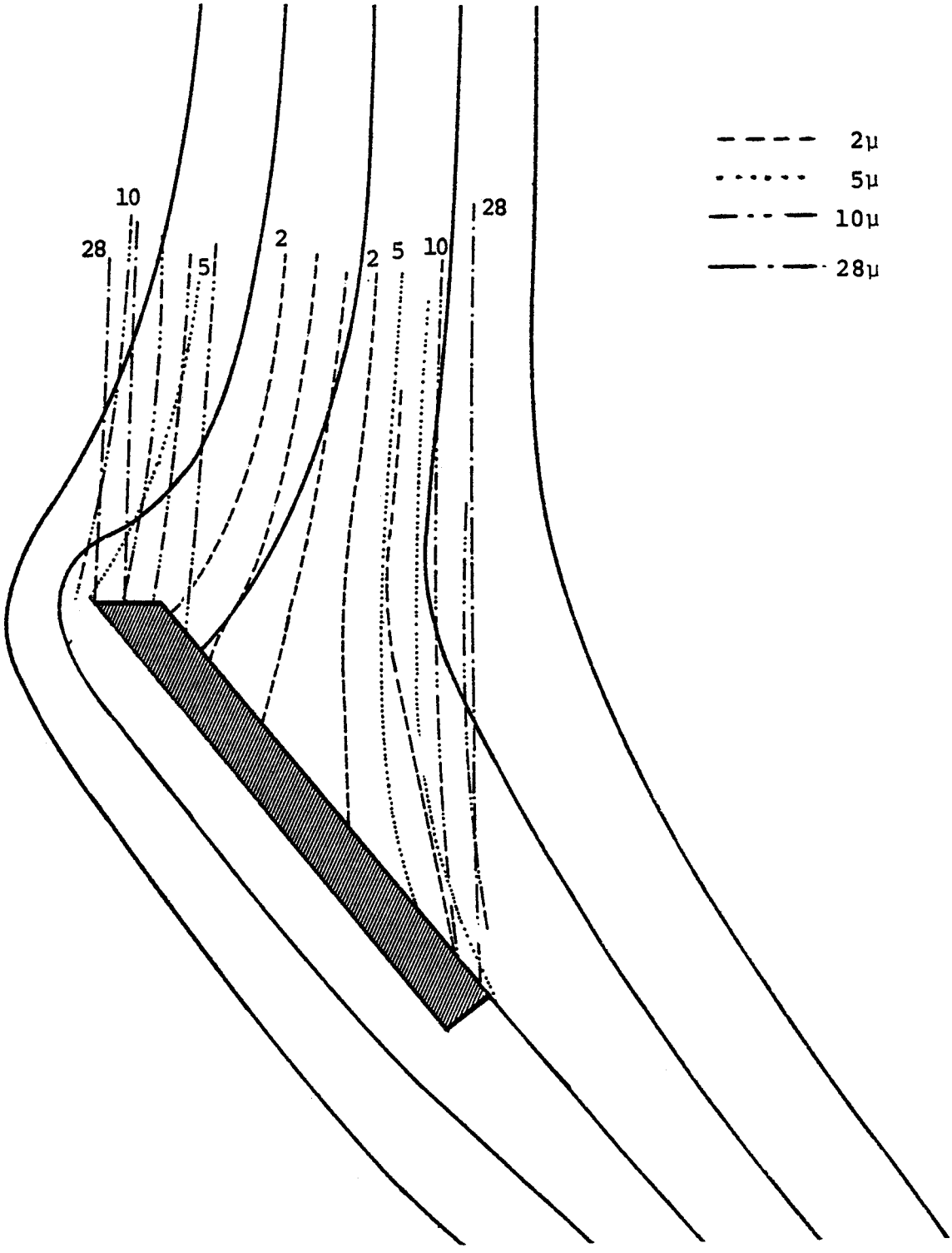

FIG. 65. TRAJECTORIES FOR DIFFERENT PARTICLE SIZES ($\alpha = 40°$).

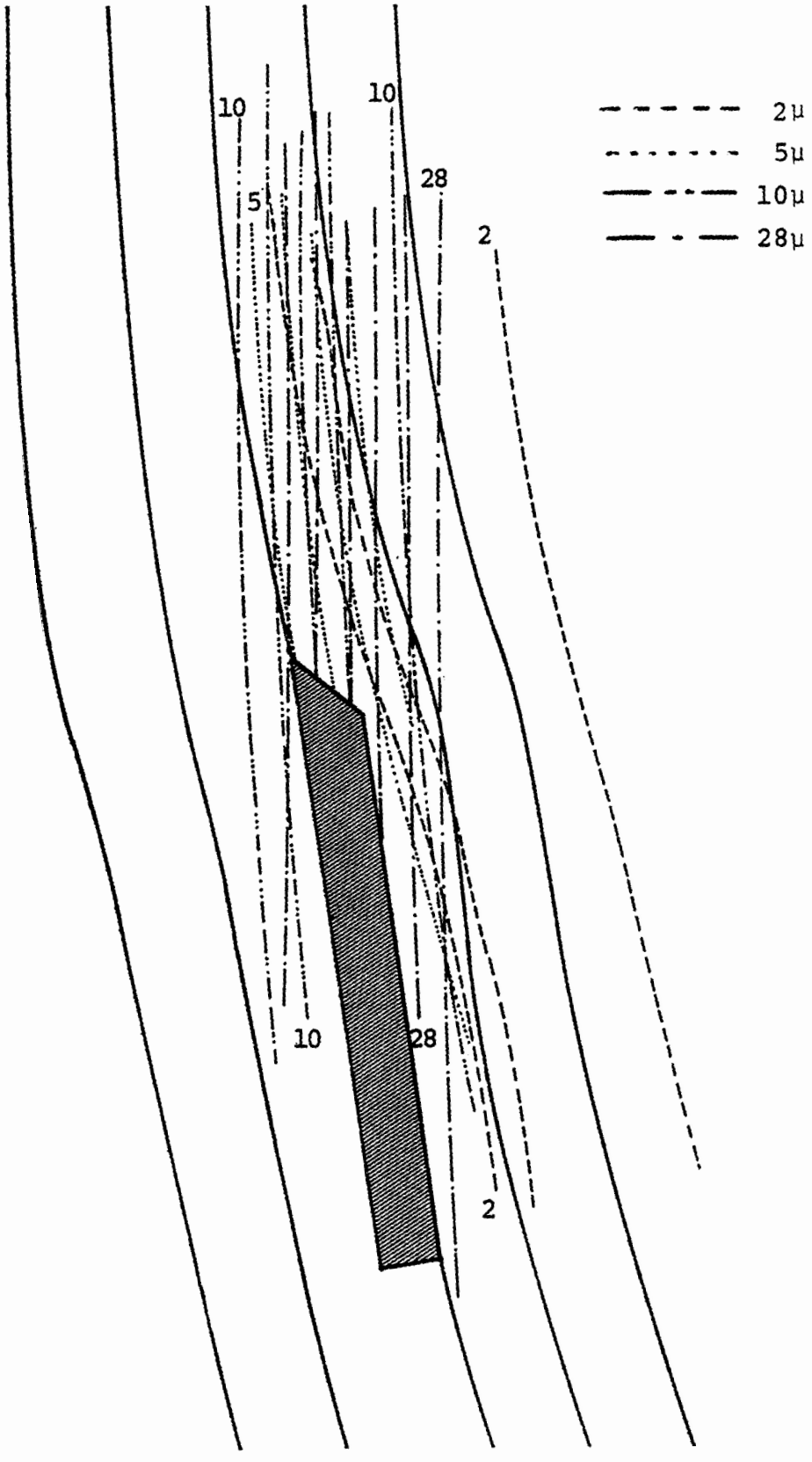

FIG. 66. TRAJECTORIES FOR DIFFERENT PARTICLE SIZES ($\alpha = 10°$).

☆U.S. GOVERNMENT PRINTING OFFICE: 1980-640-258/2394